# Numerical Simulation and Experimental Validation of Low-Pressure Powder Injection Molding Process using Moldflow

by

Foad HAGHNIAZ

THESIS PRESENTED TO ÉCOLE DE TECHNOLOGIE SUPÉRIEURE
IN PARTIAL FULFILLMENT FOR A MASTER'S DEGREE
WITH THESIS IN MECHANICAL ENGINEERING
M.A.Sc.

MONTREAL, APRIL 15, 2022

ÉCOLE DE TECHNOLOGIE SUPÉRIEURE
UNIVERSITÉ DU QUÉBEC

**BOARD OF EXAMINERS THESIS M.Sc.A.**

**THIS THESIS HAS BEEN EVALUATED**

**BY THE FOLLOWING BOARD OF EXAMINERS**

Mr. Vincent Demers, Thesis Supervisor
Department of Mechanical Engineering, École de technologie supérieure

Mr. Jean-François Chatelain, President of the Board of Examiners
Department of Mechanical Engineering, École de technologie supérieure

Mr. Philippe Bocher, Member of the jury
Department of Mechanical Engineering, École de technologie supérieure

THIS THESIS WAS PRENSENTED AND DEFENDED

IN THE PRESENCE OF A BOARD OF EXAMINERS AND PUBLIC

APRIL 11, 2022

AT ÉCOLE DE TECHNOLOGIE SUPÉRIEURE

# ACKNOWLEDGMENT

# Simulation numérique et validation expérimentale du processus de moulage par injection de poudre à basse pression à l'aide de Moldflow

Foad HAGHNIAZ

## RESUMÉ

Le moulage par injection de poudre à basse pression (LPIM) est une technique de fabrication utilisée pour produire des pièces présentant une complexité géométrique élevée et des propriétés mécaniques élevées à des coûts de fabrication inférieurs comparativement aux techniques conventionnelles telles que l'usinage ou le forgeage. Cette technique implique quatre étapes principales comprenant la formulation du mélange, l'injection, le déliantage et le frittage. Bien que toutes ces étapes soient importantes à contrôler, ce projet se concentre sur l'étape d'injection pour mieux comprendre le comportement d'écoulement et les profils de pression des mélanges dans la cavité du moule. À cet égard, il existe peu d'études portant sur le développement de l'étape d'injection à l'aide de mélanges à faible viscosité et, à la connaissance de l'auteur, la validation expérimentale des valeurs de pressions simulées n'a été effectuée qu'une seule fois à l'aide de deux cavités de moule de forme simple.

L'objectif de ce travail est donc d'évaluer la capacité d'un logiciel de simulation numérique commercial à capturer l'influence des paramètres de procédé sur la pression d'injection. La simulation numérique a été réalisée par Autodesk Moldflow Synergy 2019, tandis que la validation expérimentale a été effectuée à l'aide d'injections à échelle réelle dans cinq (5) cavités de moule différentes avec une complexité de forme différente. Quatre mélanges différents formulées à partir de deux poudres différentes (atomisées à l'eau et au gaz) et à partir de deux fraction volumique de poudre (60 et 65 vol. %) ont été caractérisées pour obtenir des propriétés telles que la viscosité, la chaleur spécifique, la densité et la conductivité thermique qui ont finalement été implémentées dans le modèle numérique. Ces mélanges ont ensuite été injectées dans différentes cavités du moule et la pression a été enregistrée expérimentalement à l'entrée du moule.

Les résultats numériques du modèle d'écoulement étaient en bon accord avec les données expérimentales pour différentes étapes de remplissage du moule. Étant donné que les injections ont été effectuées à l'aide d'un débit volumétrique constant, les résultats ont confirmé que les propriétés de la charge d'alimentation, la température de la charge d'alimentation et la température du moule n'ont aucune influence sur le patron d'écoulement. Les résultats de pression simulés étaient en bon accord avec les résultats expérimentaux sur la majorité du remplissage du moule avec une différence relative variant 30 à 64 % en fonction du mélange et des paramètres du procédé, y compris la capacité de prédire l'étape de remplissage associée aux changements de valeurs de pression.

VIII

# Numerical Simulation and Experimental Validation of Low-Pressure Powder Injection Molding Process using Moldflow

Foad HAGHNIAZ

## ABSTRACT

Low-pressure powder injection molding (LPIM) is a manufacturing technique used to produce parts exhibiting a high geometric complexity and high mechanical properties at lower manufacturing costs as compared to the conventional techniques such as machining or forging. This technique involves four main steps including feedstock formulation, the injection, the debinding, and sintering.

Although all these stages are important to be controlled, this project focuses on the injection stage to better understand the flow behavior and pressure profiles of the feedstock within the mold cavity. In this respect, there are only few studies focusing on the development on the injection stage using low-viscosity mixtures and to the best of the author's knowledge, experimental validation of simulated pressures values has been performed only once using two simple shape mold cavities.

The objective of this work is thus to evaluate the capability of the commercial numerical simulation package to capture the influence of process parameters on injection pressure. The numerical simulation was performed by Autodesk Moldflow Synergy 2019, while experimental validation was done using real-scale injections within five (5) different mold cavities with different shape complexity. Four different feedstocks formulated from two different powders (water and gas atomized) and from two solids loading (60 and 65 vol. %) were fully characterized to obtain properties such as viscosity, specific heat, density, and thermal conductivity that were finally implemented in the numerical model. These feedstocks were then injected into different mold cavities and the pressure were experimentally recorded in the gate.

The numerical results of the flow pattern were in good agreement with the experimental data for different mold filling stage. Since the injections were performed using a constant volumetric flow, the results confirmed that the feedstock properties, feedstock temperature, and mold temperature have no influence on the flow pattern behavior. The simulated pressure results were in good agreement with experimental results over the majority of the mold filling stage with maximum relative differences varying from 30 to 64% depending on particular feedstocks and process parameters, including the capability to predict the filling stage associated with the changes in pressure values.

**Keywords:** low-pressure powder injection molding, numerical simulation, metallic powder, feedstock, mold filling

# TABLE OF CONTENTS

# LIST OF TABLES

# LIST OF FIGURES

# LIST OF ABREVIATIONS

| | |
|---|---|
| PIM | Powder injection molding |
| MIM | Metal injection molding |
| LPIM | Low-pressure injection molding |
| HPIM | High-pressure injection molding |
| EVA | Ethylene–vinyl acetate |
| CW | Carnauba wax |
| PW | Paraffin wax |
| SA | Stearic acid |
| DSC | Differential Scanning Calorimetry |
| SEM | Scanning electron microscope |
| vol.% | Volume fraction |
| CFD | Computational Fluid Dynamics |
| FDM | Finite difference method |
| FEM | Finite element method |
| FVM | Finite volume method |
| WA | Water atomized |
| GA | Gas atomized |

# INTRODUCTION

This master's project deals with low-pressure powder injection molding (LPIM) which is an efficient and economical process to produce parts with complex shape and high mechanical properties. This process has a high growth rate in several fields such as automotive, electronics, medical industry and aeronautics.

The LPIM process consists of four steps such as mixing, injection molding, debinding and sintering. First, the metallic powder is mixed with a molten binder to form a homogeneous feedstock. In the second step, the feedstock is injected into a mold cavity. The feedstock is then debound to completely remove the binder, and ultimately the powder component is sintered to final density. This research project focuses specifically on the injection stage in order to better understand the flow behavior of the powder-binder mixture inside different mold cavities. The numerical simulation of the injection stage is a helpful tool to predict the design defects which occur during the LPIM process. This project aims to study the potential of Autodesk Moldflow Synergy to simulate the flow behavior of four differently formulated feedstocks during the LPIM process. In this study, the flow pattern and pressure profiles of four different feedstocks within five mold cavities were investigated and then validated by real-scale injections.

This research project is divided into four chapters. The first chapter concerns the main steps of the powder injection molding process as well as a literature review of the existing studies on the numerical simulation of the injection stage. It is followed by a second chapter in which the problem definition and the research objectives are presented. Then, the third chapter provides an overview of the methodology used to conduct this research including the steps and the equipment used to characterize the feedstock as well as the details about the simulations and process parameters used to obtain the experimental results. The fourth chapter presents a scientific article submitted in Powder Metallurgy (Taylor and Francis) journal which aims to study the numerical simulation of the injection stage during low-pressure powder injection molding (LPIM) and validate the results by experimental tests. Finally, this work ends with a

conclusion that contains a summary of the main results with some recommendations for future research work.

# CHAPTER 1

## Literature review

This chapter introduces the main steps of the powder injection molding process as well as a literature review of relevant studies on the numerical simulation specifically on the injection stage.

## 1.1 Powder injection molding

Powder injection molding (PIM) is a cost-effective manufacturing process used to produce high-volume production of small, complex shape, and dimensionally precise parts (German & Bose, 1997). Arising from the combination of conventional powder metallurgy and plastic injection molding, PIM is commonly divided as metal injection molding (MIM) or ceramic injection molding (CIM) depending on whether metal or ceramic powder is used. The potential of PIM lies in its ability to combine the design flexibility of plastic injection molding and the nearly unlimited choice of material combined with cost reductions offered by powder metallurgy (Hausnerova, 2011). Furthermore, PIM overcomes the dimensional and productivity limits of isostatic pressing and slip casting, the metallurgical and volumetric defects as well as tolerance limitations of investment casting, the low mechanical strength of die-cast parts, and the shape limitation of traditional powder compacts (Gonzalez-Gutierrez et al., 2012). PIM have significant applications in several sectors such as automotive, electrical, aeronautics, aerospace, medical, dental industry, and customer products. Due to the demand for high-performance materials and the miniaturization of complex components in various fields, PIM market passed from $ 1 billion in 2007 to $2 billion dollars in 2018, exhibiting an overall growth of about six times larger as compared to the market in early 90s(German, 2008) and (MIM2018: International Conference on Injection Molding of Metals, Ceramics and Carbides). Metal injection molding is still considered the largest segment of this market, accounting for more than 75% of global output of PIM. Although the sales growth varies year to year, in most recent times the global sales gain has sustained at 14% per year (German, 2012) .

The MIM process includes basically four steps known as mixing, injection molding, debinding, and sintering as schematized in Figure 1.1. The first step consists in preparing a mixture formulated from fine solid micrometric powders with a molten polymeric binder called the feedstock. During this step, all constituents are blended into a mixer and then heated at a temperature slightly above the binder melting point to provide a uniform coating on the powder surface (Figure 1.1a). The powder content usually ranges from 50 to 65 vol. %, where a powder content lower than 50 vol. % will make the sintering impossible (i.e., not enough powder contact), and a powder content higher than 65 vol. % will make the injection impossible (i.e., too high feedstock viscosity) (Merz et al., 2002). A homogeneous distribution of powder particles and binder in feedstock is required to minimize the segregation phenomenon (i.e., separation of powder and binder) during the injection molding stage within components and to prevent visual defects, excessive porosity, warpage, heterogeneous shrinkage, and cracks during the sintered stage (Quinard et al., 2009; Thornagel, 2010). Following the mixing step, the molten feedstock is then injected into the mold cavity and cool down to solidify the injected part before to be finally ejected from the mold (Figure 1.1b). During the debinding stage, the polymeric binder is removed to get a shaped of the metallic component in a porous state (Figure 1.1c). The three main methods known as thermal, solvent, and catalytic debinding can be used depending on the binder system (Gonzalez-Gutierrez et al., 2012; Krueger, 1996; Mathew & Mastromatteo, 2003). The final stage consists of sintering stage to provide the interparticle bonding and finally development of a granularmicrostructure that imparts strength and integrity of the part during its service (Figure 1.1d). In few words, the debound parts are sintered at temperatures ranging from 1200 to 1600°C, depending on the material. The solid-state diffusion mechanism leads in decrease in the volume fraction of pores, accompanied by growth and strong adhesion among the adjacent particles, leading to a macroscopic shrinkage of about 14 and 20% (Gonçalves, 2001; Krug et al., 2002).
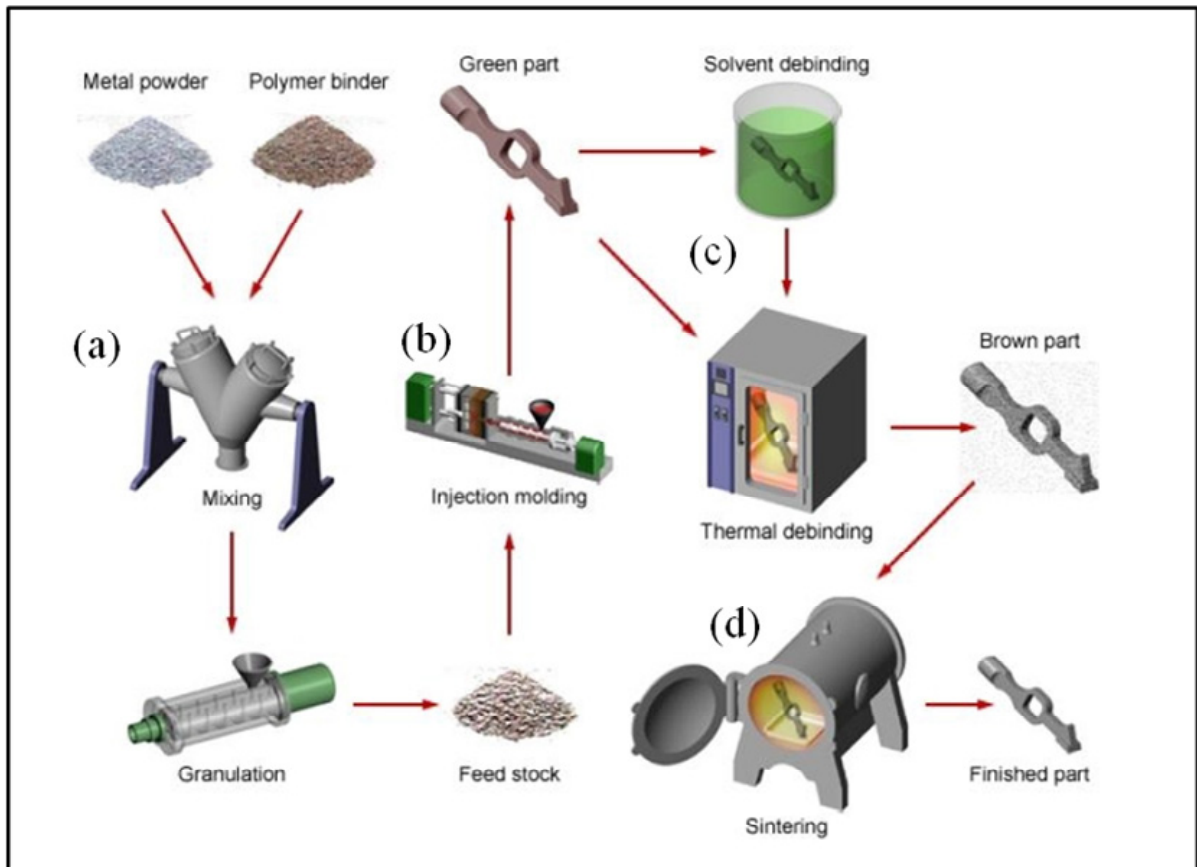
Figure 1.1 Process of metal injection molding (MIM)
Taken from Custompartnet (2022)

## 1.2    Comparison between HPIM and LPIM process

There are two types of PIM process called high-pressure powder injection molding (HPIM) and low-pressure powder injection molding (LPIM). Although these techniques are virtually similar, the difference in the binder systems directly leads to change in the mixing, molding, and debinding approaches, while the sintering process remains the same. HPIM has been widely used in industry for several decades, while LPIM process is relatively recent. As presented in Table 1.1, the main distinction between these two processes is the pressure required during the injection operation. High-molecular weight binders used in HPIM (e.g., polyethylene, polypropylene, etc.) result in high-viscosity of the feedstock varying between 100 to 1000 Pa·s which requires an injection pressure up to 200 MPa and mold clamping forces of about 100 Tons (German & Bose, 1997). This high feedstock viscosity limits the flowability

of the mixture and therefore, the complexity of the injected parts. HPIM technology is suitable for high production volume since the cost of the injection machine and tooling is very high in order to withstand high pressures during this process. In counterpart, powder segregation is prevented due to this high-viscosity constituents used in HPIM feedstock. As a result, the homogeneity of the feedstock is maintained during all stages of the process.

Low-molecular weight binders used in LPIM (e.g., paraffin wax, beeswax, carnauba wax, etc.) generate a low-viscosity feedstock typically between 1 and 20 Pa·s, rarely exceeds 50 Pa·s (Kamal & Isayev, 2012) that require an injection pressure generally below 1 MPa and a low mold clamping forces <1 Ton. This low feedstock viscosity directly leads in an increase the molding capabilities, an increase in shape complexity (Fareh et al., 2016; Lamarre et al., 2017). However, powder segregation phenomenon can be observed because of the absence of a backbone polymer in LPIM feedstock. However, this phenomenon can be minimized using thickening agents and different injection strategies that help to maintain the homogeneity of the feedstock. Consequently, LPIM has noteworthy processing advantages over the conventional HPIM technology including reduction in the size of injection equipment as well as reduction in tooling size due to the low pressure required in this process which directly lead to a cost-effective technology for manufacturing small and complex shape components, either in high- or in low-production volumes (Medvedovski & Peltsman, 2012).

Table 1.1 Comparison between LPIM & HPIM process
Adapted from Azzouni (2020, p. 7)

|                                     | HPIM      | LPIM         |
|-------------------------------------|-----------|--------------|
| Maximum injection pressure (MPa)    | 200       | 50           |
| Cost of tooling                     | High      | Low          |
| Volume of production                | High only | Low and high |
| Viscosity of mixture (Pa·s)         | < 1000    | < 10         |
| Segregation                         | No        | Yes          |

Although all PIM stages are important, the injection step remains one of the main steps that must be controlled to produce a good quality metallic or ceramic part. In this respect, numerical simulation of the injection stage becomes an interesting tool to predict the mold filling behavior

of the feedstock (capability to fill the mold) and the maximum pressure required during the operation (capability of the equipment to realize the injection stage).

## 1.3 Numerical simulation of powder injection molding

Numerical simulations are typically used to better understand, predict, and optimize the injection stage parameters before starting the industrialization and finally production of new feedstocks or new parts (Barriere et al., 2002; Kennedy & Zheng, 2013). This tool is suitable to predict filling time, shear rates, pressures, and melt front velocities or other physical quantities that are sometimes difficult or simply impossible to obtain experimentally. Obtaining these physical quantities allows a better understanding of the flow pattern through the mold cavity. To simulate and study mold filling using numerical simulations, several different software packages can be used. Whatever the package, several feedstock characteristics such as viscosity profile, density, specific heat capacity, and thermal conductivity need to be experimentally measured and the implemented into the models to obtain accurate simulations. The next subsections describe the existing packages and feedstock characterization approaches required for numerical simulations.

### 1.3.1 Input parameters for numerical simulation of the injection stage

#### 1.3.1.1 Feedstock viscosity

Viscosity ($\eta$) is a measure of a fluid's resistance to flow expressed in Pa·s. Fluids exhibiting constant viscosity regardless of the shear rate are categorized as Newtonian fluids while others whose viscosity varies according to the shear rate are referred as non-Newtonian fluids. Powder-binder mixtures used in the PIM process are non-Newtonian exhibiting shear thinning behavior meaning that the viscosity decreases as the shear rate increases as schematized in Figure 1.2. To implement the viscosity profile into the simulation packages (i.e., viscosity vs. shear deformation rate), experimental data are fitted to different viscosity models to describe the rheological behavior of the feedstock. The Power-law model presented in equation

$(\eta = k\dot{\gamma}^{(n-1)}$ (1.1) and also known as the Ostwald–deWaele equation is a type of generalized Newtonian fluid, where the power index "$n$" is obtained by fitting experimental data to the model and determines whether flow exhibits a Newtonian ($n = 1$), shear thinning ($n < 1$), or shear thickening ($n > 1$) behavior.

$$\eta = k\dot{\gamma}^{(n-1)} \tag{1.1}$$

where $\eta$ is the feedstock viscosity, $\dot{\gamma}$ is the shear deformation rate, $k$ is a flow consistency index (constant), and $n$ is a flow behavior index. However, this model's flaw is its inability to capture the Newtonian plateau that sometimes exists before or after a shear thinning zone seen in Figure 1.2 (Koszkul & Nabiałek, 2004; Tim Osswald & Natalie Rudolph, 2014; Poh, 2019).
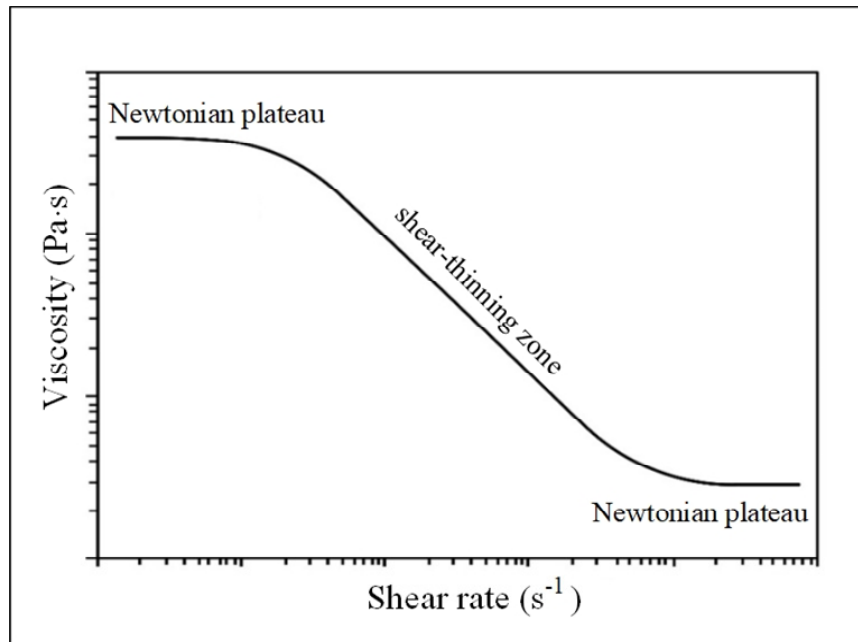


Figure 1.2 Typical viscosity profile of a PIM feedstock

Adapted from Barnes et al. (1989, p. 17)

To cover both Newtonian and non-Newtonian zones of viscosity profile typically observed with PIM feedstocks, other viscosity models are reported in the literature. For instance, Carreau model expressed in equation $(\eta(\dot{\gamma}) = \eta_\infty + \dfrac{\eta_0 - \eta_\infty}{[1+(\lambda\dot{\gamma})^2]^{\frac{(1-n)}{2}}}$ (1.2)

describes the rheological of the powder-binder mixture better than Power-law model while considering the Newtonian plateaus (Khan et al., 2018; Macosko, 1994).

$$\eta(\dot{\gamma}) = \eta_\infty + \frac{\eta_0 - \eta_\infty}{[1+(\lambda\dot{\gamma})^2]^{\frac{(1-n)}{2}}} \tag{1.2}$$

where $\eta_0$ is viscosity at a zero shear rate (Pa·s), $\eta_\infty$ viscosity at infinite shear rate (Pa·s), $n$ is a flow behavior index, and $\lambda$ is relaxation time (s). All variables in this model are determined by fitting it to experimental data. The viscosity of a PIM feedstock was fitted using Carreau model by Gonzalez-Gutierrez et al. (Gonzalez-Gutierrez et al., 2016) in Figure 1.3 for stainless steel-based feedstocks at different solid loadings (solid lines). The Newtonian plateau begins to rise as the powder loading increases, and this region was impossible to be fitted for the feedstocks with solid loading higher than 30% vol. The lack of Newtonian plateau was attributed to the possible presence of yield stress.
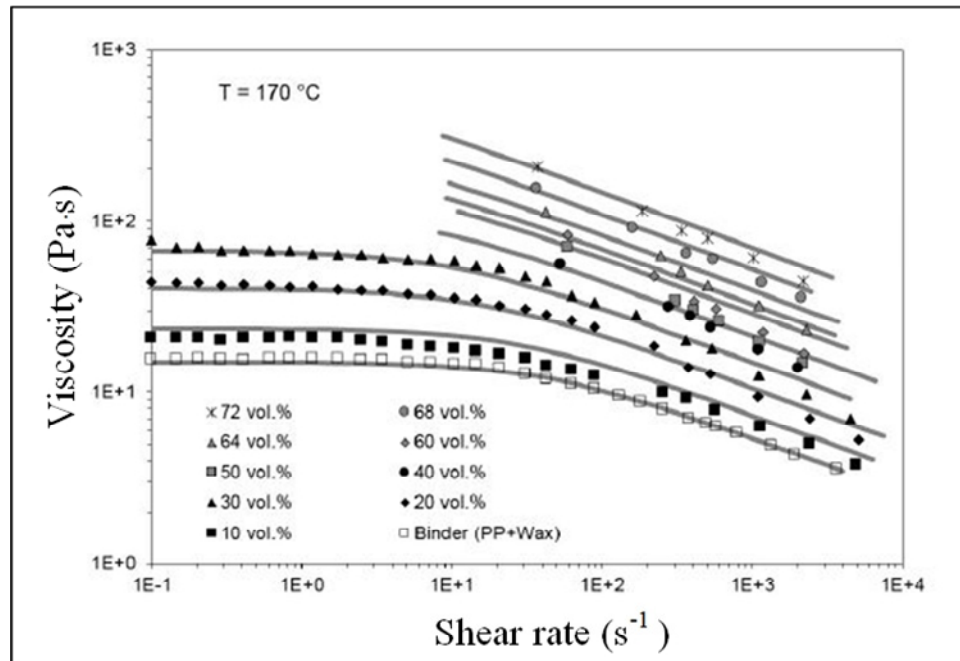


Figure 1.3 Viscosity of the feedstocks with different solid loadings fitted
by Carreau model
Taken from Gonzalez-Gutierrez et al. (2016, p. 11)

Due to additional parameters proposed by Yasuda, the modified Carreau-Yasuda model obtained additional flexibility and became applicable for describing viscosity versus shear rate curves, which have several regions of different characters (Bilovol, 2003). Carreau-Yasuda model can be written as the following equation $(\eta(\dot{\gamma}) = \eta_\infty + \frac{\eta_0 - \eta_\infty}{[1+(\lambda\dot{\gamma})^a]^{\frac{(1-n)}{a}}}$

(1.3):

$$\eta(\dot{\gamma}) = \eta_\infty + \frac{\eta_0 - \eta_\infty}{[1+(\lambda\dot{\gamma})^a]^{\frac{(1-n)}{a}}} \tag{1.3}$$

where a is Yasuda parameter and other variables are described above. Cross model given in equation $(\eta(\dot{\gamma}) = \eta(\infty) + \frac{\eta_0 - \eta_\infty}{1+(\lambda\dot{\gamma})^{-1}}$ (1.4) is commonly used to describe the viscosity at low-shear rate.

$$\eta(\dot{\gamma}) = \eta(\infty) + \frac{\eta_0 - \eta_\infty}{1+(\lambda\dot{\gamma})^{-1}} \tag{1.4}$$

where all variables are described above. This model is found in different forms with or without modification for yield stress (Atre et al., 2007; Bilovol et al., 2003; Hwang & Kwon, 2002; Ilinca & Hétu, 2001; Ilinca et al., 2004; Samanta et al., 2008; Thomas et al., 2009). However, Power-law, Carreau-Yasuda, and Cross models do not take into account temperature effects. An Arrhenius type power-law model is used to describe the dependence of viscosity on temperature as shown in equation $(\eta(\gamma,\dot{T}) = B \exp\left[\frac{E}{RT}\right] \dot{\gamma}^{n-1}$ (1.5):

$$\eta(\gamma,\dot{T}) = B \exp\left[\frac{E}{RT}\right] \dot{\gamma}^{n-1} \tag{1.5}$$

where $n$, $B$, $E$, and $R$ represent the power-law exponent, the material specific reference factor (or reference viscosity), the flow activation energy for the Arrhenius temperature dependence

of the viscosity, and the gas constant, respectively. The parameters in the above equation can be derived by curve fitting of the experimental results. Using Arrhenius model, Lin et al. (Lin et al., 2017) studied the rheological properties of blended elemental Ti-6Al-4V (BE Ti64) and pure titanium (Ti) feedstocks for the injection stage. To evaluate the dependence of viscosity on temperature, feedstocks rheological properties were measured at three different temperatures and the value of $n$ was derived by fitting the viscosity profiles Figure 1.4a-b. In this study, the lower value of $n$ for the BE Ti64 feedstock indicated that the latter exhibits a lower shear thinning effect than Ti feedstock. The parameter $E$ was derived by fitting the viscosity and temperature data Figure 1.4c-d. The estimated activation energy for flow of the BE Ti64 feedstock was similar to that of the Ti feedstock indicating they have a similar sensitivity degree to a temperature change during molding process.
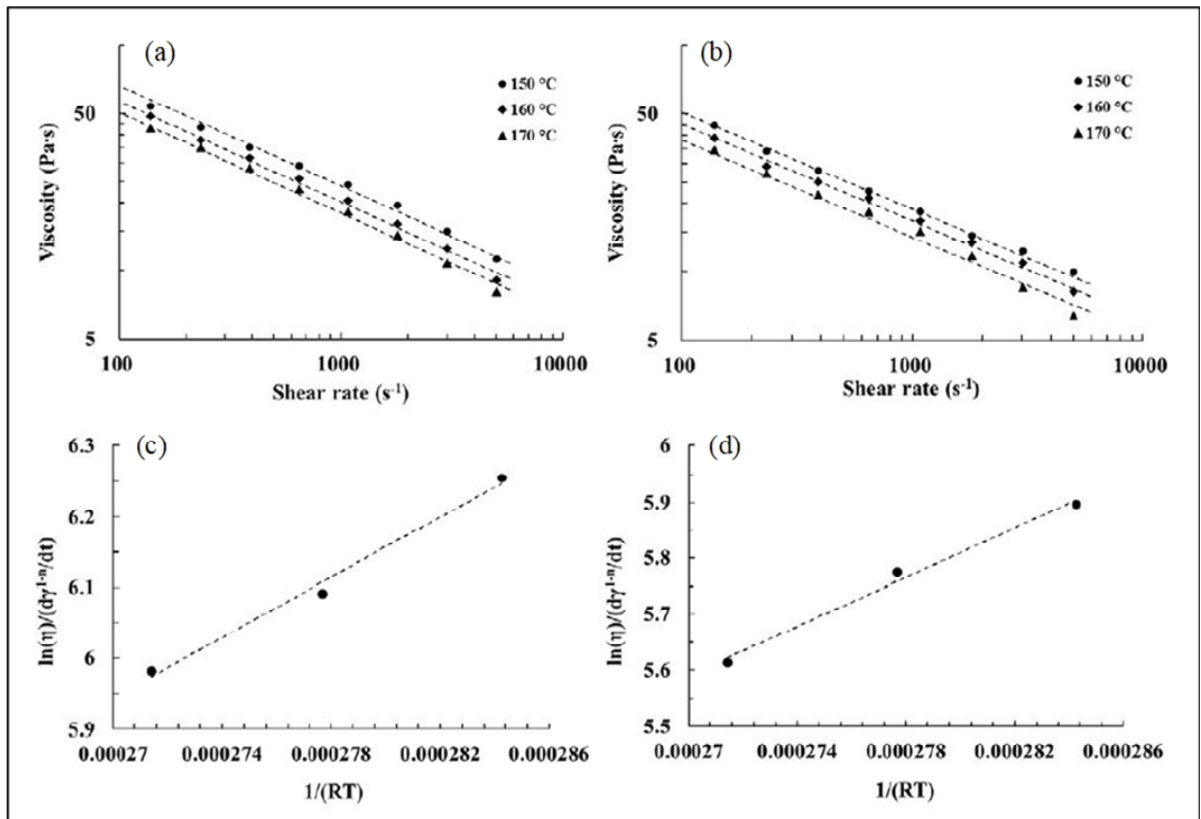


Figure 1.4 (a-b) Viscosity profiles and fitting results (the slope of dash line is n value) for 67 vol. % Ti feedstock and 64 vol. % BE Ti64 feedstock at three different temperatures

12

respectively (c-d) Flow activation energy represented as the slopes of linear fit for 67 vol. % Ti feedstock and 64 vol. % BE Ti64 feedstock respectively

Taken from Lin et al. (2017, p. 361)

Arrhenius model does not describe the dependence of viscosity on pressure. Therefore, Cross-William-Landel-Ferry (Cross-WLF) and the second order models are also widely used in PIM to describe the evolution of the feedstock viscosity according to the temperature, the shear rate,

$$\eta = \frac{\eta_0}{1 + (\frac{\eta_0 \dot{\gamma}}{\tau^*})^{1-n}}$$

and the pressure. Cross-WLF presented in equation (

(1.6) is a modified Cross model (initially presented in Eq. 1.4 above) which requires several experimental viscosity profiles (viscosity over the shear rate) obtained at different temperatures (Tim Osswald & Natalie Rudolph, 2014; Poh, 2019).

$$\eta = \frac{\eta_0}{1 + (\frac{\eta_0 \dot{\gamma}}{\tau^*})^{1-n}} \tag{1.6}$$

where the zero shear viscosity is given by the equation ($\eta_0 = C \exp\left(-\frac{A \cdot (T-D)}{B+(T-D)}\right)$

(1.7):

$$\eta_0 = C \exp\left(-\frac{A \cdot (T-D)}{B+(T-D)}\right) \tag{1.7}$$

and where $\eta$ is the melt viscosity (Pa·s), $\eta_0$ is zero shear viscosity refers to the viscosity plateau prior to the onset of shear thinning, $\dot{\gamma}$ is the shear rate (1/s), $T$ is the temperature in kelvin, $\tau*$, $n$, and coefficient $A$, $B$, $C$, and $D$ are the critical stress level at the transition to shear thinning, the power law index in the high shear rate regime, data-fitted coefficients all determined by curve fitting. The second order viscosity fitting model presented in equation (

$$\ln(\eta) = E + F \ln(\dot{\gamma}) + GT + H\left[\ln(\dot{\gamma})\right]^2 + I \ln(\dot{\gamma})T + JT^2$$

(1.8) also describes

the evolution of viscosity according to the temperature and shear rate. This model is used when the viscosity quickly decreases at low shear rates and shows a Newtonian plateau at high shear rates.

$$\ln(\eta) = E + F\ln(\dot{\gamma}) + GT + H\left[\ln(\dot{\gamma})\right]^2 + I\ln(\dot{\gamma})T + JT^2 \tag{1.8}$$

where $\eta$ and $\dot{\gamma}$ are discussed above, $T$ is the temperature in Celsius, and $E$ to $J$ are data-fitted coefficients. Rheological behavior of a PIM feedstock can be measured at different temperatures using a capillary rheometer based on ASTM D3835 for shear rate region ranging from 100 to 10,000 s$^{-1}$ or using a rotational rheometer based on ASTM D4440 for low shear rate region ranging from 0.01 to 1000 s$^{-1}$ (Liu et al., 2002; Xu & Turng, 2011). In a study performed by Côté et al. (Côté, Azzouni, Ghanmi, et al., 2020), the viscosity profiles were characterized using a rotational rheometer for one stainless steel-based and one titanium-based LPIM feedstocks. The parameters of different rheological models were extracted and then implemented in Moldflow software to study the impact of different rheological models on the accuracy of LPIM numerical simulations. The viscosity profiles were fitted by three different models as presented in Figure 1.5a-b. The simulated pressure profiles obtained for the stainless steel-based feedstock were in good agreement with experiments for the three viscosity models (Figure 1.5c) but only for the second-order and matrix models for the titanium-based feedstock (Figure 1.5d) confirming that the selection of rheological models affected the simulated injection pressures.
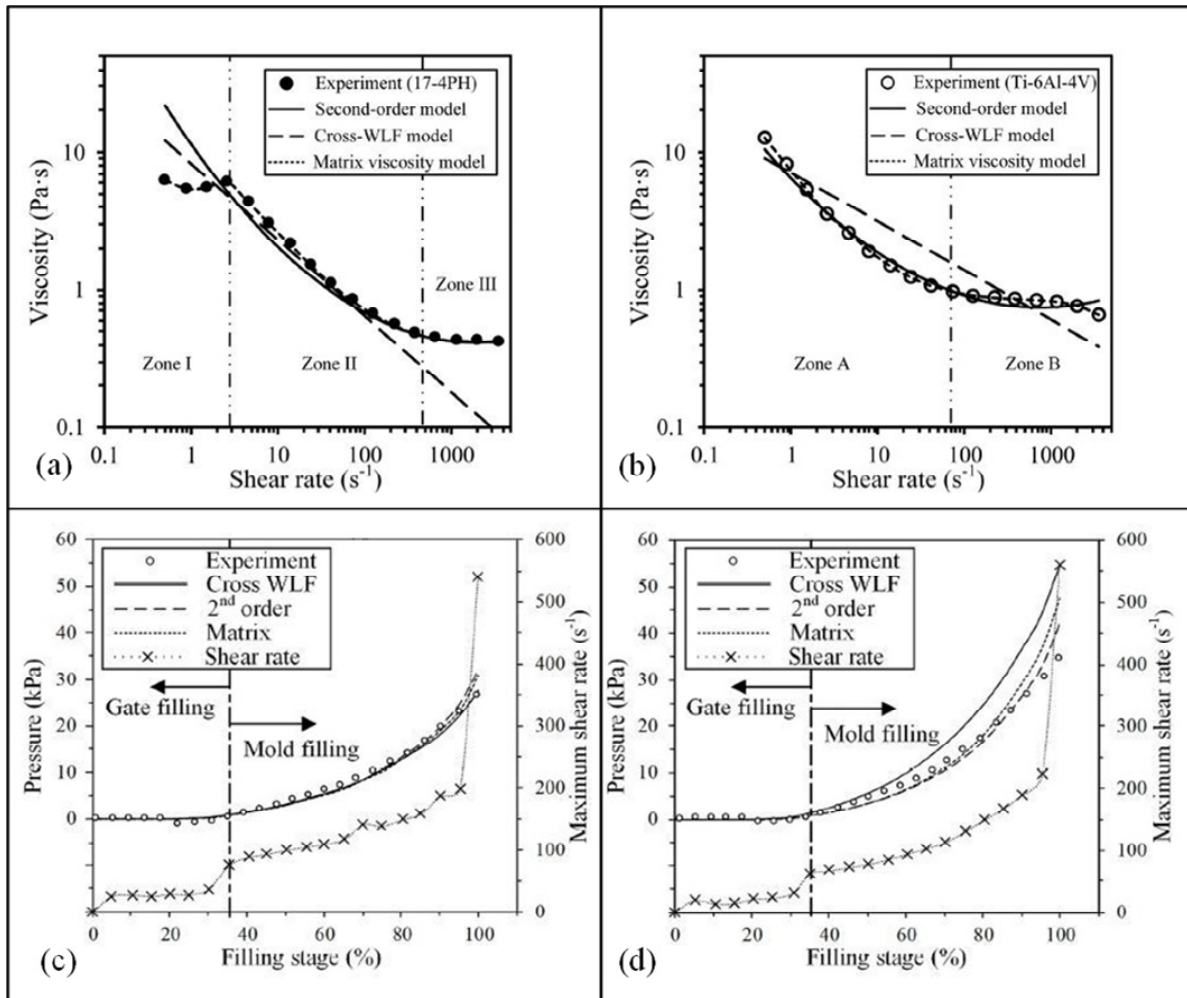
Figure 1.5 Viscosity profiles with superimposed rheological models for (a) stainless steel-based feedstock (b) titanium-based feedstock, and pressures (simulated and experimental) at different filling stages for (c) stainless steel-based (d) titanium-based feedstock
Taken from Côté et al. (2020, pp. 11-14)

### 1.3.1.2 Specific heat capacity

The specific heat capacity ($C_p$) of polymers and feedstocks is generally affected by the temperature, especially near the binder melting point where the value changes drastically as a result of the phase transformation. Furthermore, a PIM feedstock typically contains multiple binder components that may lead to multiple transitions and thus multiple sudden changes in the $C_p$ value. Accordingly, experimental data over the range of processing temperatures is generally required to accurately model the heat transfer of the molten feedstock entering in the

mold cavity (Kate et al., 2014). To that end, Differential Scanning Calorimetry (DSC) measurement using the conventional approach based on three measurements (specimen, empty pan, and sapphire using ASTM E1269 (ASTM-E1269-11, 2018)) or a new approach based on a single measurement (Modulated DSC experiments according to ASTM E2716 (ASTM-E2716-09, 2014)) is utilized. Binet et al. (Binet et al., 2005) simulated the injection stage of a metallic-based feedstock using commercial FEM software. In this study, specific heat capacity of the feedstock was evaluated with a Perkin-Elmer DSC in the temperature range between 20 and 180°C. Figure 1.6 shows data recorded during heating and cooling steps and the two peaks at about 56 and 135°C which indicate the melting points of the binder components. The specific heat capacity then was implemented into the simulation software as one of the inputs to predict the material flow of the molded part. The good agreement between numerical and simulation results was attributed to the accurate characterization of the MIM material.
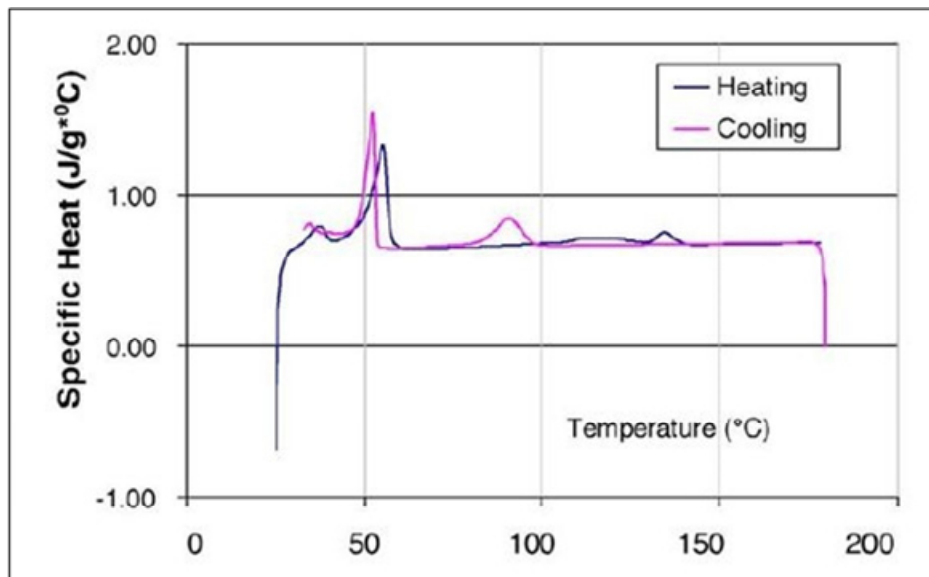


Figure 1.6 Specific heat vs. temperature obtained for stainless steel-
based feedstock
Taken from Binet et al. (2005, p. 1163)

### 1.3.1.3 Thermal conductivity

Thermal conductivity is another physical property used in numerical simulations to characterize the ability of the feedstock to transfer heat. During molding stage, a hot feedstock generally around 80-150°C is injected into relatively cold mold of about 30-60°C. Since the feedstock is gradually in contact with the mold, the feedstock transfers its heat to the mold as the part cool down. Thermal conductivity is defined by Fourier's law stating that the time rate of heat transfer through a material is proportional to the negative gradient in the temperature and to the area, at right angles to that gradient, through which the heat flows which can be written as equation ($\vec{q} = -k \cdot \nabla T$                                    (1.9):

$$\vec{q} = -k \cdot \nabla T \qquad\qquad (1.9)$$

Where $\vec{q}$ is the vector of local heat flux density in W/m², $k$ is the material conductivity in W/m¹·K¹ and $\nabla T$ is the temperature gradient in K/m¹. There are different mathematical forms of the "rule of mixtures" theory to calculate the thermal conductivity of metallic-based feedstocks. In a study performed by Kowalski et al. (Kowalski et al., 1999), two existing mathematical models (theoretical Maxwell and semi-theoretical Lewis & Nielsen) were used to calculate the thermal conductivity of the stainless steel-based feedstock that were compared with experimental results obtained by the laser flash method. Figure 1.7a-b present the thermal conductivity of 316L stainless steel and binder system as a function of temperature respectively. Figure 1.7c-d present the calculated (Maxwell- and Lewis & Nielsen models) and the measured thermal conductivity of the feedstock respectively. The Maxwell model substantially underestimated the measured values of the thermal conductivity. Lewis & Nielsen's semi-theoretical model appears to better predict the thermal conductivity of the PIM feedstock. They also concluded that the accuracy of the calculated values is inadequate for numerical simulation purposes, and experimental measurements of this property must be performed.
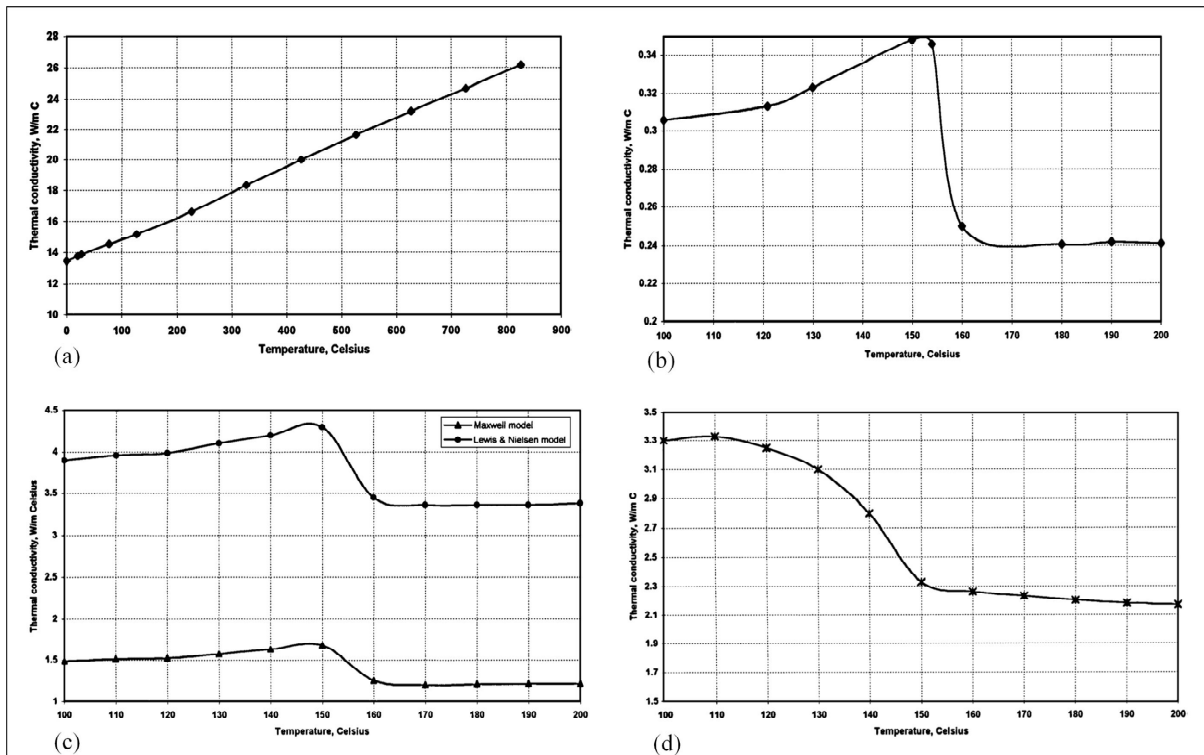
Figure 1.7 Thermal conductivity of (a) the 316L steel (b) the binder system (c) the calculated
models (d) the feedstock
Taken from Kowalski et al. (1999, pp. 2-4)

### 1.3.1.4 Density

Solid loading is defined as the volumetric ratio of powder to the total volume of feedstock (i.e.,
powder and binder). At low solid loading, the measured density usually follows the theoretical
density line, but when it reaches critical value the measured density deviates from the
theoretical line (Qu et al., 2005). Therefore, by measuring the feedstock density with
incremental increase in solid loading, a critical solid loading can be determined as shown in
Figure 1.8. Critical solid loading is reached when the powder particles in the feedstock are
packed as tightly together as possible with all the voids between particles filled with binder
(Poh, 2019). Density of the feedstock can be measured by either gas displacement method or
water immersion method. Majdi et al. (Majdi et al., 2021) performed a study on the properties
of low-viscosity iron-based feedstocks used in low-pressure powder injection molding. In this
study, they used a helium gas pycnometer to determine the critical and maximum solid loading

by determining this threshold value where the experimental point diverges from the theoretical calculation. Maximum solid loading (indicated by a white arrow in Figure 1.8) was set at 1 vol. % below critical solid loading.
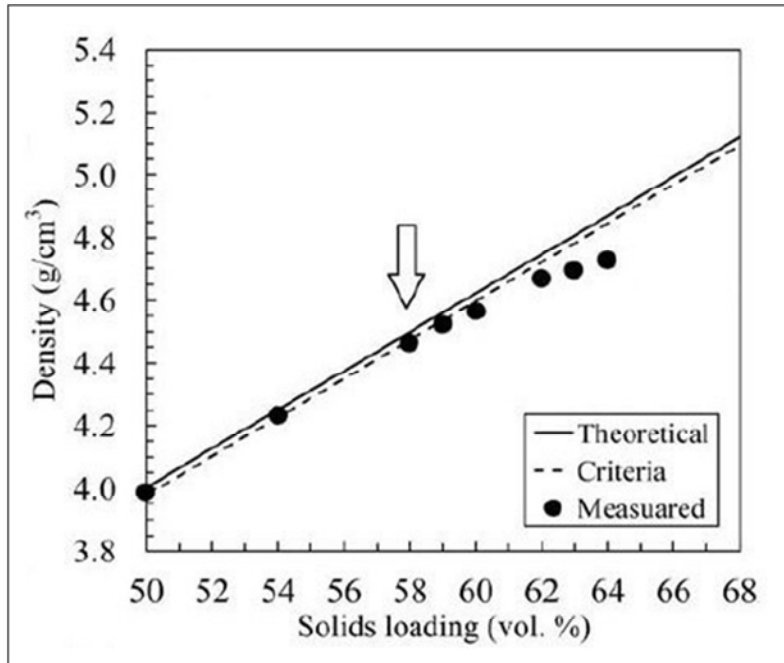


Figure 1.8 Determination of the critical and maximum solid
loading of the feedstock
Taken from Majdi et al. (2021, p. 5)

### 1.3.2    Comparison between PIM numerical simulation software

The numerical simulation of the PIM injection stage has been of interest to several researchers since it helps predict the behavior of a powder-binder mixture in a cavity without going through long and expensive experimental stages. The simulation packages available are listed in Table 1.2. These numerical tools use different rheological models, domains (2.5D or 3D), or methods for solving the governing equations and finally predict mold-filling behavior of the feedstock. The most common methods are finite element method (FEM), finite difference method (FDM), and finite volume method (FVM) (Raymond, 2012).

Table 1.2 Comparison between PIM simulation software
Adapted from Azzouni (2020, p. 18)

| Software | Domain | Method | Model |
|----------|--------|--------|-------|
| ANSYS | 3D | FVM / FEM | Cross |
| Moldex3D | 3D | FVM | Carreau Yassuda, Cross WLF |
| Moldflow | 3D | FEM | Cross WLF, Second order |
| PIMSolver | 2.5D | FEM / FDM | Cross WLF |
| ProCAST | 3D | FEM | Carreau Yassuda |
| Sigmasoft | 3D | FEM | Cross WLF |

Mold filling simulations are performed using Computational Fluid Dynamics (CFD) principles based on solving the equations of conservation of momentum, mass, and energy. The equations $(\frac{\partial \rho}{\partial t} + \nabla \cdot (\rho \boldsymbol{u}) = 0$ (1.10) to $(\beta = -\frac{1}{\rho}\frac{\partial \rho}{\partial T}$ (1.14) describe the motion of a fluid in non-isothermal conditions. Moldflow software discretizes these equations into finite elements to simulate the flow inside the mold cavity.

Conservation of mass:

$$\frac{\partial \rho}{\partial t} + \nabla \cdot (\rho \boldsymbol{u}) = 0 \tag{1.10}$$

Conservation of momentum:

$$\rho \frac{D\boldsymbol{u}}{Dt} = -\nabla p + \nabla \cdot \boldsymbol{\tau} + \rho \boldsymbol{g} \tag{1.11}$$

$p$ is the pressure, $t$ is the time, $\rho$ is the density, $\boldsymbol{u}$ is the velocity vector, $\boldsymbol{g}$ is the gravitational acceleration, and $\boldsymbol{\tau}$ is the viscous stress tensor. For the pressure-velocity (momentum and mass conservation) solution, the equations are solved by a standard finite element method which includes the material compressibility in all process stages. The beam and tetrahedral elements are solved simultaneously. In beam elements, a 1D flow is assumed and a Hele-Shaw approximation is used. In tetrahedral elements, a full Stokes solution is performed (or Navier-Stokes if the inertia option is selected).

Conservation of energy:

$$\rho C_p \frac{DT}{Dt} = \nabla \cdot (k\nabla T) + \boldsymbol{\tau} : \nabla \boldsymbol{u} + \beta T \frac{Dp}{Dt} \tag{1.12}$$

where the material derivative is defined by:

$$\frac{D(\cdot)}{Dt} = \frac{\partial(\cdot)}{\partial t} + \boldsymbol{u} \cdot \nabla(\cdot) \tag{1.13}$$

$T$ is the absolute temperature, $C_p$ is the specific heat, $k$ is the thermal conductivity, and $\beta$ is the polymer expansivity, which is defined as follows:

$$\beta = -\frac{1}{\rho}\frac{\partial \rho}{\partial T} \tag{1.14}$$

For the temperature (energy conservation) solution, equations are solved by a standard finite element method. The shear heating, convection, conduction, and compressive heating terms are included for both beam and tetrahedral elements. When solving the temperature equations, the time-step is broken into a number of shorter sub-steps for increased accuracy. At each time-step, the software iterates between the temperature and pressure-velocity equations until

convergence is reached. The following subsections present a review of previous MIM simulation studies using the software presented in Table 1.2.

### 1.3.2.1    ANSYS

Zheng and Qu (Zheng & Qu, 2006) used ANSYS package for the first time to simulate MIM process. Their numerical results presented in
Figure 1.9a exhibited a region where the feedstock temperature was higher than the initial inlet temperature. They attributed this phenomenon to viscous heating. They also predicted areas of possible weld line in the mold as confirmed in
Figure 1.9b. However, these results were not validated due to complexity in the mold design and high cost.
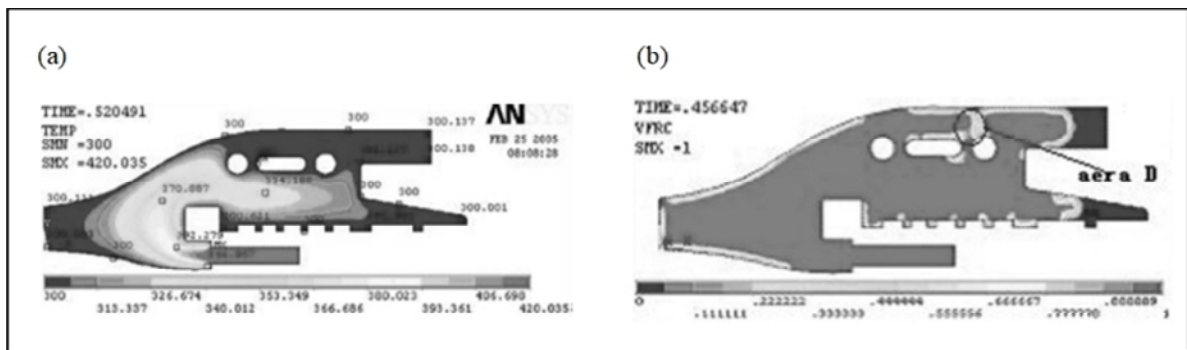


Figure 1.9 (a) Temperature distribution at the end of filling stage (b) possible weld line location
Taken from Zheng & Qu (2006, pp. 169-171)

Liu et al. (Liu et al., 2018) studied the effects of wall slip on the rheological behavior of ZrO2 feedstock flowing through the micro spool mandrel mold. In this study, a power-law wall slip model was established to simulate the pressure through the cavity during injection stage. The simulation including wall slip Figure 1.10b showed high-pressure gradient near the cylinder and generally lower pressure gradient distribution during filling as compared to the simulation excluding wall slip Figure 1.10a. Experimental results presented in Figure 1.10c-d showed the appearance of the cracks on the surface of the cylinder when the micro post was completely filled without visible defects after the injection. Since pressure gradient exerts influence on the

quality of the molded micro components, this research group concluded that the simulation including wall slip yielded better prediction for the pressure gradient.
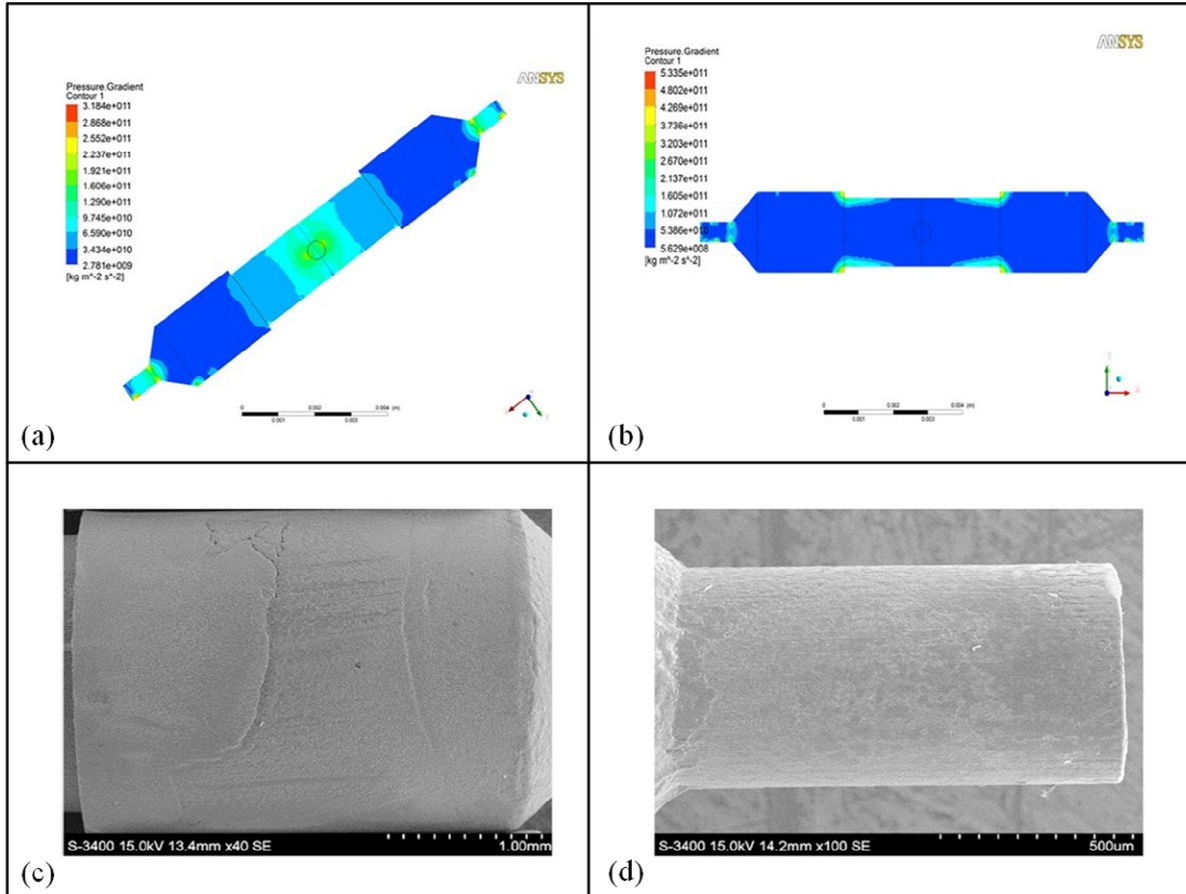


Figure 1.10 Pressure gradient distribution of the part when (a) excluding wall-slip (b) including wall-slip, and (c-d) cylinder and micro post on an injection molded part
Taken from Liu et al. (2018, pp. 16284-16285)

### 1.3.2.2    Moldex3D

Tseng et al. (Tseng et al., 2014) used Moldex3D to predict the powder concentration distribution during mold filling as an indicator for phase separation to discuss black lines appearance on injected molded parts in the MIM process. In this study, a suspension balance model was added to Moldex3D software as the powder concentration function to simulate black lines on the final part. Figure 1.11a shows the powder concentration pattern of the part

obtained by the software. Most of the surface concentration is almost uniform. However, there is a binder-rich zone, especially around the vicinity of the gate. This research group concluded that this area might be a black line due to extreme shear rates in the gate region, as shown in Figure 1.11b. However, their simulation results were not validated by real-scale injections.
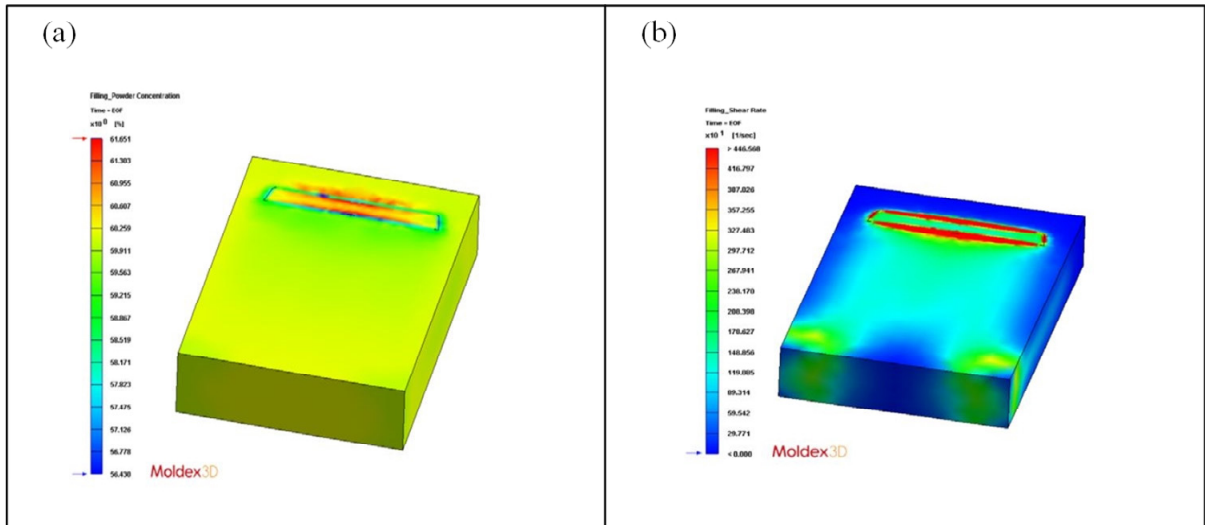


Figure 1.11 (a) Powder concentration pattern during MIM filling of the part for the average volume fraction of 60 vol. %. (b) Shear rate pattern during MIM filling of the part for the average volume fraction of 60 vol. %
Taken from Tseng et al. (2014, pp. 4-5)

Bandiwadekar (Bandiwadekar, 2017) conducted a study on designed micro-pillar array geometry with high-viscosity lead-zirconate-titanate feedstock using Moldex3D. In this study, the defect of broken micro-pillar occurring during sintering was attributed in fact to the variation in powder concentration captured during numerical simulations of the filling stage as illustrated in Figure 1.12. This author concluded that the lower powder concentration at the bottom of micro-pillar leads to a non-uniform shrinkage during debinding and sintering and resulting in neck formation in this region of low powder concentration that was finally more susceptible to failure.
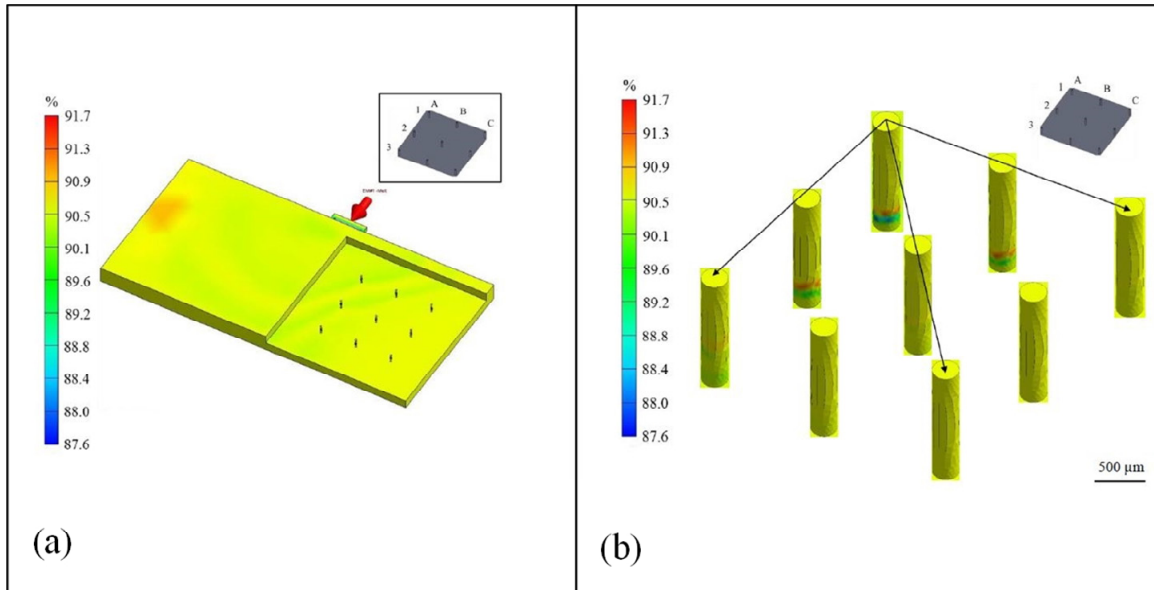
Figure 1.12 Powder concentration of (a) filled and packed microarray, and (b) within
individual micro-pillars
Taken from Bandiwadekar (2017, pp. 31-32)

### 1.3.2.3 Moldflow

Moldflow software has been used by several research groups to simulate the HPIM process. Bilovol et al. (Bilovol et al., 2003) compared MoldFlow with ProCAST and C-Mold packages to assess their accuracy of mold filling predictions. In this study, the numerical simulations of the flow pattern in the cavity obtained by these packages were compared with the experimental results obtained by means of short shot Figure 1.13. The predictions of the flow pattern obtained by Moldflow were more accurate than the other two numerical tools. The differences between experimental observations and the numerical results were attributed to the lower injection rate during the experimental short shots.
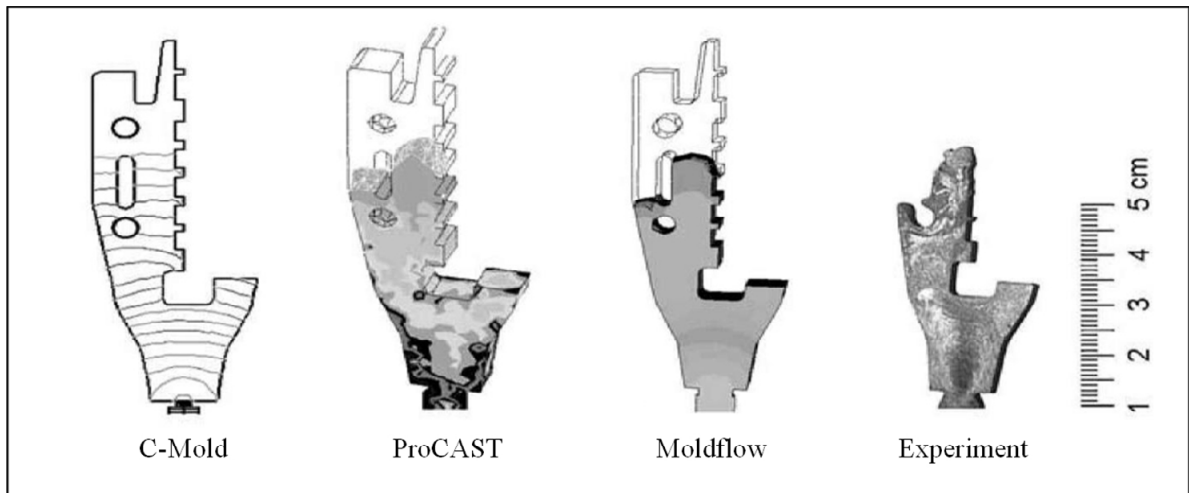
Figure 1.13 Simulated filing patterns compared to experimental result

Taken from Bilovol et al. (2003, p. 57)

Lenz et al. (Lenz et al., 2014) used Moldflow to evaluate the feasibility of powder injection molding to fabricate silicon nitride engine components. This research group identified the critical parameters affecting a ceramic-based HPIM feedstock during injection molding of a complex part. The fill behavior of the feedstock at different filling stages illustrated in Figure 1.14a-c shows smooth filling of the part without any observable defects. As shown in Figure 1.14d, the simulation results showed the melt temperature is the dominant factor affecting the injection pressure.
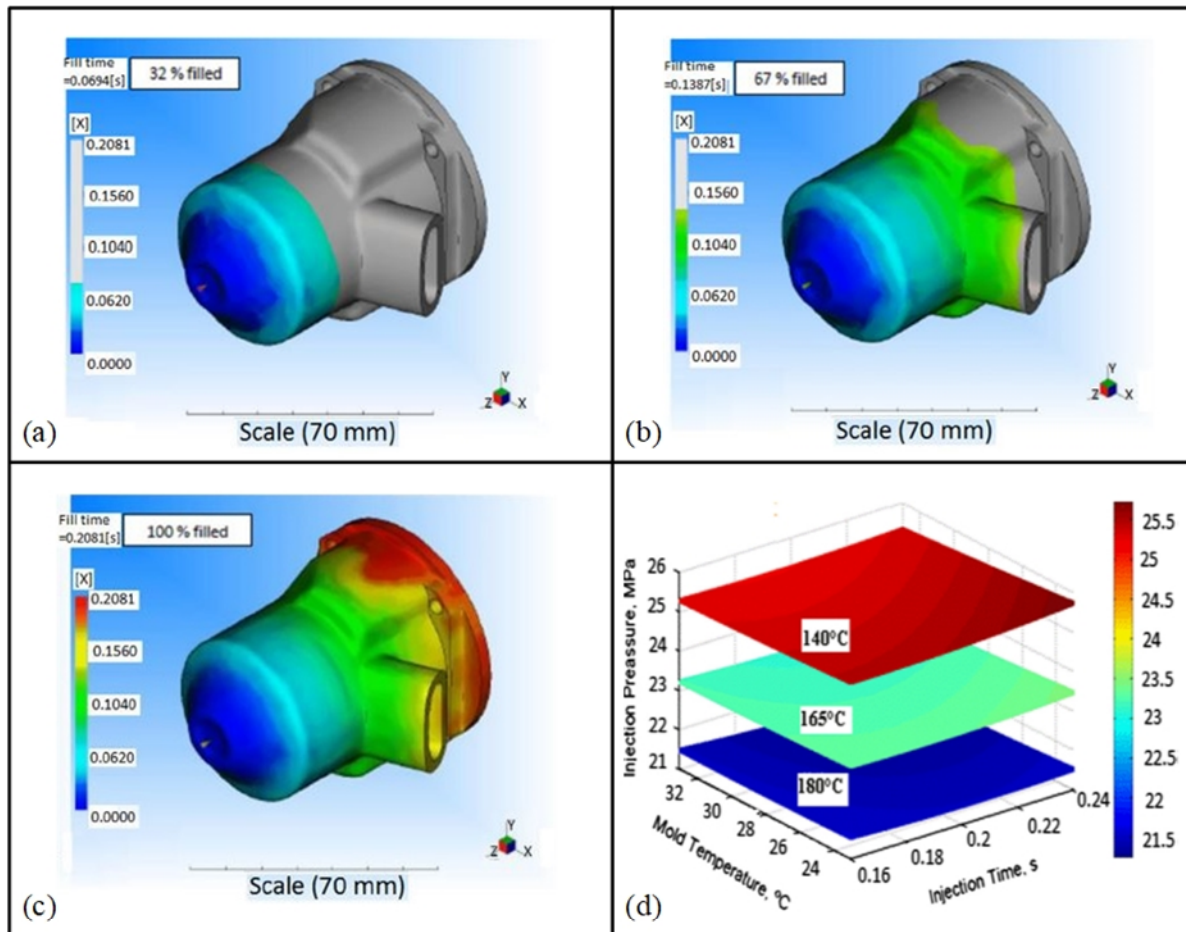
Figure 1.14 (a-c) Simulation of the filling behavior of the feedstock in the combustion engine mold cavity (d) variation of injection pressure according to different process parameters
Taken from Lenz et al. (2014, pp. 897-898)

Moldflow has also been used recently to simulate the injection step of the LPIM process for ceramic-based and metal-based feedstocks. Sardarian et al. (Sardarian et al., 2016c) simulated and experimentally validated the filling stage for an alumina-based LPIM feedstock . In this study, liquid state jetting was observed during the cavity filling at high injection temperatures and high pressures producing many voids in the injected molded parts. Laminar flow patterns exhibiting no jetting were predicted by the model Figure 1.15a-b. However, jetting predicted by the model leads to defects within the injected parts Figure 1.15c-d.
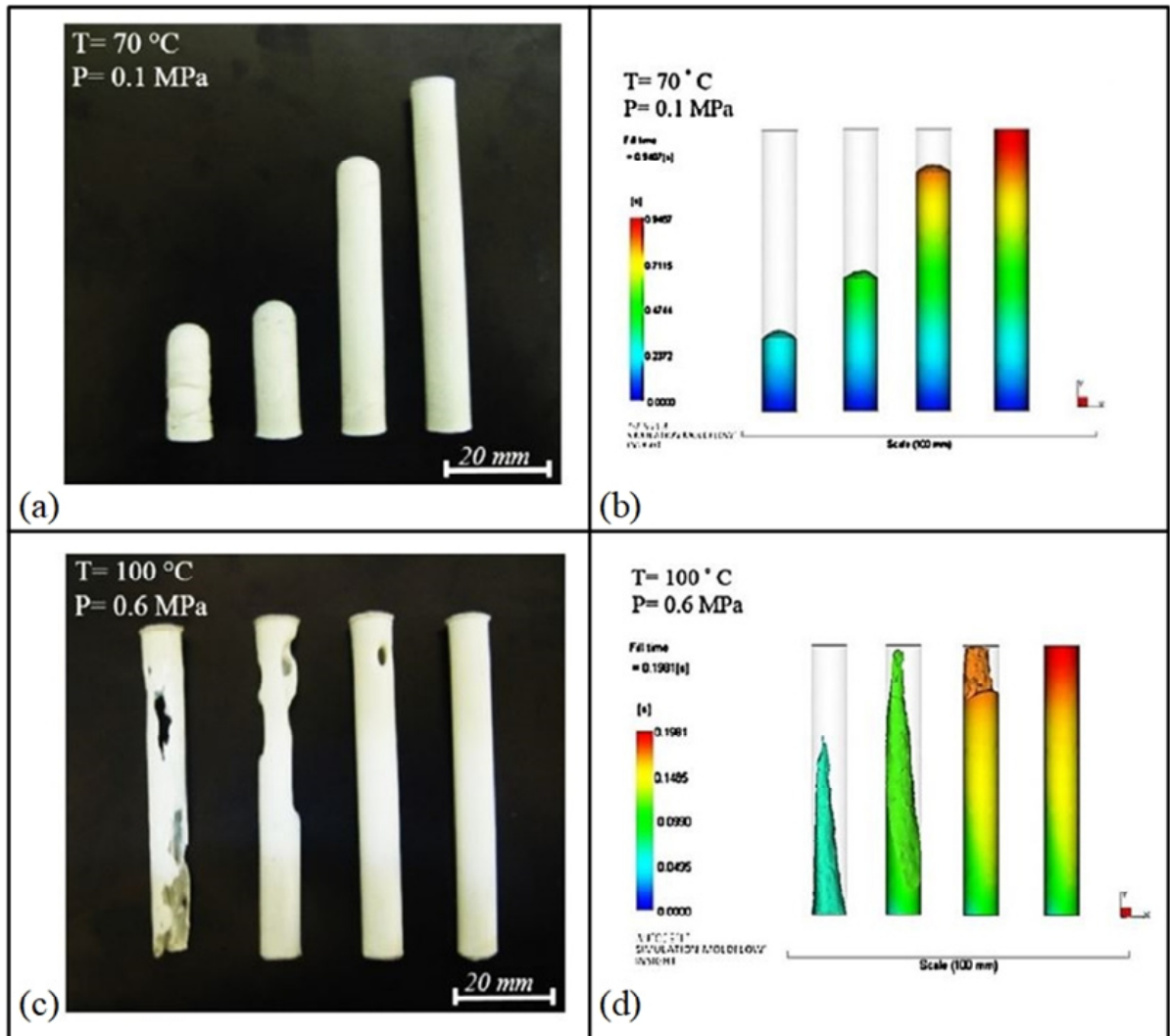
Figure 1.15 Mold cavity filling and simulation results of (a-b) uniform filling (c-d) jetting filling
Taken from Sardarian et al. (2016, p. 376)

Ben Trad et al. (Ben Trad et al., 2020) used Moldflow to simulate the mold filling behavior of a metallic-based LPIM feedstock which was validated using real-scale injections. In this study, the injected length and the filling times predicted by the numerical model were in good agreement with the experimental observations Figure 1.16a-b. Since the injections were performed and simulated at constant volumetric flow into a constant cross-section mold cavity, the mold filling results confirmed that the feedstock temperature has no influence on the injected lengths, but rather, on the injection pressure obtained in Figure 1.16c.
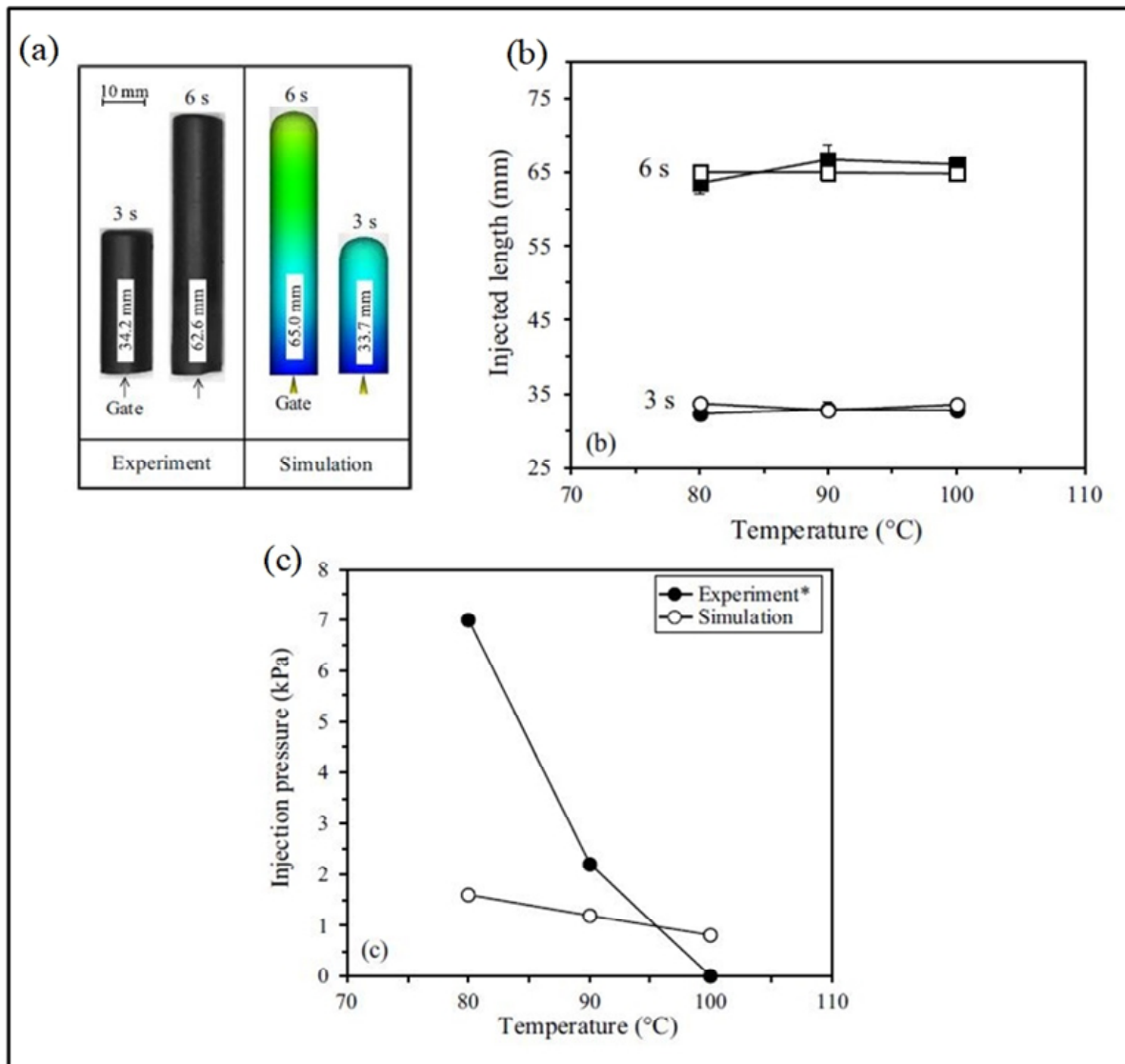
Figure 1.16 Experimental and simulated (a-b) injected length, (c) injection pressure
Taken from Ben Trad et al. (2020, pp. 1355-1356)

Azzouni et al. (Azzouni et al., 2021) simulated injected length and injection pressure using different mold cavities and thicknesses, and feedstock temperatures. The comparison between simulated and real-scale injections confirmed that the injected lengths were not influenced by the feedstock temperature, but only by the shape of the mold cavity since the experimental and simulated injections were performed at constant volumetric flow Figure 1.17a-b. The simulated pressure profiles presented in Figure 1.17c were in good agreement with experimental results

over the majority of the mold filling range. In this study, the simulation capability of Moldflow package for the injection pressure of LPIM feedstock was validated experimentally for the first time.
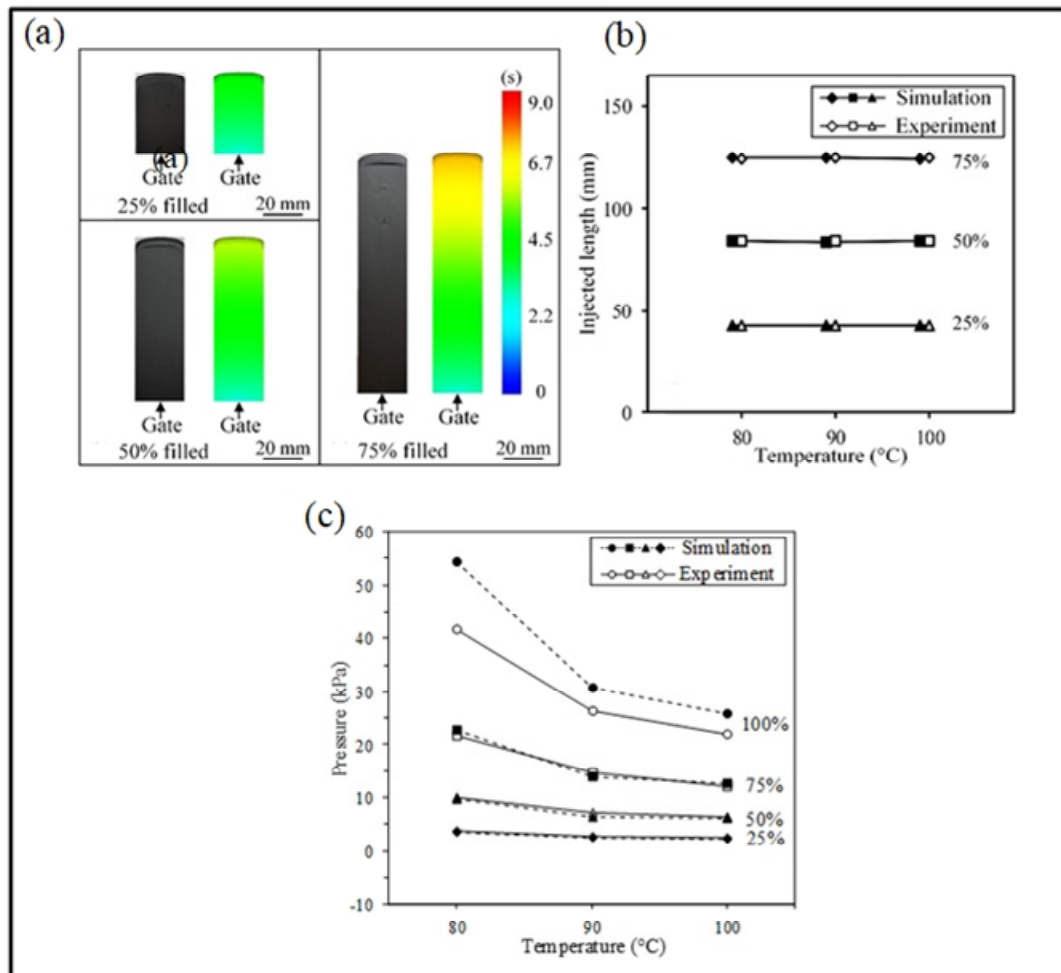


Figure 1.17 Experimental and simulated (a-b) injected lengths, (c) pressure profiles
Taken from Azzouni et al. (2021, pp. 967-968)

### 1.3.2.4 PIMSolver

Ahn et al. (Ahn et al., 2008) used PIMSolver to study the importance of slip phenomena and the coupled analysis between the filling/packing and cooling stages. The pressure profiles obtained from simulations were compared to the experimental results. The simulated pressure

30

profiles were obtained from the filling and packing analyses at a constant cavity wall temperature without and with consideration of slip layer. It was shown that the simulation results obtained from filling/packing analysis with slip layer are better fitted to the experimental data than no slip condition Figure 1.18a-b. The authors also considered cavity wall temperature distributions of cooling analysis (coupled analysis) in their simulations and obtained more accurate simulation results Figure 1.18c-d. This research group attributed the increase in accuracy to the fact that viscosity and slip layer of powder–binder mixture highly depend on temperature.
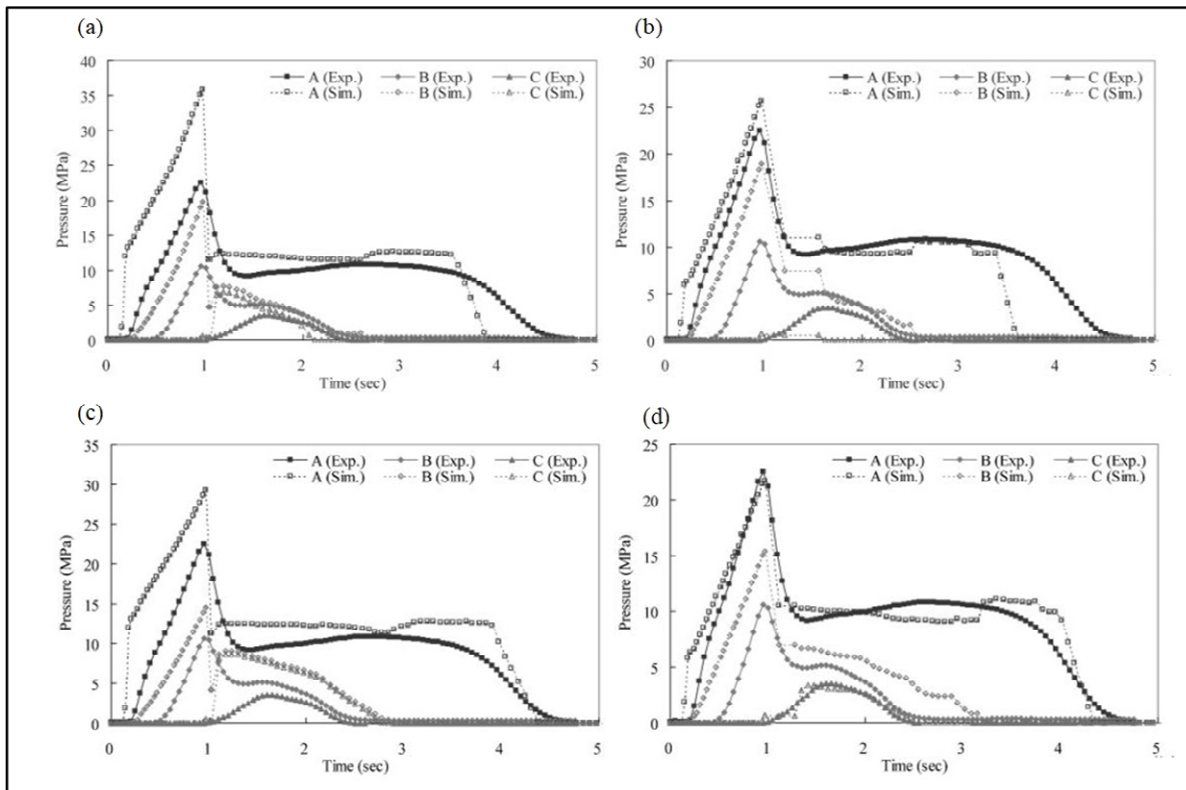


Figure 1.18 Experimental and simulated pressure profiles with constant wall temperature (a) without slip layer (b) with slip layer, and experimental and simulated pressure profiles with cavity wall temperature distributions (c) without slip layer (d) with slip layer
Taken from Ahn et al. (2008, p. 324)

### 1.3.2.5    ProCAST

Using ProCAST simulation package, Sardarian et al. (Sardarian et al., 2016a) studied the effects of injection temperature and pressure on the properties of alumina-based LPIM feedstock. Results showed that increase in injection temperature and pressure and the resulting increase in flow rate leads to the formation of void. The formation of void during the filling stage was attributed to occurrence of jetting and this phenomenon was captured by the software Figure 1.19a. In this study, the SEM micrographs showed that an increase in injection temperature may result in evaporation of binder components Figure 1.19b (Arrows mark the presence of binder evaporation).
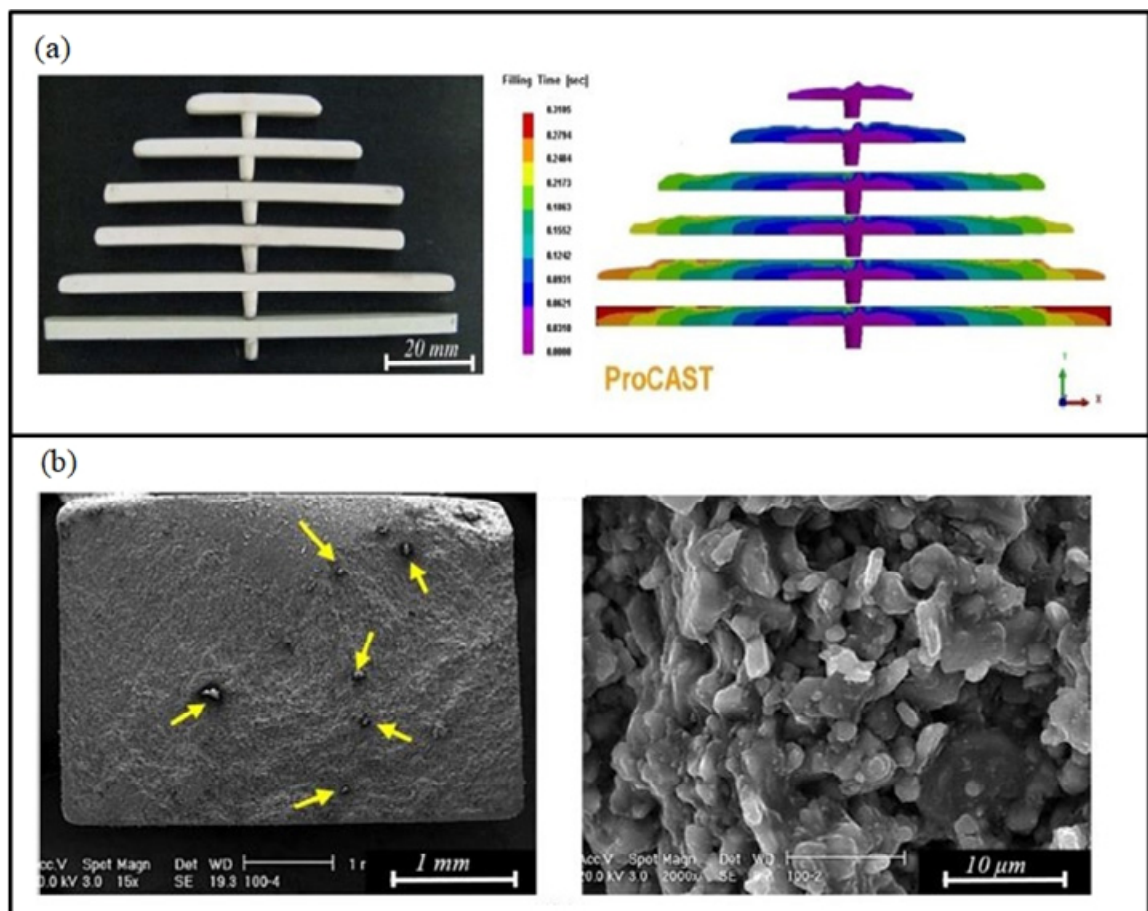


Figure 1.19 (a) Experimental and simulated flow pattern (b) the SEM micrograph of the fracture surface
Taken from Sardarian et al. (2016, pp. 4790-4791)

### 1.3.2.6 Sigmasoft

Mulser et al. (Mulser et al., 2011) used Sigmasoft to predict and visualize the material contact for metallic-based feedstocks during a simultaneous injection method (also called co-injection). The injection parameters (feedstock temperature, packing pressure) were varied systematically to analyze their influence on the material contact and the interface that is formed after co-injection. In this study, the feedstock with lower temperature was pressed into the feedstock with higher temperature. Obviously, the feedstock of higher temperature maintained its temperature and was replaced by the 10°C colder feedstock due to its lower viscosity Figure 1.20a. The feedstock pressurized with lower packing pressure was replaced by the feedstock of higher packing pressure Figure 1.20b. The simulations obtained by this group showed the same trends as the experimental results Figure 1.20.
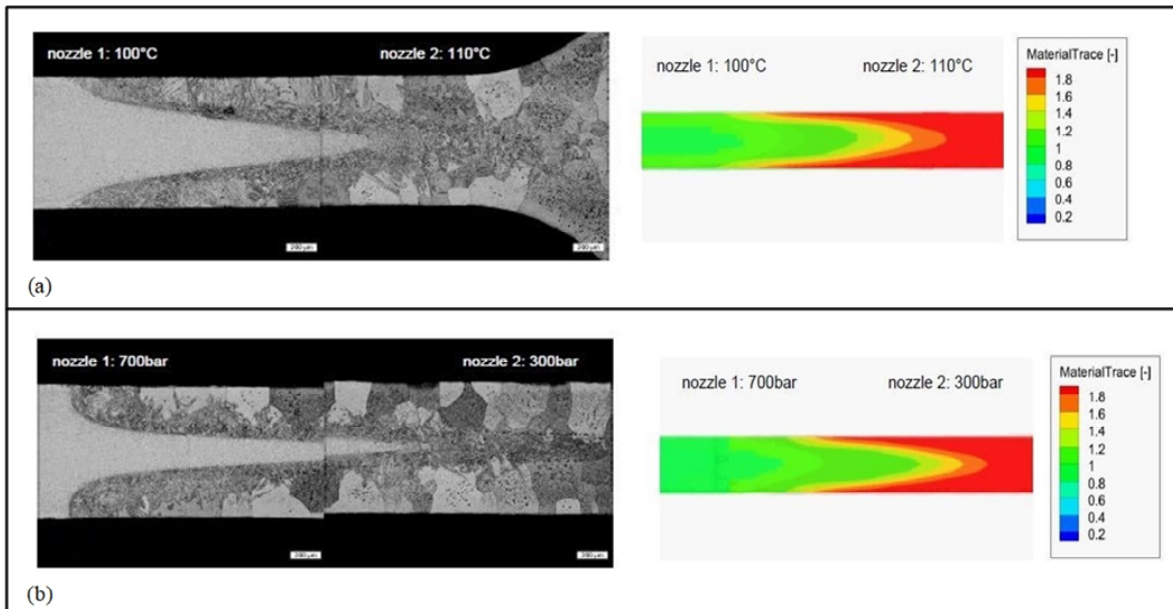


Figure 1.20 Experimental and simulated co-injection with different (a) feedstock
temperatures, (b) packing pressures
Taken from Mulser et al. (2011)

# CHAPTER 2

## Problem definition and research objectives

### 2.1    Problem definition

The literature review has shown that numerical simulation can be used successfully to predict the flow behavior of the powder-binder mixture during the injection stage of the PIM process. Using this tool, it is possible to optimize the process parameters in order to minimize design defects of the molds before starting the production stage, to reduce the costs of calibration tests, and finally accelerate the industrialization phases of new PIM parts. So far, the vast majority of numerical simulation studies have been carried out on the PIM process using conventional high-viscosity feedstocks (also known as HPIM process). However, there is only few studies on the LPIM process that uses low-viscosity mixtures. In addition, and to the best of the author's knowledge, measurement and experimental validation of the simulated pressure values for LPIM process has been performed only once in two simple shapes 2D mold cavities using Moldflow. Therefore, experimental validation of such low-pressure obtained numerically within more complex shape mold cavities has never been confirmed for this family of low-viscosity ceramic- or metallic-based feedstocks.

### 2.2    Research objectives

The objective of this work is to evaluate the capability of a commercial numerical simulation package to capture the influence of process parameters on injection pressure. The following specific objectives are stated:

- Define the material law (viscosity profiles, density, specific heat vs. temperature, and thermal conductivity vs. temperature) required in Autodesk Moldflow Synergy
- Evaluate numerically the flow patterns and pressure at different filling stages for various injection parameters (different mold cavities, mold temperatures, melt temperatures, and feedstock formulations).
- Validate numerical results by experimental injections

# CHAPTER 3

## Methodology

This chapter provides an overview of the methodology used to carry out this project including the steps and the equipment used to characterize the feedstock as well as the details about the simulations and process parameters used to obtain the experimental results. Other methodological details are also available in the article presented in Chapter 4.

### 3.1 Feedstock preparation

#### 3.1.1 Metallic powder

In this study, two 17-PH stainless steel powder lots produced from gas-atomization (Sandvik Osprey, United Kingdom) and water-atomization (Epson Atmix Corporation, Japan) were used. The particles morphology was observed with a scanning electron microscope (Hitachi 3600, secondary electrons detector) and the particle size distribution was measured using a laser diffraction particle analyzer (Beckman Coulter LS 13 320) presented in Figure 3.1a-b. Gas atomized powder exhibits spherical shapes with an average particle size of about 12 μm (Figure 3.1c), while water-atomized powder shows a blend of spherical and ligamental particles with an average particle size of 11 μm (Figure 3.1d). Particle size in the $10^{th}$, $50^{th}$, and $90^{th}$ (i.e., $D_{10}$, $D_{50}$, and $D_{90}$) extracted from Figure 3.1e-f were reported in Table 3.1.
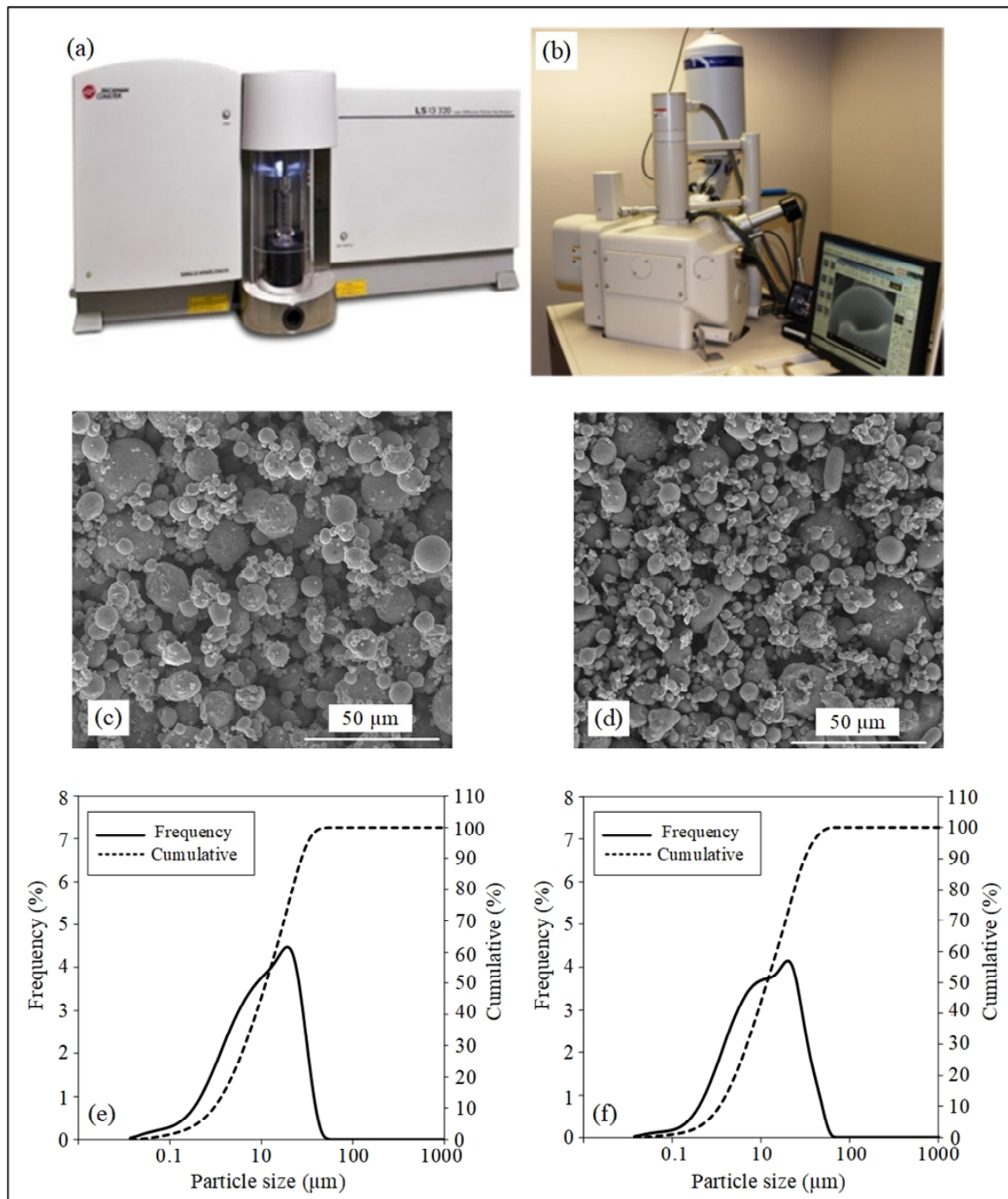
Figure 3.1 (a) Scanning electron microscope (Hitachi 3600, secondary electrons detector), (b) diffraction particle analyzer Beckman Coulter LS 13 320 laser, (c-d) SEM observations of the dry powder, and particle size distributions of 17-4PH dry powders produced by (e) gas-atomization, and (f) water-atomization

Table 3.1 17-4 PH powder characteristics

| Powder lot | Atomization technique | Density (g/cm$^3$) | $D_{10}$ (μm) | $D_{50}$ (μm) | $D_{90}$ (μm) | Supplier |
|---|---|---|---|---|---|---|
| PF-20F | Water | 7.8 | 3.4 | 11.8 | 31.3 | Atmix |
| S17700 | Gas | 7.8 | 3.0 | 11.3 | 27.5 | Osprey |

### 3.1.2 Polymeric binders

Water-atomized and gas-atomized stainless steel 17-4PH powders were combined with wax-based binder at 60 and 65 vol. % of powder to formulate a total of four feedstocks. During this step, all constituents were blended into a mixer and then heated at a temperature slightly above the binder melting point under vacuum to promote powder coverage, remove air bubbles, and produce homogeneous feedstock. In this study, binder constituents were selected due to their extensive use in LPIM. Paraffin wax and carnauba wax were used as the main carrier and shrinking agent to improve the material flowability (Ahn et al., 2009). Ethylene vinyl acetate was used as a thickening agent to increase the viscosity of the feedstock, prevent the powder-binder separation, and increase the strength of the green parts after the injection (Ghalya, 2018). Stearic acid was used as a surfactant agent to promote powder wetting by lowering the surface energy of the binder-powder interface (Kong, 2011).

## 3.2 Feedstock characterization

### 3.2.1 Viscosity

Feedstock viscosity was measured using an Anton Paar MCR 302 rotational rheometer using the concentric-cylinder (CC-17) and a Peltier temperature-controlled (C-PTD 200) measuring system presented in Figure 3.2a. In this study, molten feedstock was poured into the rheometer concentric cylinder before to introduce a bob mandrel (illustrated in Figure 3.2b) and tested at shear deformation rates ranging from 0.5 to 3500 s$^{-1}$ under constant temperature condition varying from 80 to 100°C. Based on the methlogy developed by Fareh et al. (Fareh et al.,

2017), the viscosity profiles were obtained by repeating each condition three times to calculate average viscosity.
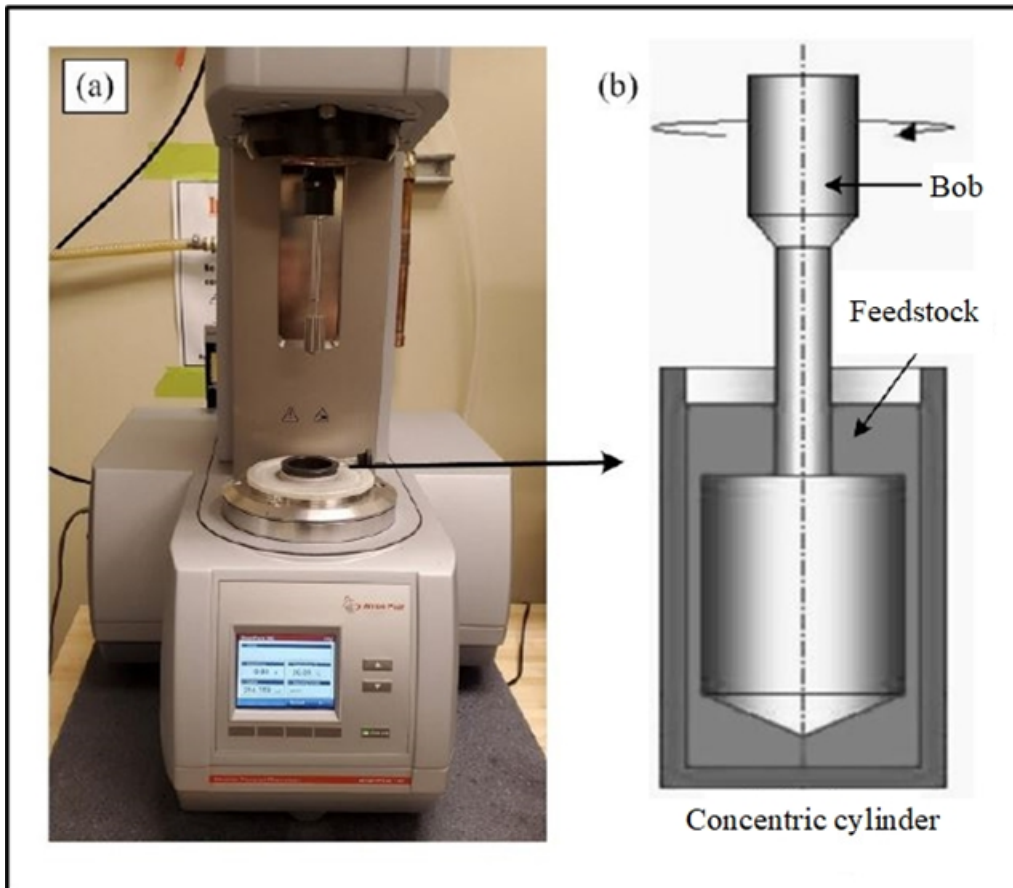


Figure 3.2 (a) Anton Paar MCR 302 rotational rheometer (b) schematic representation of the measurement system CC-17

### 3.2.2    Thermal properties

Based on the standard test method ASTM D3418-15, the melting point of each single binder constituent and feedstock were obtained using the differential scanning calorimeters (DSC) Discovery DSC 2500 (TA instruments) illustrated in Figure 3.3a. Specimens were heated from 20 to 120°C using a heating rate of 10°C/min under a nitrogen gas flow rate of 50 ml/min. The specific heat capacity was measured using the same DSC based on ASTM E1269 using the $T_{zero}$ technology providing a direct heat capacity measurement instead of the three measurements required by the traditional approach. The feedstock thermal conductivity ($k$)

was measured with the Trident measurement system (C-Therm Technologies Ltd) reported in Figure 3.3b according to ASTM D7984-16.
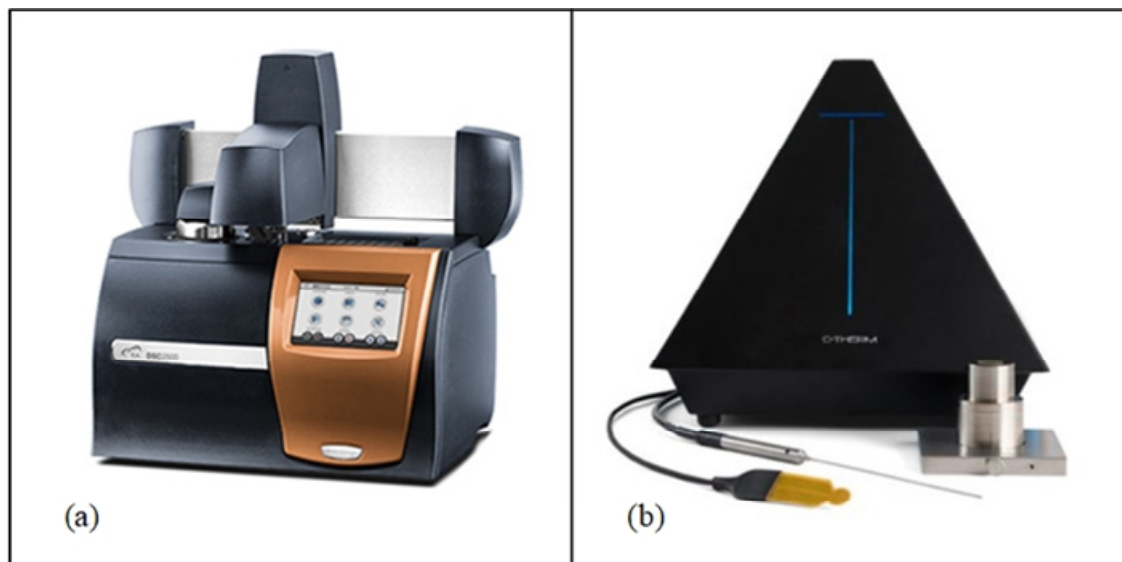


Figure 3.3 (a) differential scanning calorimeters (DSC) Discovery DSC 2500 (TA instruments), and (b) Trident measurement system (C-Therm Technologies Ltd)

### 3.2.3    Density

The density of the metallic powder, binder, and feedstock were measured following the ASTM B923–16 standard using the helium gas pycnometer (AccuPyc II 1340) illustrated in Figure 3.4. The sample weight was measured prior to the test on a precision balance to allow the calculation of the density. During the test, the sample was placed in a 10 cm$^3$ cup which was then placed into the sample chamber. Gas was introduced to the sample chamber and then expanded into a second empty chamber. The sample volume was calculated using the Eq. 3.1 by recording the pressure before and after an increase of the total volume:

$$V_{sample} = V_{chamber} - V_{ref} \cdot \left(\frac{P_2}{P_1 - P_2}\right) \tag{3.1}$$

where $V_{sample}$ is the volume of the sample, $V_{chamber}$ is the volume of the sample chamber, $V_{ref}$ is the volume of the reference chamber, $P_1$ is gauge pressure when the $V_{chamber}$ and $V_{ref}$ are not connected, and $P_2$ is gauge pressure when the $V_{chamber}$ and $V_{ref}$ are connected
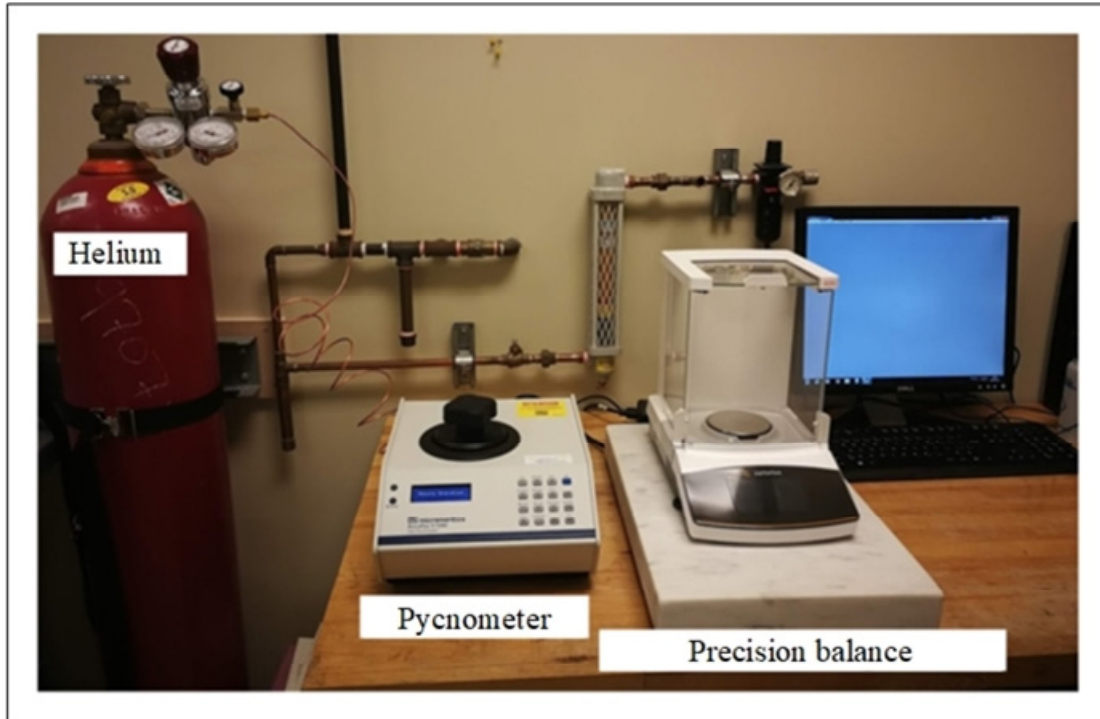


Figure 3.4 Helium gas pycnometer (AccuPyc II 1340)

## 3.3      Numerical simulations and experimental validations

### 3.3.1      Numerical simulations

Recent studies on PIM numerical simulations (Azzouni et al., 2021; Ben Trad et al., 2020; Sardarian et al., 2016b; Zhang & Lin, 2007) indicate that Moldflow (Autodesk inc.) is suitable for predicting the mold filling behavior of LPIM feedstock. Therefore, this software was selected for this study. The feedstock properties such as viscosity profile, density, specific heat, and thermal conductivity as well as the process parameters such as melt temperature, mold temperature, and volumetric flow rate were implemented into the simulation tool. Three matrix models were used to introduce the evolution of the viscosity according to the shear rate and

temperature, specific heat capacity according to the temperature, and thermal conductivity according to the temperature.

The four 3D CAD models illustrated in Figure 3.5 were produced by SOLIDWORKS and then imported in Moldflow to be meshed using a tetrahedral structure imposed by the PIM module. These different geometries were used to demonstrate the ability of the Moldflow package to predict the in-cavity pressure during the injection stage of LPIM metallic feedstock for more complex 2D mold cavities. In this respect, different mesh sizes varying from 0.3 to 3 mm were tested to define the optimal mesh size minimizing the computational time as well as the error in injection pressure (i.e., change in pressure values). This convergence study was used to define an optimal mesh size of about 0.5 mm producing no impact on the pressure results, while minimizing the computational time. Since the mold cavities presented in Figure 3.5 have similar total volumes, this optimal mesh size was used for all numerical simulations (i.e., about 1.5 to 2.6 million 3D tetrahedral elements according to the mold cavity).
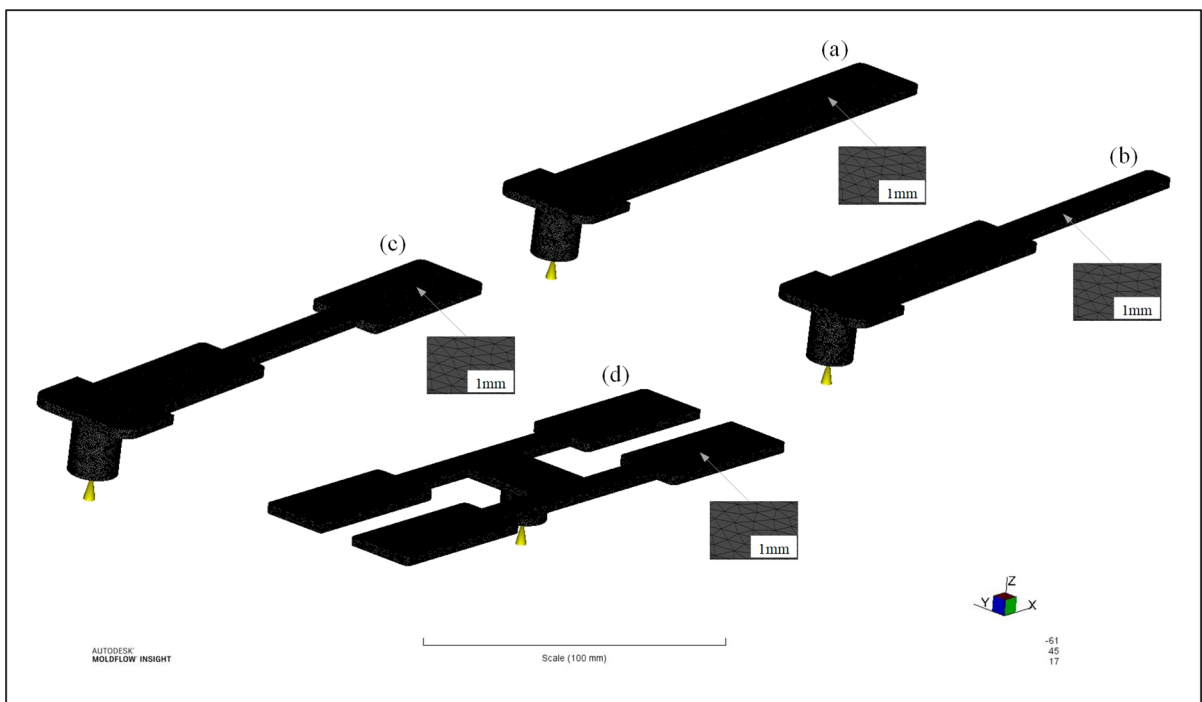


Figure 3.5 3D view of the meshed parts using finite element method (FEM)

The boundary conditions such as mold temperature, the time step, the limit of iterations, and the characteristics of the injection molding machine such as its maximum injection pressure and the type of injection control (piston speed or volumetric flow rate) were defined using the values reported in Table 3.2. Activation of the gravity effect and inertia was applied to take into account the external force experienced by the feedstock. The solver then uses Computational Fluid Dynamics (CFD) principles based on solving equations of conservation

of momentum, mass, and energy (i.e., the equations $\frac{\partial \rho}{\partial t} + \nabla \cdot (\rho \boldsymbol{u}) = 0$

(1.10) to $\beta = -\frac{1}{\rho}\frac{\partial \rho}{\partial T}$ (1.14) presented above) to simulate

mold filling behavior of the feedstock in a mold cavity.

Table 3.2  The boundary conditions

| Mold temperature (°C) | 30, 40, and 50 |
|---|---|
| Time step | 0.01 |
| Limit of iterations | 50 |
| Maximum injection pressure (MPa) | 1 |
| Volume flow rate (cm$^3$/s) [piston speed (mm/s)] | 10 [~50] |

### 3.3.2    Experimental validation

Experimental tests were performed to validate the flow patterns and pressure values predicted by numerical simulations. In continuity of  the methodology developed by Azzouni et al. (Azzouni et al., 2021), 2D mold cavities were  slightly complexified (Figure 3.7) to force different filling behavior and confirm the capability of this simulation package to predict these in-cavity pressure during the filling stage of LPIM metallic feedstock. The injected length simulated by Moldflow at different filling stages was compared with the results obtained by

real-scale injections that were performed using the low-pressure injection press available at ÉTS (Figure 3.6a) using a typical sequence illustrated in Figure 3.6b-g. Following an initial vacuum of about 45 minutes, the injection device takes out the desired volume of feedstock from the container aligned with the piston (Figure 3.6b). The injection cylinder is then aligned with the mold (Figure 3.6c), clamped on the injection table and the molten feedstock is pushed into the mold cavity (Figure 3.6d). Once the feedstock is solidified, the mold is removed from the injection table and the part is ejected from the mold. After the injection, the feedstock remaining in the cylinder (Figure 3.6e) is returned into the container in the steps illustrated in Figure 3.6f-g (Lamarre, 2016). The real-scale injections were performed using the same parameters used for numerical simulation (Table 3.2).
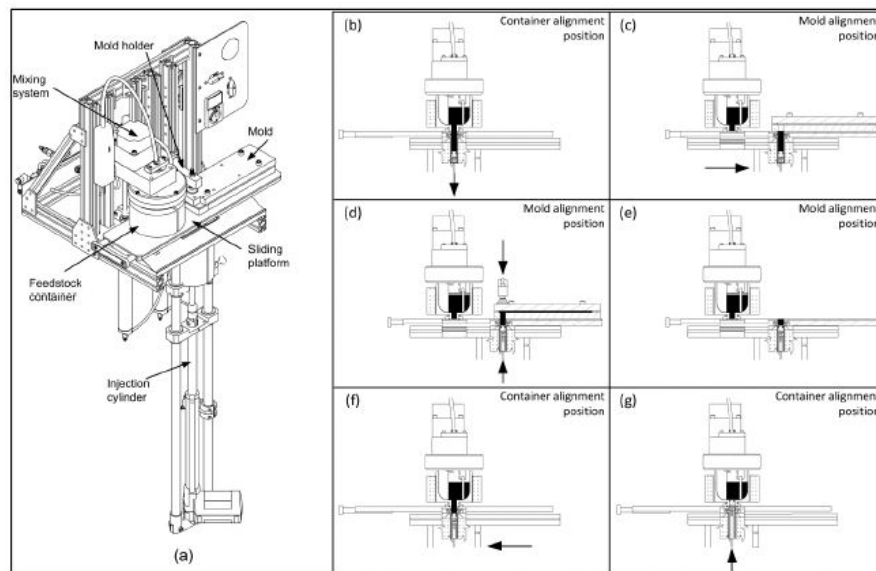


Figure 3.6 (a) General view of the injection system in a mold
Alignment position, and (b-g) partial section views of the injection
system describing the method for injecting a feedstock
Taken from Lamarre (2016, p. 52)

The 2D mold cavities presented in Figure 3.7 were equipped with a piezoresistive pressure sensor (series 25Y, Omni instruments: maximum pressure of 50 kPa and accuracy +/- 0.25 kPa) placed on the top of the gate. To measure the in-cavity pressure, the voltage returned by

the sensor was converted in a pressure signal using the equation $(P = \left(\frac{P_{max}}{V_e}\right)(\frac{V_m}{C_f})$ (3.2) that was implemented in an acquisition card (National Instruments) managed by a LabVIEW program.

$$P = \left(\frac{P_{max}}{V_e}\right)(\frac{V_m}{C_f}) \tag{3.2}$$

where $P$ is the experimental pressure, $P_{max}$ is the full-scale capacity (the maximum pressure of 50 kPa in this case), $V_e$ is the excitation voltage, $V_m$ is the measured voltage (between 0 and 8 Volts), and $C_f$ is the calibration factor equal to 0.25. For an excitation voltage of 32 volts, the equation $(P = \left(\frac{P_{max}}{V_e}\right)(\frac{V_m}{C_f})$ (3.2) can be written as the following equation $(P = 6.25 \cdot V_m$ (3.3):

$$P = 6.25 \cdot V_m \tag{3.3}$$

Although this pressure sensor was delivered with a calibration certificate, it was validated using an Omega digital pressure gauge coupled with the custom adaptor shown in Figure 3.8a. The pressure was applied manually using the manual pump on the digital pressure gauge and maintained for about 30 seconds for each step. A total of eight steps were done to cover the whole range of the piezoresistive sensor (from 0 to 5 bars). The comparison results presented in Figure 3.8b confirm that the piezoresistive sensor provides accurate pressure values within ±0.5 kPa which is far below typical pressure variation expected in this project. These tests also confirmed that the maximum pressure variation during an applied static pressure of 30 seconds was ±0.2 kPa.
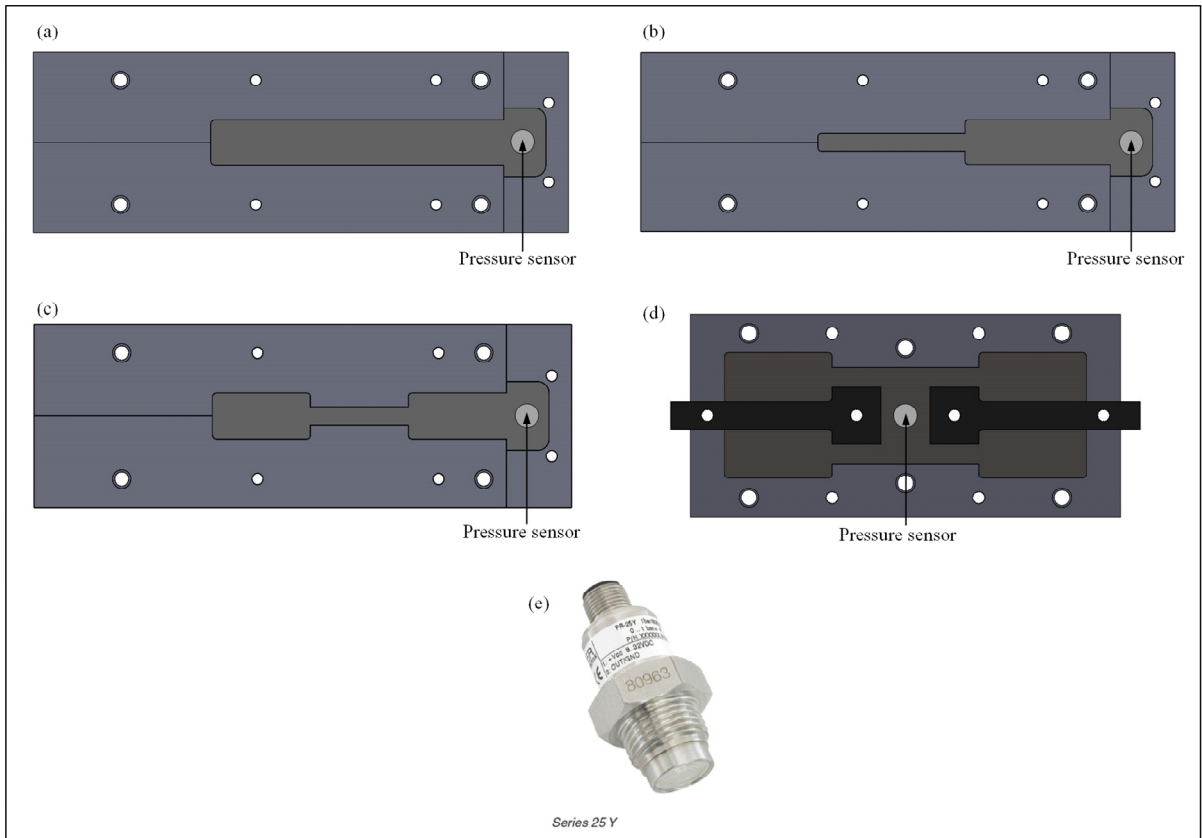
Figure 3.7 (a-d) Top view of the mold cavity with pressure sensor positions, and (e) image of the piezoresistive pressure sensor (series 25Y)
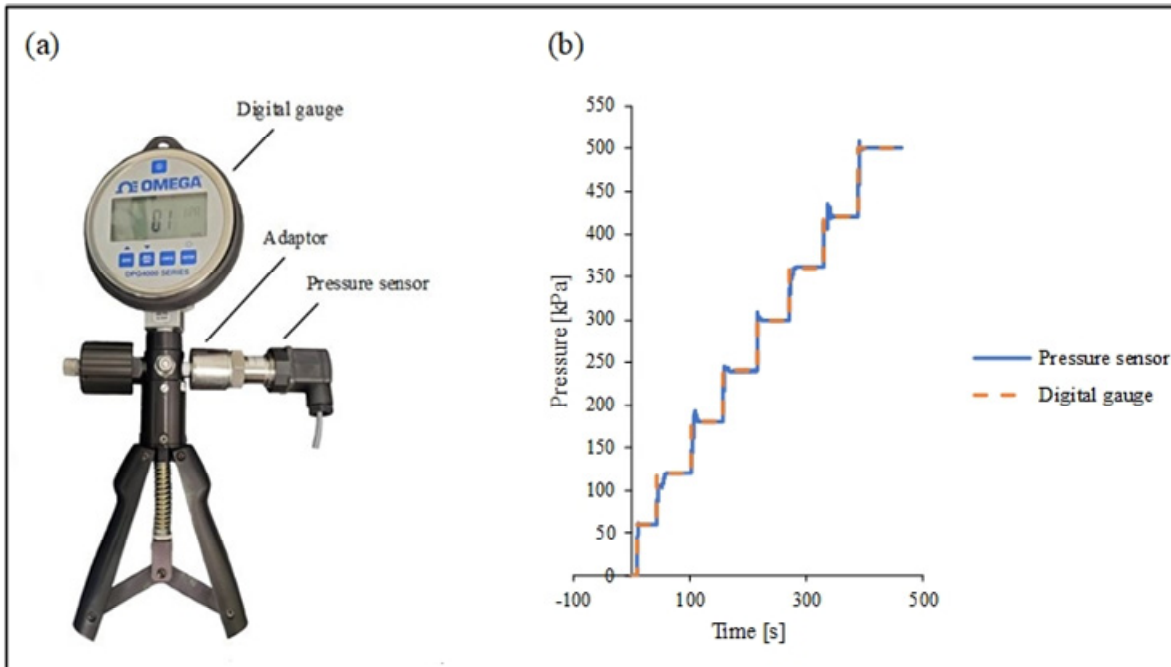
Figure 3.8 (a) the piezoresistive sensor coupled with the Omega digital gauge (b) Pressure curve of the 5-bar sensor compared to different pressure applied by the calibration tool

# CHAPTER 4

# Mold filling behavior of LPIM feedstocks using numerical simulations and real-scale injections

Foad Haghniaz [a], Dorian Delbergue [a], Raphaël Côté [a], Vincent Demers [a]

[a] Department of Mechanical Engineering, École de Technologie Supérieure,
1100 Notre-Dame West, Montreal, Quebec, Canada H3C 1K3

## 4.1      Abstract

The low-pressure powder injection molding (LPIM) process is known to use molds and injection machines that are smaller in size overall, and which may ultimately provide cost reductions as compared to the conventional PIM process. However, further studies are needed to improve and transition the technology to the point where it is ready for metallic-based feedstocks. This study aims to compare the flow patterns and in-cavity pressures obtained experimentally and numerically for different conditions. Four feedstocks based on 17-4PH stainless steel powder were fully characterized and implemented as material laws in an Autodesk Moldflow package before to obtain numerical simulations that were then validated using real-scale injections. The flow patterns obtained numerically for the different flat bar mold geometries were in good agreement with the experimental flow patterns, showing an almost perfect fit, whereas for the flow patterns of the complex mold geometry, there were some minor discrepancies. The simulated pressure profiles obtained for different mold geometries, feedstock temperatures, mold temperatures and solid loadings were in good agreement with the experimental pressure profiles in terms of trend and pressure values, with maximum relative differences varying from 30 to 64% depending on particular feedstocks and process parameters.

**Key words:** Low-pressure powder injection molding, numerical simulation, metallic powder, feedstock, mold filling

## 4.2 Introduction

Powder injection molding (PIM) is a manufacturing process used to produce metallic or ceramic components exhibiting complex geometries and precise dimensions at a relatively low cost (Gonzalez-Gutierrez et al., 2012). PIM involves four basic steps, during which the powder is firstly (i) mixed with a molten polymeric binder to form a homogenous feedstock that is then (ii) injected into a mold cavity before being (iii) debound to completely remove the binder, and finally (iv) sintered to obtain a final dense component (Heaney, 2012; Kryachek, 2004). High-pressure powder injection molding (HPIM) and low-pressure powder injection molding (LPIM) are the two declinations of the PIM technology. In HPIM, high-viscosity feedstocks (>100 Pa·s) formulated from high-viscosity wax/polymer-based binders are injected into a mold cavity using a high pressure typically varying from 20 to 200 MPa (German & Bose, 1997). In LPIM, low-viscosity feedstocks (< 100 Pa·s) formulated from low-viscosity wax-based binders are injected at pressures that are generally lower than 1 MPa (Peltsman, 1986; Rei et al., 2002). The low pressure required in the LPIM process means the size of the injection machines can be smaller, just like the overall mold dimensions. The result is increased design flexibility and a decrease in fabrication costs (Medvedovski & Peltsman, 2012). However, the technology readiness level of the LPIM process remains relatively low, especially for metallic-based feedstocks, whose molding behaviors were mainly studied for high-viscosity HPIM mixtures, using experimental and numerical approaches. In this context, the mold filling behavior was successfully simulated to optimize the process conditions and minimize or avoid the formation of defects such as voids, sinks, jetting, welding lines, warpage, and cracks (Thornagel, 2010). To perform PIM simulations, feedstock properties, including physical, thermal, and rheological properties have traditionally been experimentally measured and then implemented as material laws in simulation packages such as Moldflow, Sigmasoft, PIMsolver, and Modlex3D in order to investigate the melt front velocity, filling time, segregation, and pressure during an injection (Semenov et al., 2019; Tosello et al., 2019).

Tseng et al. (Tseng et al., 2014) used Moldex3D to predict black lines caused by powder-binder phase separation occurring during the injection stage. The suspension balance model provided in the software was able to numerically predict this defect in the vicinity of the gate observed experimentally. Using the same simulation package combined with an experimental validation, Bandiwadekar (Bandiwadekar, 2017) predicted the mold filling behavior of a high-viscosity lead-zirconate-titanate feedstock that was used to reduce the development time required for the fabrication of piezoelectric sensors. Atre et al. (Atre et al., 2007) used PIMSolver to study the effect of several input parameters on pressure, temperature, and flow responses (i.e., output parameters) during the mold filling of a stainless steel feedstock. A sensitivity analysis confirmed that the output parameters related to the flow were affected by the process parameters and geometry conditions, while the output parameters related to pressure and temperature were sensitive to the same input parameters, in addition to the feedstock properties. Using the same metallic-based feedstock and the same simulation package, Ahn et al. (Ahn et al., 2008) confirmed one year later that the filling, packing, and cooling stages could be accurately simulated when rheological characteristics such as the yield stress and apparent slip phenomena were taken into account by the model. Similarly, Liu et al. (Liu et al., 2018) implemented the wall-slip effect in an ANSYS package to increase the accuracy of the pressure gradient numerically predicted for a high-viscosity ceramic-based feedstock. Similarly, Sanetrnik et al. (Sanetrnik et al., 2021) recently confirmed with an HPIM metallic-based feedstock that the wall-slip effect appears to increase as the particle size and sphericity increase. Mulser et al. (Mulser et al., 2011) experimentally validated the numerical simulation results obtained with SIGMASOFT during a co-injection of two different stainless steel high-viscosity feedstocks before concluding that the feedstock temperature and packing pressure drive the formation of the contact interface between the two materials. In two different studies, Lenz et al. (Lenz et al., 2012; Lenz et al., 2014) used Moldflow to identify the critical parameters affecting a ceramic-based HPIM feedstock during the injection stage. They demonstrated that the feedstock melting point is the most important parameter affecting the injection pressure, the clamping force, the shear stress, the sink mark depth, the flow front temperature, and the volumetric shrinkage.

Although numerical tools are routinely used to predict the behavior of HPIM powder-binder mixtures, only a few studies have considered the simulation of the LPIM injection process. To the best of the authors' knowledge, all these studies were performed using the Moldflow package, with the first simulations realized by Zhang and Lin (Zhang & Lin, 2007) to better understand the impact of injection parameters during the fabrication of a complex shape ceramic ferrule from a wax-based feedstock containing no backbone polymer. About ten years later, Sardarian et al. confirmed the powerful capacity of the same Moldflow package by simulating the mold filling (Sardarian et al., 2016a), jetting(Sardarian et al., 2016c), and pressure distribution (Sardarian et al., 2016b) for a low-viscosity alumina feedstock. These simulation results showed that the jetting length increases with an increase in injection pressure and temperature. Recently, Yavari and Khorsand (Yavari & Khorsand, 2021) used the same package to confirm that the segregation and imbalance filling phenomena occurring during the injection of an LPIM silicon-carbide feedstock were more severe for thin-wall components. Using an LPIM stainless steel feedstock, Ben Trad et al. (Ben Trad et al., 2020) predicted the injected length, the melt front velocity, and the filling times, which were validated with experimental results. In that study, the absence of segregation captured by Moldflow was also confirmed by thermogravimetric measurements. The same simulation package was used to study the injection flow and occurrence of defects for two titanium-based feedstocks injected into two different intricate mold cavities (Côté, Azzouni, & Demers, 2020; Ghanmi & Demers, 2021). The study demonstrated that the melt front location and filling completion predicted by the numerical model at different short shots were in good agreement with experimental observations. An experimental validation of very low-pressure values simulated from an LPIM feedstock was performed for the first time by Azzouni et al. (Azzouni et al., 2021) in two simple shape 2D mold cavities. However, an in situ validation of the pressure values developed within more complex shape mold cavities was never confirmed for such low-viscosity ceramic- or metallic-based feedstocks. The present study aims to demonstrate the ability of the Moldflow package to predict the in-cavity pressure during the injection stage of LPIM metallic feedstocks for more complex 2D mold cavities.

## 4.3      Methodology

### 4.3.1      Feedstock preparation

One water-atomized 17-4PH stainless steel powder (Epson Atmix Corporation, Japan) and one gas-atomized 17-PH stainless steel powder (Sandvik Osprey, United Kingdom) were mixed with a wax-based binder to formulate a total of four feedstocks using solid loadings varying from 60 to 65 vol. %. Two different suppliers were selected since it was not possible to obtain the powders with these atomization techniques from the same supplier. Gas atomized powders are produced by melting the metal using induction or other method of heating and subsequently pouring the melt through a nozzle. After leaving the nozzle, the liquid metal is struck by a high-velocity stream of gas, which breaks the melt into fine droplets, then these droplets solidify into spherical shaped particles during their fall. In most aspects, water atomization is similar to gas atomization except that water rather than gas is used to break up the melt stream into fine particles exhibiting slightly irregular shape Figure 4.1a-b (Aich et al., 2017; Heaney, 2012). The particle shape and particle size distribution of these dry powders were assessed using a scanning electron microscope (Hitachi 3600, secondary electrons detector) and a laser diffraction particle analyzer (LS 13320 Beckman Coulter), respectively. As reported in Figure 4.1c, water atomization exhibits a blend of spherical and ligamental particles with an average particle size of about 11 μm, while gas atomization produces spherical shapes with a similar average particle size of 12 μm Figure 4.1d (measured by laser diffraction particle analyzer). The powder characteristics with similar particle size distribution extracted from Figure 4.1e-f are reported in Table 4.1.
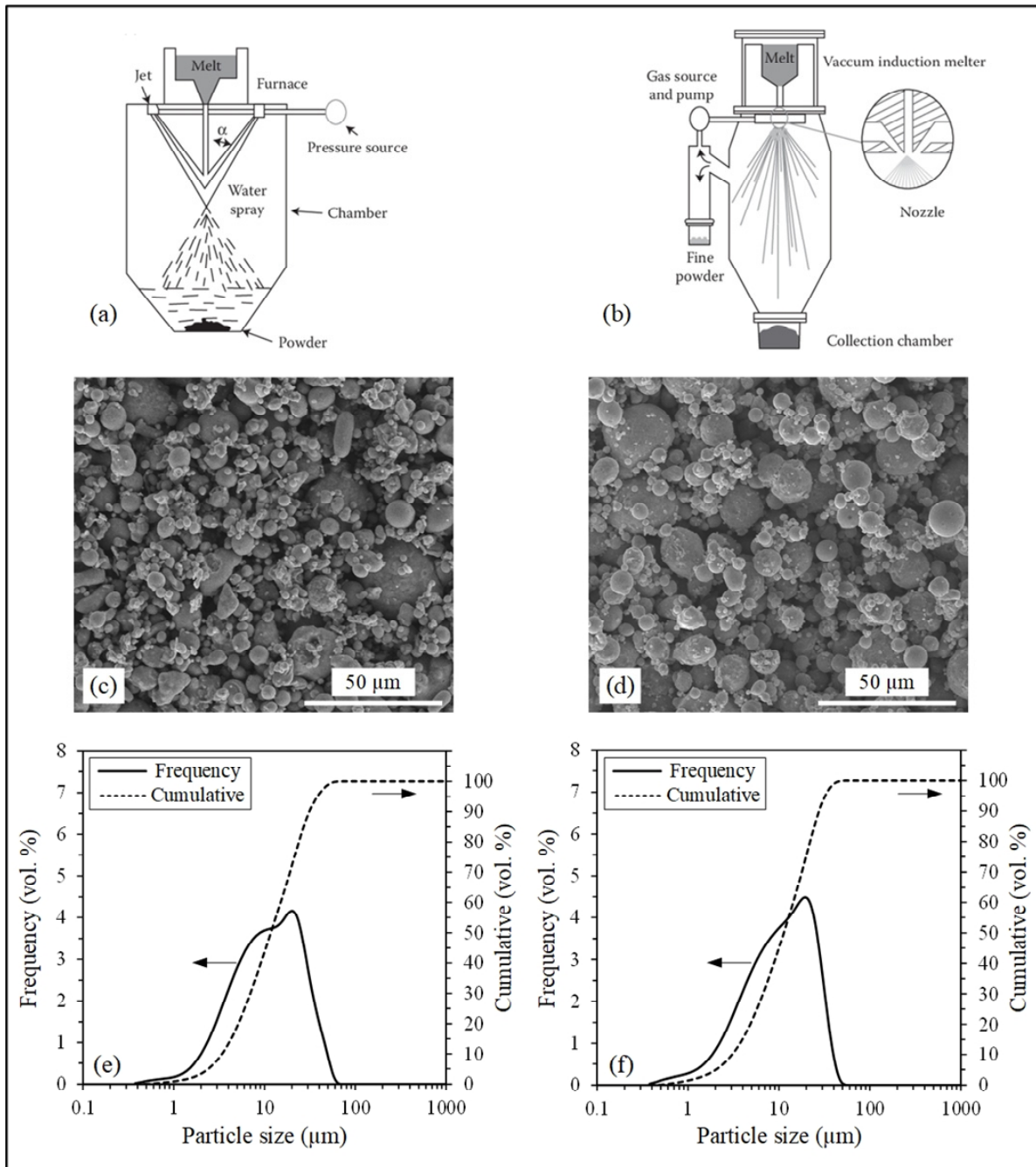
Figure 4.1 Schematics of atomization techniques (a) water atomization, and (b) gas atomization
Taken from Aich et al. (2017, p. 467)
SEM observations and particle size distributions of 17-4PH dry powders produced by (c) & (e) water atomization, and (d) & (f) gas atomization

Table 4.1 17-4 PH powder characteristics

| Powder lot | Atomization technique | Density (g/cm$^{-3}$) | $d_{10}$ (µm) | $d_{50}$ (µm) | $d_{90}$ (µm) | Supplier |
|---|---|---|---|---|---|---|
| PF-20F | Water | 7.8 | 3.4 | 11.8 | 31.3 | Epson Atmix |
| S17700 | Gas | 7.8 | 3.0 | 11.3 | 27.5 | Sandvik Osprey |

The two powders were mixed with the same wax-based binder system formulated from paraffin wax (PW), Carnauba wax (CW), stearic acid (SA), and ethylene vinyl acetate (EVA) according to the proportion reported in Table 4.2 . These binder constituents were selected due to their extensive use in LPIM. The paraffin wax and Carnauba wax were used to help with the mold filling and part ejection; the stearic acid was used to promote the surfactant effect, while the ethylene-vinyl acetate was added to act as a thickening agent needed to control the phase segregation. Feedstock formulations presented herein are referenced by their atomization techniques (i.e., "W" for water or "G" for gas) and nominal solid loading calculated at room temperature (i.e., 60 or 65 vol. %). For example, the feedstock G60 is a mixture containing 60 vol. % of gas-atomized powder. The melting point of each binder constituent and feedstock was obtained using a Discovery DSC 2500 (TA instruments) according to the standard test method ASTM D3418-15 (ASTM-D3418-15, 2015). The tests were conducted over temperatures ranging from 20 to 120°C, using a heating rate of 10°C/min under a nitrogen gas flow rate of 50 ml/min. The density of the metallic powder, binder, and feedstock was measured using a helium gas pycnometer (AccuPyc II 1340) according to the ASTM B923-16 standard (ASTM-B923-16, 2016). The characteristics of the feedstock constituents are given in Table 4.3.

Table 4.2 Volume fraction of the powder and polymers used for feedstock formulations

| Feedstock # | Atomization technique | Vol. % | | | | |
| --- | --- | --- | --- | --- | --- | --- |
| | | Powder | Paraffin wax (PW) | Carnauba wax (CW) | Stearic acid (SA) | Ethylene-vinyl acetate (EVA) |
| G60 | Gas | 60 | 30 | 7 | 2 | 1 |
| G65 | Gas | 65 | 25 | 7 | 2 | 1 |
| W60 | Water | 60 | 30 | 7 | 2 | 1 |
| W65 | Water | 65 | 25 | 7 | 2 | 1 |

Table 4.3 Melting point and density of feedstock constituents

| Constituents | Melting point (°C) | Density (g/cm$^3$) | Supplier (Product number) |
| --- | --- | --- | --- |
| Paraffin wax (PW) | 59 | 0.9 | Sigma-Aldrich (327204) |
| Carnauba wax (CW) | 85 | 1.0 | Sigma-Aldrich (243113) |
| Stearic acid (SA) | 75 | 0.9 | Sigma-Aldrich (W303518) |
| Ethylene-vinyl acetate (EVA) | 49 | 1.0 | DuPont (Elvax$^{TM}$ 250) |

### 4.3.2    Feedstock characterization

The feedstock properties required for the numerical simulations were the density, the melt viscosity, the specific heat capacity, and the thermal conductivity. The critical solid loadings (CSL) for the water-atomized powder lot were assessed from the pycnometer density profiles reported in Figure 4.2a. A CSL of about 66 vol. % was determined according to the criterion where the measured density diverged by 0.025 g/cm$^3$ (dashed line) from the theoretical density (continuous line). Each feedstock density was measured three times using different samples to obtain an average value and a standard deviation as low as ~0.003 g/cm$^3$ (not shown in Figure 4.2a, since the error bars are smaller than the marks). In this work, two solid loadings were set at 60 and 65 vol. %, i.e., below the critical value, to guarantee the fluidity of the feedstocks in all mold cavities, with the feedstocks G60 and W60, and to represent the typical high powder contents used in metal injection molding (MIM), with the feedstocks G65 and W65. The DSC thermograms presented in Figure 4.2b were used to determine the feedstock transition temperature obtained from the cooling stage. The feedstocks' specific heat ($C_p$) according to the temperature presented in Figure 4.2c was obtained using three experimental DSC thermograms obtained with the feedstocks, a standard material (i.e., sapphire), and an empty pan, according to the ASTM-E1269 standard test method (TA Instruments, 2021). The feedstocks' thermal conductivity ($k$) reported in Figure 4.2c was measured according to the transient line-source technique described in the ASTM-D5930 standard test method (ASTM-D5930-17, 2017).
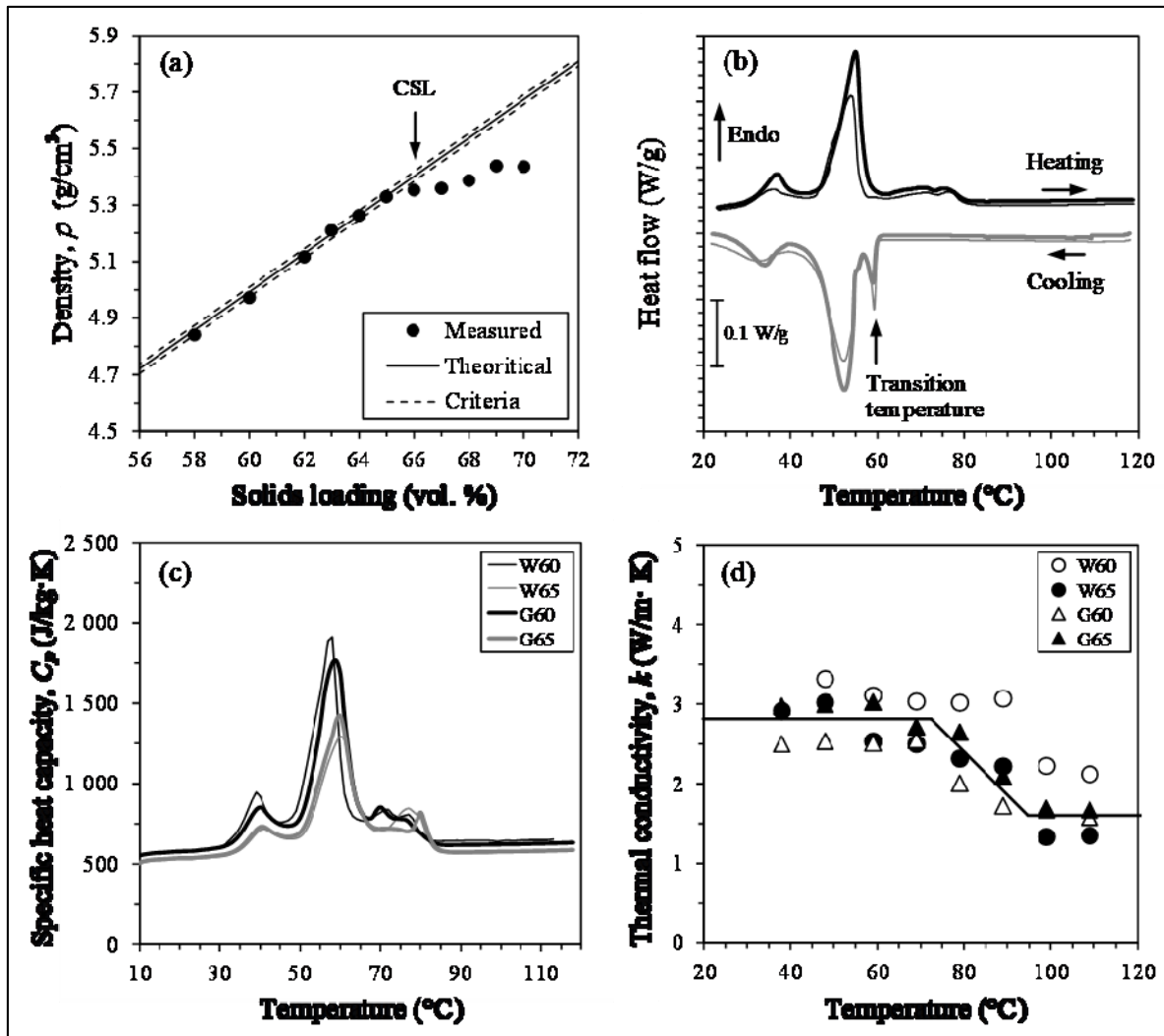
Figure 4.2 Physical and thermal properties of feedstocks: (a) feedstock density according to solid loading, (b) DSC thermograms used to determine the transition temperature, (c) specific heat capacity, and (d) thermal conductivity of the feedstock measured at different temperatures (W60 & W65: feedstock containing 60 or 65 vol. % of water-atomized powder; and G60 & G65: feedstock containing 60 or 65 vol. % of gas-atomized powder)

The feedstock viscosity profiles reported in Figure 4.3 were measured with a rotational rheometer (Anton Paar MCR 302), using a cup/cylinder configuration (CC-17) placed into a temperature-controlled measuring system (C-PTD 200). Molten feedstock was poured into the rheometer cup and then tested at shear deformation rates ranging from 0.5 to 3,500 s$^{-1}$ under constant temperature conditions varying from 80 to 100°C. The viscosity profiles were obtained by repeating each condition three times to calculate the average viscosity profiles

following the procedure described in (Fareh et al., 2017). The experimental viscosity profiles were fitted using the Cross-WLF viscosity model, a second-order mathematical fitting, and a matrix interpolation approach. A superposition of these three models on experimental data was shown only for the W60 feedstock for visual clarity Figure 4.3a. The Cross-WLF viscosity model is generally used when the viscosity remains constant at low shear rates, while exhibiting a significant decrease at high shear rates, while for its part, the second-order fitting is generally used when the feedstock viscosity decreases meaningfully at low shear rates and stabilizes as a Newtonian-like plateau at high shear rates. In Moldflow, the matrix interpolation approach is used when the last two models are not able to adequately fit the experimental data. The Cross-WLF and the second-order viscosity models are defined respectively as equation (

$$\eta = \frac{C\exp\left(-\dfrac{A\cdot(T_k-D)}{B+(T_k-D)}\right)}{1+\left(\dfrac{\left(C\exp\left(-\dfrac{A\cdot(T_k-D)}{B+(T_k-D)}\right)\right)\dot{\gamma}}{\tau^*}\right)^{1-n}}$$

(4.1) and equation (

$$\ln(\eta) = E + F\ln(\dot{\gamma}) + GT_c + H\left[\ln(\dot{\gamma})\right]^2 + I\ln(\dot{\gamma})T_c + JT_c^2$$

(4.2):

$$\eta = \frac{C\exp\left(-\dfrac{A\cdot(T_k-D)}{B+(T_k-D)}\right)}{1+\left(\dfrac{\left(C\exp\left(-\dfrac{A\cdot(T_k-D)}{B+(T_k-D)}\right)\right)\dot{\gamma}}{\tau^*}\right)^{1-n}}$$

(4.1)

$$\ln(\eta) = E + F\ln(\dot{\gamma}) + GT_c + H\left[\ln(\dot{\gamma})\right]^2 + I\ln(\dot{\gamma})T_c + JT_c^2$$

(4.2)

where $\eta$ is the melt viscosity in Pa·s, $\dot{\gamma}$ is the shear rate in s$^{-1}$, $T_k$ is the temperature in kelvin, $T_c$ is the temperature in degrees Celsius, and all other parameters (such as $\tau^*$, the critical stress level at the transition to shear thinning; $n$, the power law index in the high shear rate regime,

and *A to J*) are data-fitted coefficients determined by curve fitting. Both viscosity models were fitted into the experimental viscosity profiles using the Matlab Curve Fitting Toolbox and the fitting coefficients are reported in Table 4.4.
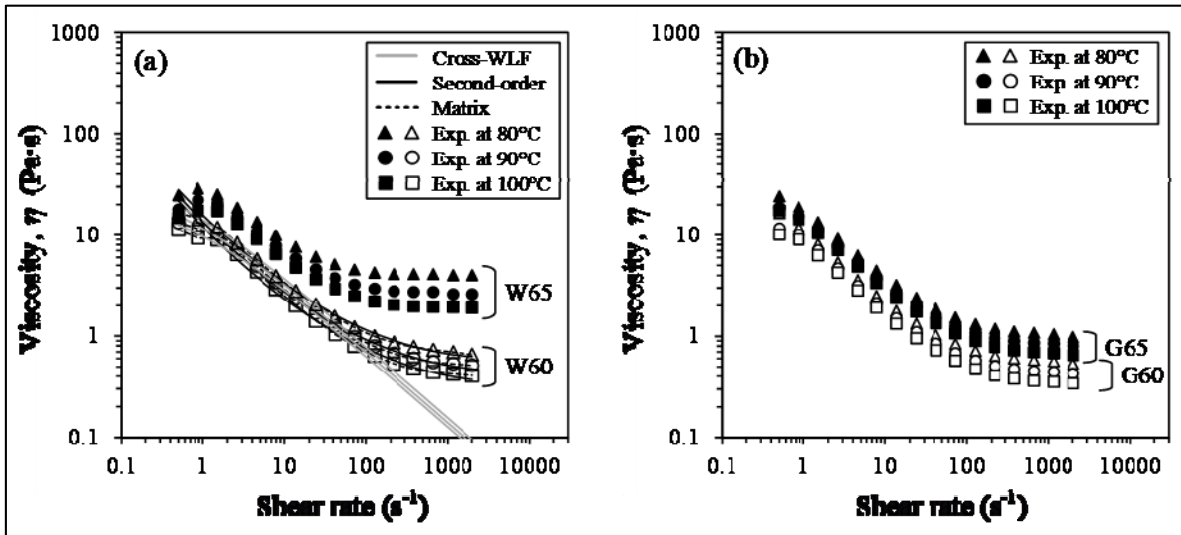


Figure 4.3 (a) Viscosity profiles with superimposed Cross-WLF, second-order, and matrix models (W60 & W65: feedstock containing 60 or 65 vol. % of water-atomized powder; and (b) G60 & G65: feedstock containing 60 or 65 vol. % of gas-atomized powder)

Table 4.4 Data-fitted coefficients used in Cross-WLF and second-order viscosity models

|  | **W60** | **W65** | **G60** | **G65** |
|---|---|---|---|---|
| $n$ | 0.2956 | 0.5418 | 0.3118 | 0.6365 |
| $\tau^* (Pa)$ | 14.180 | 2.769 | 7.90 | 0.035 |
| $A$ | 18.18 | 5.46 | 2.96 | 48.02 |
| $B (K)$ | 50.44 | 156.50 | 11.58 | 353.70 |
| $C (Pa \cdot s)$ | 9.928 E6 | 1.402 E2 | 2.120 E2 | 7.849 E1 |
| $D (K)$ | 248.3 | 367.0 | 344.2 | 372.9 |
| $E$ | 4.805 | 7.036 | 5.796 | 7.262 |
| $F$ | -6.557 E-1 | -3.757 E-1 | -6.164 E-1 | -6.329 E-1 |
| $G$ | -3.52 E-2 | -6.90 E-2 | -6.25 E-2 | -8.31 E-2 |
| $H$ | 4.801 E-2 | 3.292 E-2 | 4.227 E-2 | 3.878 E-2 |
| $I$ | -1.671 E-3 | -1.746 E-3 | -1.070 E-3 | -4.309 E-4 |
| $J$ | 1.198 E-4 | 2.683 E-4 | 2.531 E-4 | 3.625 E-4 |

### 4.3.3    Numerical simulation and experimental set-up

Numerical simulations of the injection stage were performed using Moldflow Synergy 2019 (Autodesk Inc.) for the five mold cavities presented in Figure 4.4a-e. The four simple rectangular parts presented in  Figure 4.4a-d (molds #1 to #4) were selected to study the flow patterns and pressure profiles at constant thickness (3 mm). Their cavity volumes ranged from 15.3 to 27 cm$^3$. The fifth mold (mold #5), illustrated in Figure 4.4e, was identified to study the flow behavior within a more complex shape part, especially around as-MIM features such as small holes and intricate internal cavities. The CAD models were meshed using the 3D tetrahedral elements illustrated in Figure 4.4a and the mesh sensitivity analysis performed on the mold #1 (Figure 4.4f) confirmed that a mesh size of about 0.5 mm provides an adequate accuracy in injection pressure, while not compromising the computational time required for

simulations. The mold cavities contain between 1.5 and 3.1 million elements, depending on the model's shape.
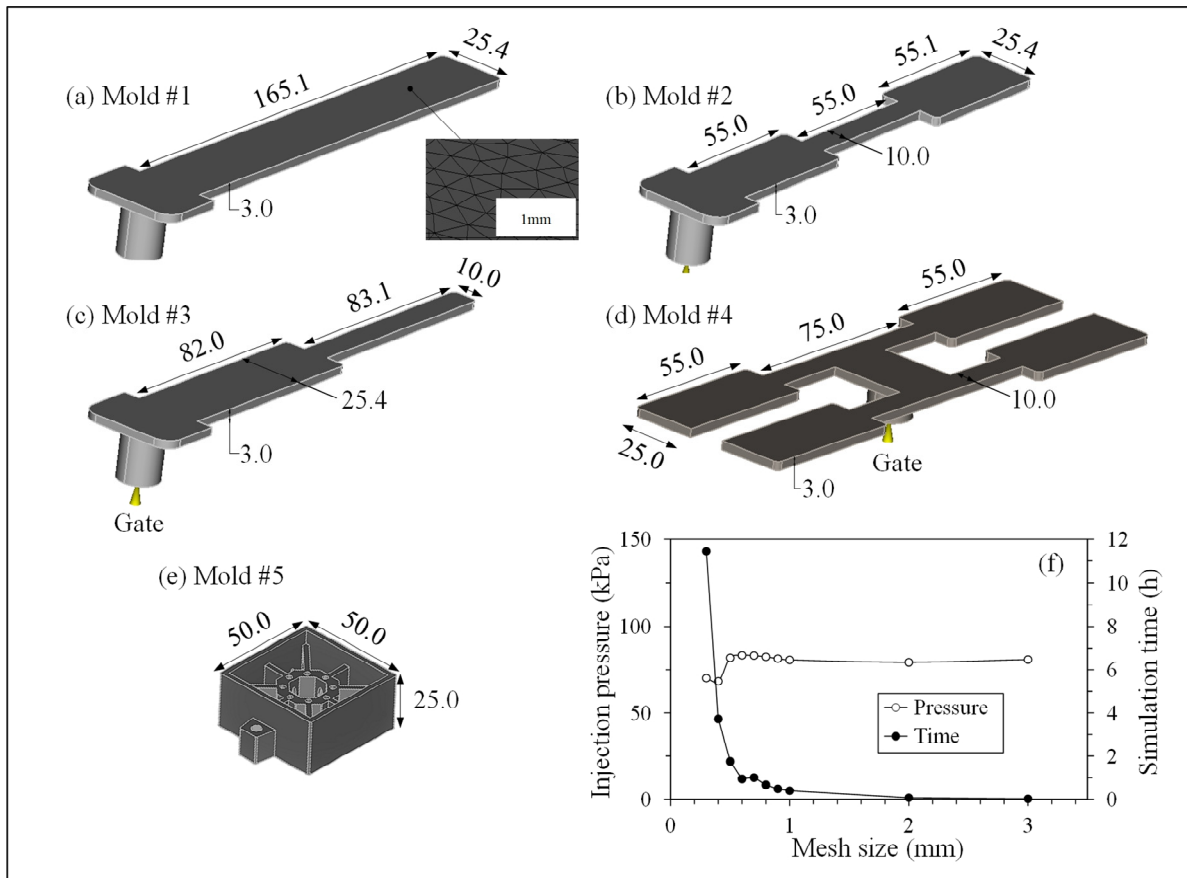


Figure 4.4 (a-e) 3D view of the five mold cavities with an example of superimposed tetrahedral finite element mesh (dimensions in mm), and (f) evolution of the pressure at the gate and simulation time according to the mesh size

In the Moldflow package, the Cross-WLF model, the second-order fitting, and the matrix linear interpolation approach are the three methods used to implement the material law related to the feedstock viscosity. As shown in Figure 4.3a, the Cross-WLF and second-order viscosity models are not well-adapted to capture both the continued decrease in viscosity at low-moderate shear rates and the quasi-Newtonian behavior seen at high shear rates for the low-viscosity feedstock used in this study. In fact, the Cross-WLF and second-order viscosity models generate respectively a maximum relative difference of 89 and 92% with the experimental data. Therefore, the experimental viscosity profiles obtained at different

temperatures were grouped, ordered, and implemented in Moldflow as the matrix viscosity model. Using this third rheological model, the viscosity was determined and managed by the simulation package from the measured data obtained at specific temperatures and shear rates, as well as via interpolations between data points and extrapolation outside the data point range. The feedstock density ($\rho$) and its thermal properties (i.e., $C_p$ and $k$ presented in Figure 4.2c-d) were implemented in Moldflow as a scalar and two material law matrices, respectively. Finally, two other important thermal parameters, namely, the transition temperature and mold-melt heat transfer coefficient, were assessed and implemented in Moldflow. For semi-crystalline or amorphous binders, the transition temperature corresponds respectively to the crystallization peak or the inflection point of the DSC heat flow curve, both obtained during the second cooling stage. Since no glass transition was observed on DSC thermograms obtained in this project, the transition temperature was set to 62°C, i.e., the first crystallization peak representing the temperature at which the melt-to-solid transition occurs (Lucyshyn et al., 2012). Based on a value proposed by Ilinca et al. (Ilinca et al., 2004), and to better reflect the heat transfer occurring between the mold interface and such feedstocks, the mold-melt heat transfer coefficient (HTC) for the filling phase was set to 100,000 W/m$^2$·°C as MIM feedstocks exhibit much higher thermal conductivities as compared to polymers using a default value of about 5000 W/m$^2$·°C (Lucyshyn et al., 2021; Zink & Kovács, 2022). The numerically obtained flow pattern and pressure were validated with real-scale injections performed with the laboratory injection press described in (Lamarre et al., 2017) and equipped with the instrumented molds illustrated in Figure 4.5a-d. The molten feedstock was injected into the steel mold cavities to produce different short shot conditions (flow patterns) and complete injections (injection pressure measurements), using the process parameters provided in Table 4.5. A speed ramp of about 300 mm/s$^2$ was used in the experiments to accelerate the feedstocks during the injections, and was reproduced in the numerical simulations. The 2D mold cavities were equipped with a Series PR-25Y piezo-resistive pressure sensor designed by Keller AG Druckmesstechnik (with a maximum pressure of 1000 kPa +/- 2.5 kPa). The pressure sensor was plugged into an NI USB-6212 acquisition card (National Instrument Corp.) and pressure measurements were recorded using a LabVIEW script.
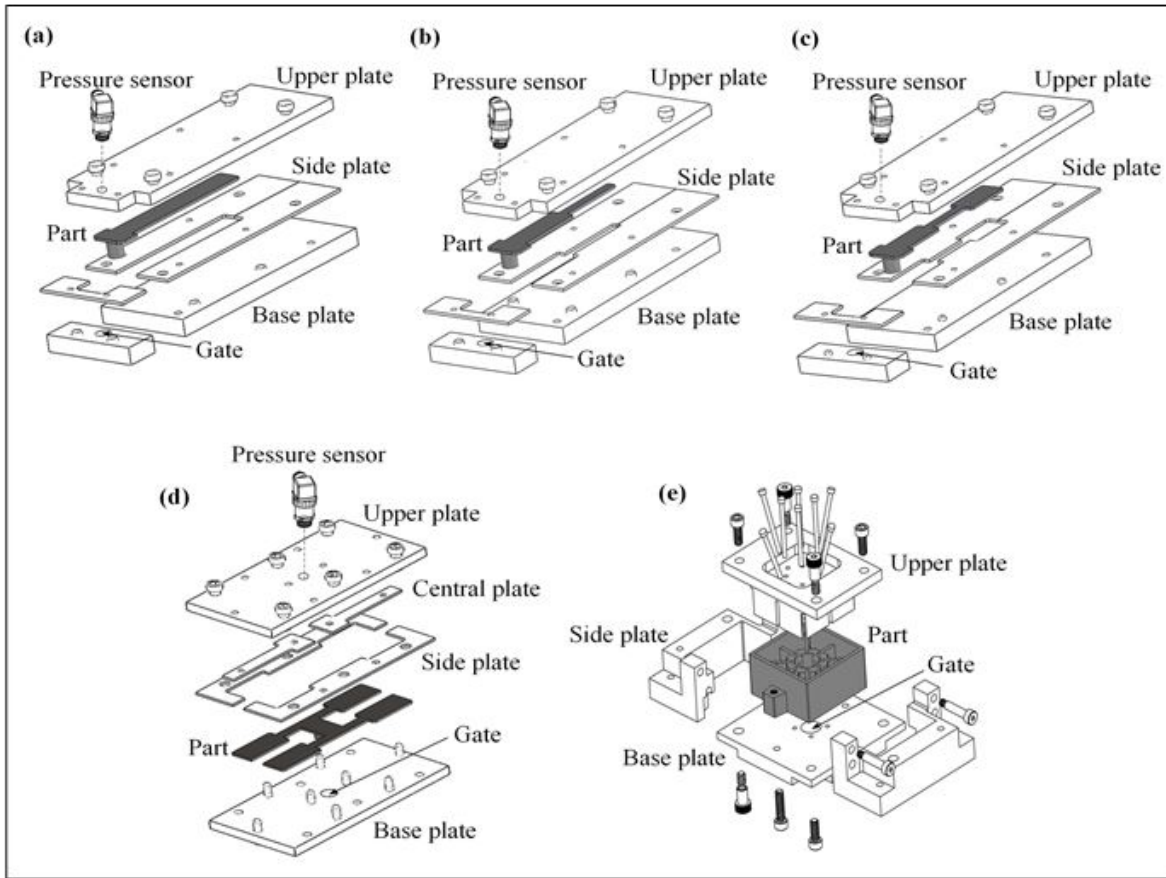
Figure 4.5 Exploded view of the mold (a) #1: constant flat bar, (b) #2: flat bar with fillet (c) #3: flat dogbone bar, (d) #4: multiple flat bars cavities (showing the location of the pressure sensor), and (e) #5: complex shape

Table 4.5 Process parameters used for the numerical simulations and real-scale injections

| Mold temperature (°C) | 30, 40, and 50 |
|---|---|
| Feedstock temperature (°C) | 80, 90, and 100 |
| Volumetric flow rate (cm$^3$/s) | 9.74 |
| [piston speed (mm/s)] | [50] |
| Speed ramp (mm/s$^2$) | ~300 |

## 4.4 Results and discussion

### 4.4.1 Influence of mold geometry on flow patterns and pressure

A qualitative and quantitative comparison between the experimental and simulated flow patterns and injection pressures is presented in Figure 4.6 for the four rectangular mold cavities (molds #1 to #4). The influence of mold geometry on these two output parameters was assessed for the feedstock W60 using a constant feedstock temperature (90°C), mold temperature (40°C), and flow rate (9.74 cm$^3$/s). During injections at constant volumetric flow rates, the position of the flow fronts measured at different short shots (Figure 4.6a-d) was controlled by the shape of the mold cavities (i.e., a given volume filled after a certain injection time). With a constant volumetric flow rate, the injection time needed to completely fill the rectangular molds ranged from 1.6 to 2.8 s. Short shots corresponding to 30, 60, and 90% mold filling stages were experimentally produced for the four different mold cavities. As presented in Figure 4.6a-d, the obtained short shots are in good agreement with the injected lengths and flow patterns predicted numerically via Moldflow for these three specific mold filling stages. Furthermore, the absence of visual defects at the surface of the short shot injections confirms that the volumetric flow rate used in this work is suitable for use in all mold geometries to avoid early solidification or jetting phenomena in feedstocks, which may occur at volumetric flow rates that are too low or too high, respectively. The progressive color gradient obtained by numerical simulations (Figure 4.6a-d) also predicted a uniform filling exhibiting no solidification or jetting occurring during the injections. The experimental pressures developed in the four different mold cavities were measured using a pressure sensor located at the top of the injection gates, as illustrated in Figure 4.5a-d. Following short shot injections, the pressure sensor mounted flush with the mold surfaces left a circular imprint on the bottom and in the middle of the green parts for molds #1-3 (Figure 4.6a-c) and mold #4 (Figure 4.6d), respectively. The experimental and simulated pressure profiles for a complete filling of the four molds are presented in Figure 4.6e-h where the pressure profiles are divided into two zones.

For all mold cavities, the gate filling zone corresponds to the vertical cylinder (visible in Figure 4.5) and the larger rectangular section in-plane with the rectangular cavities (visible in Figure 4.6a-d). The pressure recorded by the sensor in this zone remains at zero since the feedstock is not in contact with the sensor located at the top of this gate filling zone (Figure 4.6e-h). The mold filling zone corresponds to the main rectangular cavities, as presented in Figure 4.6a-d. As the molds' sections are reduced as compared to the gate filling zone, the feedstock confined within the gate filling zone comes in contact with the pressure sensor to record a continuous increase in injection pressure during the filling stage of a constant mold cavity (Figure 4.6e) to overcome the internal friction experienced by the molten feedstock. The changes in cross-section of the mold cavities #2-4 correspond to the slope variations of the pressure profiles reported in Figure 4.6f-h, and are highlighted by the hollow arrows. In the mold filling zone, the pressure drop at the end of the filling stages corresponds to the piston deceleration implemented experimentally to avoid overpressure on the sensor. The simulated pressure profiles for molds #1-3 are in good agreement with the experimental pressure profiles in terms of trends and pressure values, with a maximum relative difference of 35, 30, and 31% for the molds #1, #2, and #3, respectively. Although the simulated pressure values of the mold #4 are not consistent with the sharp initial increment measured experimentally in the gate filling zone, the slow and constant increase in the injection pressure predicted numerically in the mold filling zone follows the similar trend as the one observed experimentally.
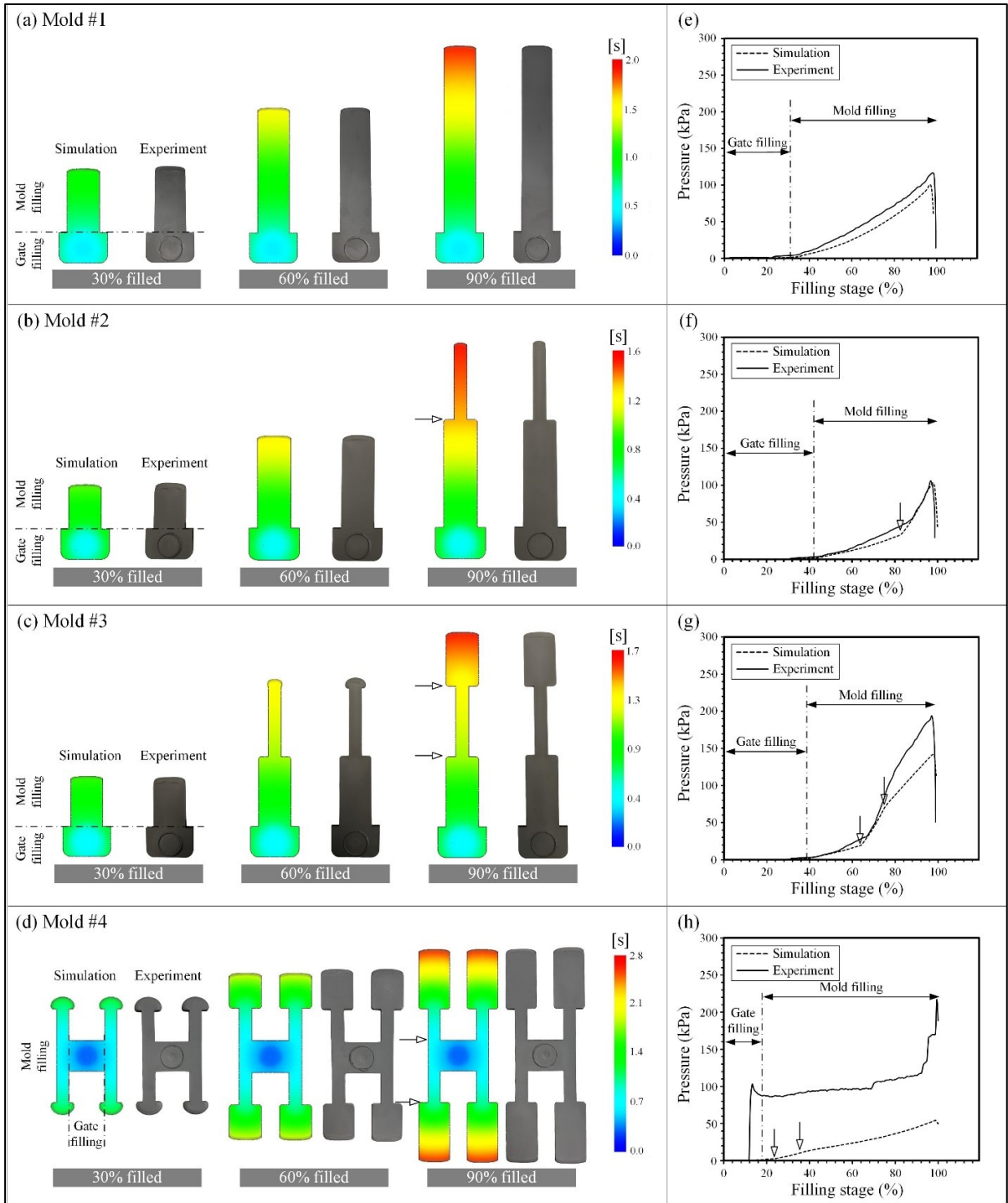
Figure 4.6 Simulated and experimental (a-d) flow patterns and (e-h) pressure profiles for the molds #1-4 (feedstock W60 injected in constant mold's thickness = 3 mm, feedstock temperature = 90°C, mold temperature = 40°C, and flow rate = 9.74 cm³/s). Hollow arrows represent changes in the molds' cross-sections

### 4.4.2 Influence of injection parameters on flow patterns and pressure

The influence of the feedstock temperature ($T_{feedstock}$) and mold temperature ($T_{mold}$) on the flow patterns and injection pressures was studied for the feedstock W60 and mold #3. The three feedstock temperatures and mold temperatures reported in Table 4.5 were used to obtain the simulated and experimental flow patterns at the 90% filling stage under various process conditions, as presented in Figure 4.7a-f. When varying $80 < T_{feedstock} < 100°C$ , $T_{mold}$ was kept constant at 40°C and, when varying $30 < T_{mold} < 50°C$ (Figure 4.7d-f), $T_{feedstock}$ was maintained at 90°C to obtain the resulting flow patterns and pressure profiles. Since all the injections were performed at a constant volumetric flow rate (9.74 cm$^3$/s), the injected lengths and flow patterns are similar, regardless of the feedstock temperatures (Figure 4.7a-c) or the mold temperatures (Figure 4.7d-f). Indeed, this injection approach (described in detail in (Lamarre et al., 2017)) controls the injection flow using a constant stroke plunger for which the feedstock properties (e.g., the viscosity typically influenced by the feedstock or mold temperatures) have no impact on its injection length for a given injection time. This result was properly captured by the numerical model, as the injected lengths and filling times are identical.

The pressure profiles experimentally recorded and numerically predicted during complete injections are presented in Figure 4.7g-h for different feedstock and mold temperatures. Similarly to the previous results obtained with the dogbone shape mold #3, the pressure profiles exhibit an S shape (i.e., changes in slope) corresponding to different part filling stages that can be divided into four (4) segments superimposed on Figure 4.7g, which are related to the top view of the injected part in Figure 4.7c. The segment #1 represents the gate filling stage (about 39% of the cavity filled), while the segments #2-4 for this constant mold thickness denote the first large cross-section, the small cross-section, and the second large cross-section representing 25, 11, and 25% of the cavity filled, respectively. As expected during injections at a constant volumetric flow rate, a change in $T_{feedstock}$ and/or $T_{mold}$ produces a variation in the injection pressure, where an increase in one or the two process parameters produces a decrease in the injection pressure, as shown in Figure 4.7g-h. This is generally explained by a decrease in feedstock viscosity with an increase in temperature (mixture as well as mold), where an

increase in feedstock temperature from 80 to 100°C produces a decrease in feesdtock viscosity of about 1 to 0.6 Pa·s (values extracted in a typical shear rate range of 100-500 $s^{-1}$ in Figure 4.3), ultimately resulting in a decrease in the injection pressure from 300 to 120 kPa for this specific mold cavity. The pressure profiles obtained experimentally (solid lines in Figure 4.6g-h) confirm that the numerical model (dashed lines in Figure 4.6g-h) was able to adequately capture the influence of $T_{feedstock}$ and $T_{mold}$ on the injection pressure, with a maximum relative difference of 39%. Using these typical injection parameters, the maximum overall injection pressure varying from 100 to 300 kPa remains significantly lower than the well-accepted value of 1 MPa reported to be used in the LPIM process. It is worth noting that this pressure is about 20 to 600 times lower than that used in the conventional high-pressure PIM process and represents an interesting opportunity to reduce the size of injection machines as well as the overall size of the molds, and finally, the cost of parts.
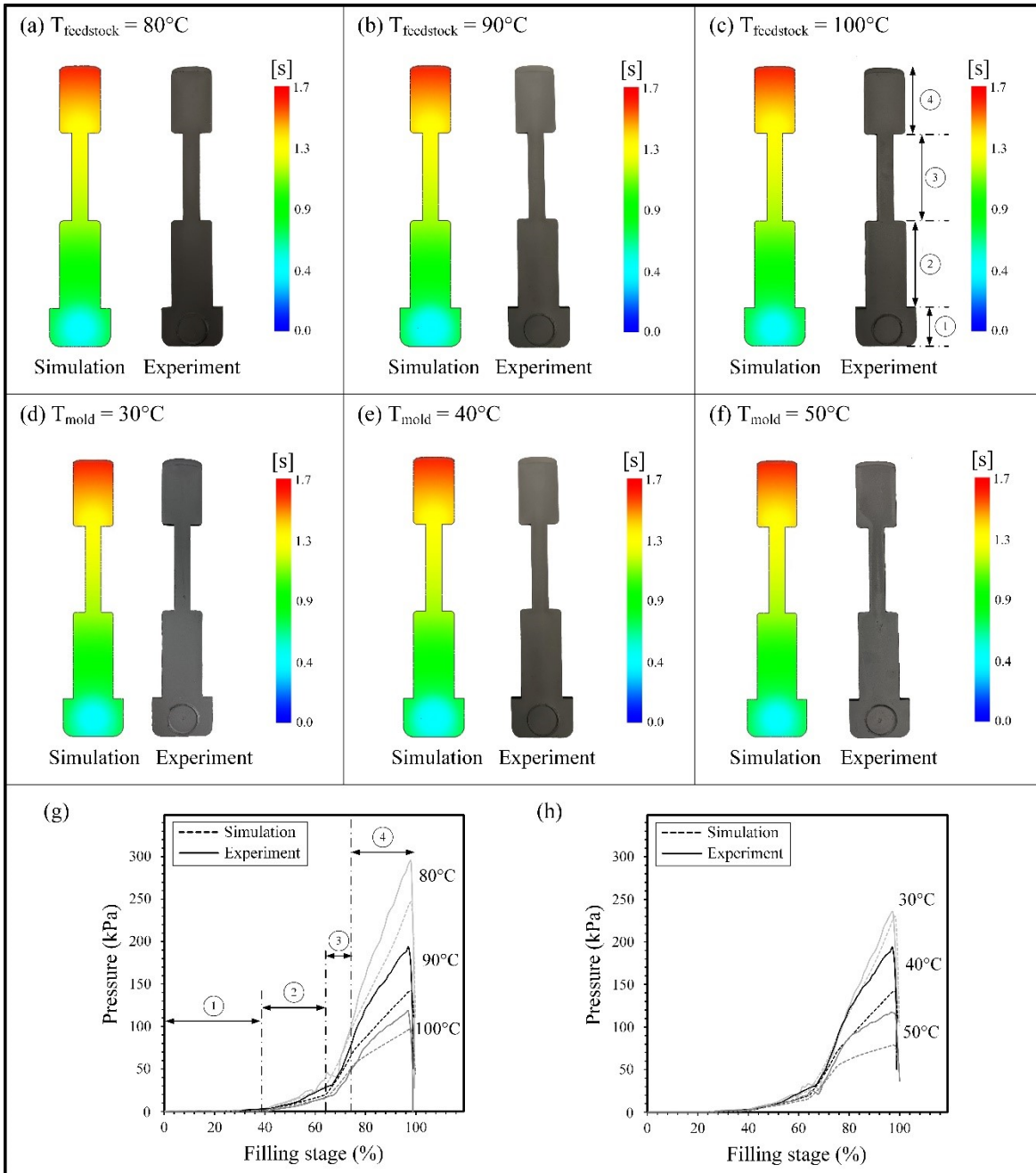
Figure 4.7 Simulated and experimental (a-f) flow patterns at 90% filling stage and (g-h) pressure profiles obtained for different feedstock temperatures 'T$_{feedstock}$' and mold temperatures 'T$_{mold}$' (feedstock W60 injected in mold #3 using constant thickness = 3 mm, and flow rate = 9.74 cm$^3$/s)

### 4.4.3 Influence of feedstock properties on flow patterns and pressure

The influence of the feedstock properties on the flow patterns and injection pressures was studied for the four feedstocks, W60, W65, G60, and G65, formulated from two different powder atomization techniques ("W" for water-atomized, and "G" for gas-atomized) and two solid loadings (60 and 65 vol. % of powder). Although the powder suppliers are different, these two powders can be compared due to similar particle size distribution. The simulated and experimental flow patterns presented in Figure 4.8a-d were obtained using the mold #3 at the 90% filling stage, for a constant feedstock temperature and a mold temperature of 90°C and 40°C, respectively. The simulated and experimental flow patterns are in good agreement for each feedstock condition. Similarly to previous results, the flow patterns and the injection time were not influenced by the feedstock properties as the injections were performed at a constant volumetric flow rate of 9.74 cm$^3$/s.

The pressure profiles measured for a complete mold filling are presented in Figure 4.8e-f for the four different feedstocks. In general, the simulated pressure profiles are in good agreement with the experimental pressure profiles in terms of overall shape of the curves and pressure values obtained at different filling stages, with a maximum relative difference of 64% obtained with the feedstock G65. For the gas-atomized powder-based feedstocks, G60 and G65, an increase of 5 vol. % in powder content produces an increase in maximum pressure of 146 kPa, whereas for the water-atomized powder-based feedstocks, W60 and W65, the same solid loading increase produces a fourfold increase in the maximum pressure. This increase in injection pressure with an increase in the solid loading or decrease in powder sphericity is expected. On the one hand, it is worth noting that the feedstocks formulated at the same low solid loading of 60 vol. % (i.e., feedstocks W60 and G60) required similar injection pressures (with a maximum reached around 150 kPa), regardless of the powder shape. On the other hand, the feedstock W65 required a maximum pressure about three times higher than that of the feedstock G65. As anticipated by the rheological results (Figure 4.3a), the similar viscosity and similar low injection pressure of feedstocks W60 and G60 can be explained by the binder-rich zones and large interparticle spaces filled with binder (i.e., mixtures exhibiting a solid

loading relatively far from the CSL), reducing the particle interactions, and thus the impact of particle characteristics. For feedstocks close to the CSL, the significant difference in viscosity values and injection pressures obtained for the feedstocks W65 and G65 confirm that these mixtures are probably more sensitive and driven by particle-to-particle interactions where a slight decrease in powder sphericity produces a significant increase in feedstock viscosity. In all cases, a LPIM injection at high solid loading using typical process parameters produces a low injection pressure (< 1 MPa).
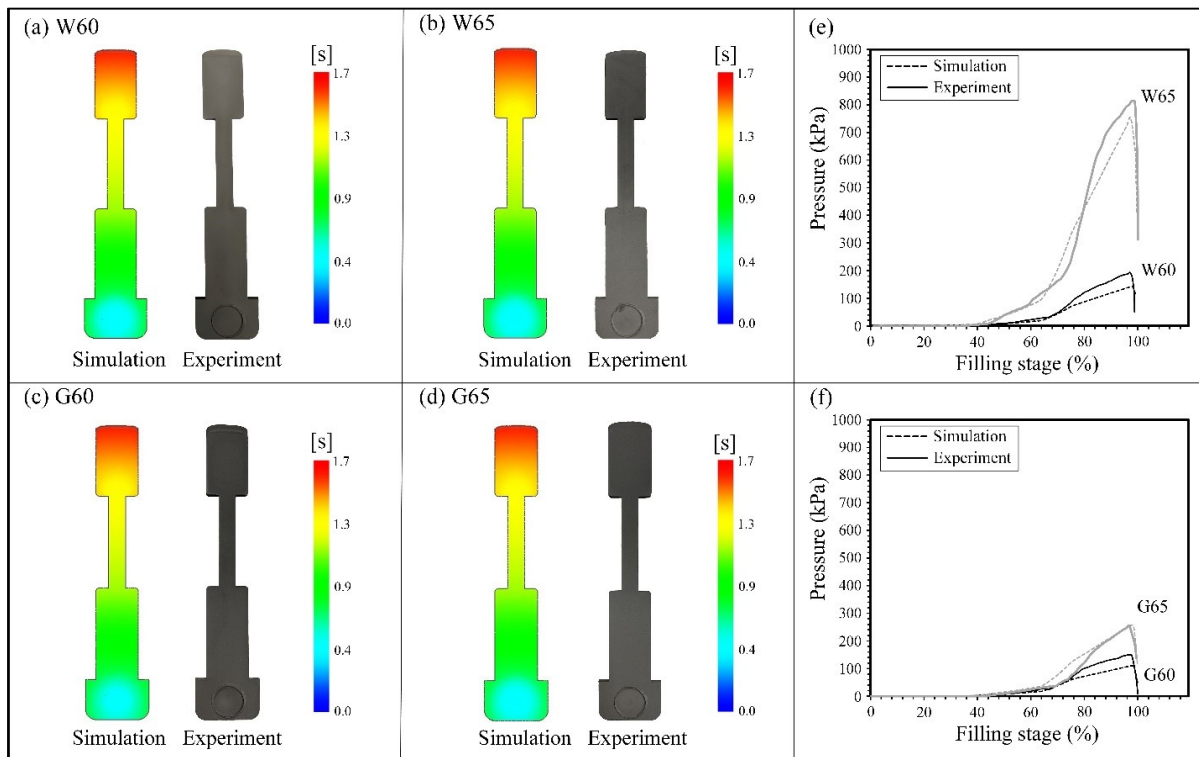


Figure 4.8 Simulated and experimental flow patterns at 90% filling stage for (a-b) water- and (c-d) gas-atomized powder-based feedstocks and (e-f) corresponding pressure profiles for complete filling (injected in mold #3 using constant thickness = 3 mm, feedstock temperature = 90°C, mold temperature = 40°C, and flow rate = 9.74 cm³/s)

### 4.4.4 Simulation of the filling behavior in a complex shape part

The capability of Moldflow to predict the mold filling behavior within a complex geometry (mold #5) is illustrated in Figure 4.9 for different filling stages (30, 60, 90, and 100%).

Experimental and numerical injections were carried out for the feedstock W60 using a constant feedstock temperature (90°C), mold temperature (40°C), and flow rate (9.74 cm$^3$/s). Since the gate is located at the center of the base (visible in Figure 4.5e), only part of the base (1) and the central core (2) are filled with feedstock after a 30% filling, as presented in Figure 4.9a. For this filling stage, the simulation is similar to the real-scale injection in terms of flow pattern. At the 60% filling stage (Figure 4.9b), the base (1) and the central core (2) are completely filled, while the struts (3), the lugs (4), and the walls (5) are partially filled with feedstock. For the second filling stage, the experimental and simulated short shots differ, with slightly different filled volumes of the struts (3), the lugs (4), and the walls (5), which may be due to the flow imbalance created by the two lugs (4) (of about 2.3 cm$^3$ or 7% of the total mold volume) symmetrically positioned on two of the four external walls (5). At the 90% filling stage (Figure 4.9c), the base (1), the central core (2), the struts (3), and the lugs (4) are completely filled, while the remaining 10% is contained in the four external walls (5). Although the flow imbalance observed experimentally was not perfectly captured by the numerical simulation, the general distribution of the feedstock within the mold cavity remained reasonably accurate. At the end of the mold filling, the complete mold filling predicted by the numerical model was confirmed with the real-scale injection where no obvious weld lines or incomplete filling was observed. The maximum injection pressure of about 8 kPa obtained numerically confirms that the LPIM approach can be used to shape this intricate metallic part.
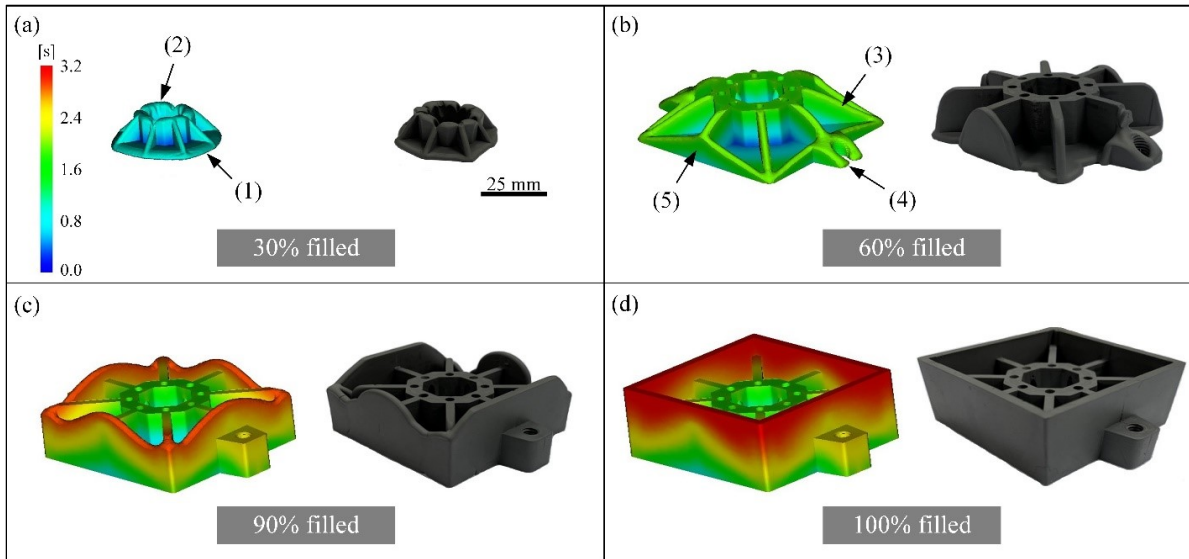
Figure 4.9 Numerical and experimental flow patterns for mold #5 from 30 to 100% filling stage. Numbers (1) to (5) indicate the base, the central core, the struts, the threaded lugs, and the walls, respectively.

## 4.5    Conclusion

The potential to simulate the flow behavior within molds of different shape complexities and to predict the injection pressure of LPIM metallic-based feedstocks during the injection stage was investigated using the Autodesk Moldflow Insight 2019 commercial software. Four different stainless steel-based feedstocks were formulated from two different powders (water- or gas-atomized) at two solid loadings (60 and 65 vol. % of powder), and characterized to obtain the melting point, specific volume, viscosity, specific heat, and thermal conductivity before being implemented in the simulation models. The simulated injected lengths and pressure profiles were validated with real-scale injections at various mold geometries, feedstock temperatures, mold temperatures, and feedstock properties. The analysis of the results led to three important conclusions:

- Regardless of the complexity of the mold (rectangular shape vs. complex shape), the flow patterns predicted by the numerical model were in good agreement with the experimental observations since the injections were carried out at a constant volumetric flow rate (i.e., were not influenced by the feedstock properties or process parameters,

except for the injection speed). Furthermore, the numerical model was able to accurately predict the pressure values for the molds #1 & #2, i.e., the two simplest molds used in this work, exhibiting constant or a single variation in the cross-section. However, a maximum relative difference of 64% between simulations and experiments was seen for the dogbone mold #3, which exhibited two variations in the cross-section.

- The simulated flow patterns and pressure profiles obtained for the dogbone mold when varying the feedstock temperature, the mold temperature, and feedstock properties were in good agreement with the experimental results.

- For a high solid loading (65 vol. % of powder), the powder morphology (water- vs. gas-atomized) had a significant influence on the injection pressure, where the model was able to capture the higher injection pressure required as the powder sphericity decreased (as seen in Figure 4.1c-d). Using an adequate feedstock characterization, the numerical model was able to adequately predict the flow patterns and injected pressures. Finally, this work confirms that further investigations are required to better understand the influence of the powder morphology on the injection pressure, especially for the LPIM process.

## 4.6    Acknowledgments

# CONCLUSION

This master's thesis aimed to evaluate the capability of Autodesk Moldflow Synergy 2019 to capture the influence of mold geometries, process parameters, and feedstock properties on flow pattern and injection pressure during injections using LPIM process. In this study, the simulated results were validated with experimental results obtained from real-scale injections. Four different feedstocks formulated from two different powders (water and gas atomized) and two solids loading (60 and 65 vol. %) were fully characterized to obtain properties such as viscosity, specific heat, density, and thermal conductivity that were implemented in the numerical model. These feedstocks were then injected into different mold cavities and the pressure were experimentally recorded in the gate of the mold.

The numerical results of the flow pattern were in good agreement with the experimental data for different filling stages. Since the injections were performed using a constant volumetric flow, the results confirmed that the feedstock properties, feedstock temperature, and mold temperature have no influence on the flow pattern. The simulated pressure results were in good agreement with experimental results over the majority of the mold filling stage with maximum relative differences varying from 30 to 64% depending on particular feedstocks and process parameters, including the capability to predict the filling stage associated with the changes in pressure values (i.e., due to change in mold cavity cross section). To the best of the author's knowledge, measurement and experimental validation of the simulated pressure values for LPIM process has been performed only once in two simple shape 2D mold cavities using Moldflow. Therefore, experimental validation of such low-pressure obtained numerically within more complex shape mold cavities has been confirmed for the first time in this project for low-viscosity metallic-based feedstocks.

## RECOMMENDATIONS

Based on the results, it is possible to predict the flow behavior of low-viscosity feedstocks during the LPIM process using numerical simulation tools. However, several possibilities for improving the simulated results should be considered. Here are some recommendations for future research:

- Heat transfer coefficient (HTC) determines the heat flux across the interface of the feedstock and the mold wall in Moldflow. HTC values are therefore important and yet are not well quantified in the existing studies. It is recommended to carry out further studies on the impact of HTC on the simulated pressure values in the LPIM process.

- The volumetric flow rate of 10 $cm^3$/s was used in this project to avoid feedstock solidification or jetting phenomenon occurring respectively at too low or too high flow rates. Therefore, it is recommended to evaluate the capability of Moldflow to capture pressure values at different flow rates.

- In line with the previous recommendation, evolution of pressure and temperature within the mold cavity can also be obtained using non-constant volumetric flow rate, by changing in real-time the piston speed to target a constant in-cavity pressure.

Other feedstock properties (especially the viscosity) must be simulated and validated to confirm that this successful prediction of the in-cavity pressure can be reproduced for almost all feedstocks used in LPIM process.

## LIST OF BIBLIOGRAPHICAL REFERENCES

Ahn, S., Chung, S., Atre, S., & Park, S. J. (2008). Integrated filling, packing and cooling CAE analysis of powder injection moulding parts. *Powder Metallurgy*, *51, 318-326.* https://doi.org/10.1179/174329008X284903

Ahn, S., Park, S. J., Lee, S., Atre, S. V., & German, R. M. (2009). Effect of powders and binders on material properties and molding parameters in iron and stainless steel powder injection molding process. *Powder Technology*, *193*(2), 162-169. https://doi.org/https://doi.org/10.1016/j.powtec.2009.03.010

Aich, Shampa, Satapathy, D.K., Shield, J.E. (2017) Advances in Magnetic Materials: Processing, Properties, and Performance, CRC Press Taylor & Francis Group, 1st Edition, Boca Raton, FL, USA, 758 pages.

ASTM-B923-16. (2016). *Standard Test Method for Metal Powder Skeletal Density by Helium or Nitrogen Pycnometry* ASTM International.

ASTM-D3418-15. (2015). *Standard Test Method for Transition Temperatures and Enthalpies of Fusion and Crystallization of Polymers by Differential Scanning Calorimetry*. ASTM International.

ASTM-D5930-17. (2017). *Standard Test Method for Thermal Conductivity of Plastics by Means of a Transient Line-Source Technique*. ASTM International.

ASTM-E1269-11. (2018). *Standard Test Method for Determining Specific Heat Capacity by Differential Scanning Calorimetry*. ASTM International.

ASTM-E2716-09. (2014). *Standard Test Method for Determining Specific Heat Capacity by Sinusoidal Modulated Temperature Differential Scanning Calorimetry*. ASTM International.

Atre, S., Park, S. J., & Zauner, R. (2007). Process simulation of powder injection moulding: Identification of significant parameters during mould filling phase. *Powder Metallurgy*, *50*, 76-85. https://doi.org/10.1179/174329007X185607

Azzouni, M., Demers, V., & Dufresne, L. (2021). Mold filling simulation and experimental investigation of metallic feedstock used in low-pressure powder injection molding. *International Journal of Material Forming, 14,* 961-972. https://doi.org/10.1007/s12289-021-01612-0

Bandiwadekar, B. P. (2017). *Material properties design using simulations and experiments for powder injection molding of lead zirconate titanate (PZT).* (Master's thesis, University of Louisville).

Barriere, T., Gelin, J. C., & Sheng, L. (2002). Improving mould design and injection parameters in metal injection moulding by accurate 3D finite element simulation. *Journal of Materials Processing Technology*, *125-126*, 518-524. https://doi.org/10.1016/S0924-0136(02)00307-2

Ben Trad, M. A., Demers, V., Côté, R., Sardarian, M., & Dufresne, L. (2020). Numerical simulation and experimental investigation of mold filling and segregation in low-pressure powder injection molding of metallic feedstock. *Advanced Powder Technology*, *31*(3), 1349-1358. https://doi.org/https://doi.org/10.1016/j.apt.2020.01.018

Bilovol, V., Kowalski, L., Duszczyk, J., & Katgerman, L. (2003). Comparison of numerical codes for simulation of powder injection moulding. *Powder Metallurgy*, *46*, 55-60. https://doi.org/10.1179/003258903225010514

Bilovol, V. V. (2003). *Mould filling simulations during powder injection moulding.* (Doctoral thesis, Delft University of Technology).

Binet, C., Heaney, D. F., Spina, R., & Tricarico, L. (2005). Experimental and numerical analysis of metal injection molded products. *Journal of Materials Processing Technology*, *164-165*, 1160-1166. https://doi.org/https://doi.org/10.1016/j.jmatprotec.2005.02.128

Côté, R., Azzouni, M., & Demers, V. (2020). Impact of binder constituents on the moldability of titanium-based feedstocks used in low-pressure powder injection molding. *Powder Technology*, *381,* 255-268. https://doi.org/10.1016/j.powtec.2020.12.008

Côté, R., Azzouni, M., Ghanmi, O., Kapoor, S., & Demers, V. (2020). Impact of rheological model on numerical simulation of low-pressure powder injection moulding. *Powder Metallurgy*, *64*, 1-9. https://doi.org/10.1080/00325899.2020.1852492

Custompartnet (2022). Metal injection molding steps. Retrieved from https://www.custompartnet.com/wu/metal-injection-molding

Fareh, F., Demers, V., Demarquette, N., Turenne, S., & Scalzo, O. (2016). Molding Properties of Inconel 718 Feedstocks Used in Low-Pressure Powder Injection Molding. *Advances in Materials Science and Engineering*, *2016*, 1-7. https://doi.org/10.1155/2016/7078045

Fareh, F., Demers, V., Demarquette, N. R., Turenne, S., & Scalzo, O. (2017). Influence of segregation on rheological properties of wax-based feedstocks. *Powder Technology*, *320*, 273-284. https://doi.org/https://doi.org/10.1016/j.powtec.2017.07.056

German, R. M. (2008). PIM breaks the $1 bn barrier. *Metal Powder Report*, *63*(3), 8-10. https://doi.org/https://doi.org/10.1016/S0026-0657(08)70036-5

German, R. M. (2012). Markets applications, and financial aspects of global metal powder injection moulding (MIM) technologies. *Metal Powder Report*, *67*, 18–26. https://doi.org/10.1016/S0026-0657(12)70051-6

German, R. M., & Bose, A. (1997). Injection molding of metals and ceramics. *Metal Powder Industries Federation, Princeton, NJ.*

Ghalya, A. (2018). *Influence of wax-based binder formulations on rheological properties of feedstocks used in low-pressure metal injection.* (Master's thesis, École de technologie supérieure).

Ghanmi, O., & Demers, V. (2021). Molding properties of titanium-based feedstock used in low-pressure powder injection molding. *Powder Technology*, *379*, 515-525. https://doi.org/https://doi.org/10.1016/j.powtec.2020.10.068

Gonçalves, A. C. (2001). Metallic powder injection molding using low pressure. *Journal of Materials Processing Technology*, *118*(1), 193-198. https://doi.org/https://doi.org/10.1016/S0924-0136(01)00916-5

Gonzalez-Gutierrez, J., Duretek, I., Kukla, C., Poljšak, A., Bek, M., Emri, I., & Holzer, C. (2016). Models to Predict the Viscosity of Metal Injection Molding Feedstock Materials as Function of Their Formulation. *Metals*, *6*(6), 129. https://www.mdpi.com/2075-4701/6/6/129

González-Gutiérrez, J., Stringari, G. B., & Emri, I. (2012). Powder injection molding of metal and ceramic parts. Some Critical Issues for Injection Molding, 65-88.

Hausnerova, B. (2011). Powder injection moulding-An alternative processing method for automotive items. New Trends and Developments in Automotive System Engineering, 129-145.

Heaney, D. F. (2012). Handbook of Metal Injection Molding. Elsevier.

Hwang, C., & Kwon, T. (2002). A full 3D finite element analysis of the powder injection molding filling process including slip phenomena. *Polymer Engineering and Science*, *42*, 33-50. https://doi.org/10.1002/pen.10926

Ilinca, F., & Hétu, J.-F. (2001). Three Dimensional Filling and Post-filling Simulation of Polymer Injection Molding. *International Polymer Processing*, *16*, 291-301. https://doi.org/10.3139/217.1643

Ilinca, F., Hétu, J.-F., Derdouri, A., & Stevenson, J. (2004). Metal injection molding: 3D modeling of nonisothermal filling. *Polymer Engineering & Science*, *42*, 760-770. https://doi.org/10.1002/pen.10988

Kamal, M. R., & Isayev, A. I. (2012). *Injection Molding Technology and Fundamentals*. Carl, München Hanser

Kate, K., Enneti, R., Park, S. J., & Atre, S. (2014). Predicting Powder-Polymer Mixture Properties for PIM Design. *Critical Reviews in Solid State and Material Sciences*, *39*(3)*, 197-214. https://doi.org/10.1080/10408436.2013.808986

Kennedy, P., & Zheng, R. (2013). *Flow analysis of injection molds*. Carl Hanser Verlag GmbH Co KG. https://doi.org/10.3139/9781569905227.fm

Khan, M., Sardar, H., Gulzar, M. M., & Alshomrani, A. S. (2018). On multiple solutions of non-Newtonian Carreau fluid flow over an inclined shrinking sheet. *Results in Physics*, *8*, 926-932. https://doi.org/https://doi.org/10.1016/j.rinp.2018.01.021

Kong, X. (2011). *Development and characterization of polymer-metallic powder feedstocks for micro-injection molding.* (Doctoral dissertation, Université de Franche-Comté).

Koszkul, J., & Nabiałek, J. (2004). Viscosity models in simulation of the filling stage of the injection molding process. *Journal of Materials Processing Technology*, *157*, 183-187. https://doi.org/10.1016/j.jmatprotec.2004.09.027

Kowalski, L., Duszczyk, J., & Katgerman, L. (1999). Thermal conductivity of metal powder-polymer feedstock for powder injection moulding. *Journal of Materials Science*, *34*(1), 1-5. https://doi.org/10.1023/A:1004424401427

Krueger, D. C. (1996). *U.S. Patent No. 5,531,958*. Washington, DC: U.S. Patent and Trademark Office.

Krug, S., Evans, J. R. G., & Maat, J. H. H. (2002). Differential sintering in ceramic injection moulding: particle orientation effects. *Journal of the European Ceramic Society*, *22*, 173-181. https://doi.org/10.1016/S0955-2219(01)00259-X

Kryachek, V. M. (2004). Injection Moulding (Review). *Powder Metallurgy and Metal Ceramics*, *43*(7), 336-348. https://doi.org/10.1023/B:PMMC.0000048127.24809.d3

Lamarre, S. (2016). *Conception, fabrication et validation d'une presse à injection basse pression pour le procédé des poudres métalliques.* (Doctoral dissertation École de technologie supérieure).

Lamarre, S., Demers, V., & Chatelain, J. F. (2017). Low-pressure powder injection molding using an innovative injection press concept. *The International Journal of Advanced Manufacturing Technology*, *91*(5), 2595-2605. https://doi.org/10.1007/s00170-016-9889-1

Lenz, J., Enneti, R., Onbattuvelli, V., Kate, K., Martin, R., & Atre, S. (2012). Powder Injection Molding of Ceramic Engine Components for Transportation. *JOM*, *64*(3), 388-392. https://doi.org/10.1007/s11837-012-0264-x

Lenz, J., Enneti, R., Park, S. J., & Atre, S. (2014). Powder Injection Molding Process Design For UAV Engine Components Using Nanoscale Silicon Nitride Powders. *Ceramics International*, *40*(1), 893-900. https://doi.org/10.1016/j.ceramint.2013.06.084

Lin, D., Sanetrnik, D., Cho, H., Chung, S., Kwon, Y.-S., Kate, K., Hausnerova, B., Atre, S., & Park, S. J. (2017). Rheological and thermal debinding properties of blended elemental Ti-6Al-4V powder injection molding feedstock. *Powder Technology*, *311*, 357-363. https://doi.org/10.1016/j.powtec.2016.12.071

Liu, L., Gao, Y. Y., Qi, X. T., & Qi, M. X. (2018). Effects of wall slip on ZrO2 rheological behavior in micro powder injection molding. *Ceramics International*, *44*(14), 16282-16294. https://doi.org/https://doi.org/10.1016/j.ceramint.2018.06.022

Liu, Z., Loh, N., Tor, S., & Khor, K. (2002). Characterization of powder injection molding feedstock. *Materials Characterization*, *49*(4), 313-320. https://doi.org/10.1016/S1044-5803(02)00282-6

Lucyshyn, T., d'Avernas, L.-V., & Holzer, C. (2021). Influence of the Mold Material on the Injection Molding Cycle Time and Warpage Depending on the Polymer Processed. *Polymers*, *13*(18), 3196. https://doi.org/10.3390/polym13183196

Lucyshyn, T., Knapp, G., Kipperer, M., & Holzer, C. (2012). Determination of the Transition Temperature at Different Cooling Rates and Its Influence on Prediction of Shrinkage and Warpage in Injection Molding Simulation. *Journal of Applied Polymer Science*, *123*(2), 1162-1168. https://doi.org/10.1002/app.34591

Macosko, C. W. (1994). Rheology Principles. *Measurements and Applications*.

Majdi, S. M., Tafti, A. A., Demers, V., Vachon, G., & Brailovski, V. (2021). Effect of powder particle shape and size distributions on the properties of low-viscosity iron-based feedstocks used in low-pressure powder injection moulding. *Powder Metallurgy*, 1-11. https://doi.org/10.1080/00325899.2021.1959696

Mathew, B. A., & Mastromatteo, R. (2002). Metal injection moulding for automotive applications. *Metal Powder Report*, *57*(3), 20-23.

Medvedovski, E., & Peltsman, M. (2012). Low Pressure Injection Moulding Mass Production Technology of Complex Shape Advanced Ceramic Components. *Advances in Applied Ceramics*, *111*(5-6), 333-344. https://doi.org/10.1179/1743676112Y.0000000025

Merz, L., Rath, S., Piotter, V., Ruprecht, R., Ritzhaupt-Kleissl, J., & Hausselt, J. (2002). Feedstock development for micro powder injection molding. *Microsystem Technologies*, *8*, 129-132. https://doi.org/10.1007/s00542-002-0166-x

Mulser, M., Petzoldt, F., Lipinski, M., & Hepp, E. (2011). Powder Injection Moulding: Advance Processing: Influence of the Injection Parameters on the Interface Formation of Co-injected PIM Parts. In *European Congress and Exhibition on Powder Metallurgy. European PM Conference Proceedings* (p. 1). The European Powder Metallurgy Association.

Osswald, T., & Rudolph, N. (2015). Generalized newtonian fluid (GNF) models. *Polymer Rheology Fundamentals and Applications; Strohm, C., Ed.; Hanser Publications: Cincinnati, OH, USA*, 59-74.

Osswald, T., & Rudolph, N. (2015). Polymer rheology. *Carl Hanser, München*.

Peltsman, M. (1986). Low pressure injection moulding and mould design. *Metal Powder Report*, *41*(5), 367-369.

Poh, P. Y. (2019). *Experimental and numerical study of silicon nitride for powder injection moulding.* (Doctoral dissertation, University of Glasgow).

Qu, X., Gao, J., Qin, M., & Lei, C. (2005). Application of a wax-based binder in PIM of WC–TiC–Co cemented carbides. *International Journal of Refractory Metals and Hard Materials*, *23*(4), 273-277 https://doi.org/https://doi.org/10.1016/j.ijrmhm.2005.04.006

Quinard, C., Barriere, T., & Gelin, J. C. (2009). Development and property identification of 316L stainless steel feedstock for PIM and µPIM. *Powder Technology*, *190*(1), 123-128. https://doi.org/https://doi.org/10.1016/j.powtec.2008.04.044

Raymond, V. (2012). *Metal injection molding development: modeling and numerical simulation of injection with experimental validation.* (Master's thesis, École Polytechnique de Montréal).

Rei, M., Milke, E. C., Gomes, R. M., Schaeffer, L., & Souza, J. P. (2002). Low-pressure injection molding processing of a 316-L stainless steel feedstock. *Materials Letters*, *52*(4), 360-365. https://doi.org/https://doi.org/10.1016/S0167-577X(01)00422-0

Samanta, S. K., Chattopadhyay, H., Pustal, B., Berger, R., Godkhindi, M. M., & Bührig-Polaczek, A. (2008). A numerical study of solidification in powder injection molding process. *International Journal of Heat and Mass Transfer*, *51*(3), 672-682 https://doi.org/https://doi.org/10.1016/j.ijheatmasstransfer.2007.04.033

Sanetrnik, D., Hausnerova, B., Novak, M., & Mukund, B. (2021). Effect of Particle Size and Shape on Wall Slip of Highly Filled Powder Feedstocks for Material Extrusion and Powder Injection Molding. *3D Printing and Additive Manufacturing*.

Sardarian, M., Mirzaee, O., & Habibolahzadeh, A. (2017). Influence of injection temperature and pressure on the properties of alumina parts fabricated by low pressure injection molding (LPIM). *Ceramics International*, *43*(6), 4785-4793. https://doi.org/10.1016/j.ceramint.2016.11.208

Sardarian, M., Mirzaee, O., & Habibolahzadeh, A. (2017). Mold filling simulation of low pressure injection molding (LPIM) of alumina: Effect of temperature and pressure. *Ceramics International*, *43*(1), 28-34. https://doi.org/10.1016/j.ceramint.2016.07.224

Sardarian, M., Mirzaee, O., & Habibolahzadeh, A. (2017). Numerical simulation and experimental investigation on jetting phenomenon in low pressure injection molding (LPIM) of alumina. *Journal of Materials Processing Technology*, *243*, 374-380. https://doi.org/10.1016/j.jmatprotec.2016.12.014

Semenov, A., Kutsbakh, A., Muranov, A., & Semenov, B. (2019). Development of a Technique to Simulate the Injection Molding of Metallic-Powder-Filled Polymers. *Russian Metallurgy (Metally)*, *2019*, 1351-1356 https://doi.org/10.1134/S0036029519130330

TA Instruments (2021). DSC 2500. Retrieved from https://www.tainstruments.com/dsc-2500/

Thomas, Y., Baril, E., Ilinca, F., & Hetu, J. F. (2009). Development of titanium dental implant by MIM: experiments and simulation. *Advances in Powder Metallurgy and Particulate Materials*, *4*, 81-93.

Thornagel, M. (2010). Simulating flow can help avoid mould mistakes. *Metal Powder Report*, *65*(3), 26-29. https://doi.org/https://doi.org/10.1016/S0026-0657(10)70072-2

Tosello, G., Marhöfer, D. M., Islam, A., Müller, T., Plewa, K., & Piotter, V. (2019). Comprehensive characterization and material modeling for ceramic injection molding simulation performance validations. *The International Journal of Advanced Manufacturing Technology*, *102*(1), 225-240. https://doi.org/10.1007/s00170-018-03251-3

Tseng, H. C., Chang, Y. J., Tien, C. H., & Hsu, C. H. (2014). Prediction of powder concentration for filling simulation of metal injection molding. In *SPE Annual Tech meeting*.

Xu, J. (2011). *Microcellular injection molding*. John Wiley & Sons.

Yavari, R., & Khorsand, H. (2021). Numerical and experimental study of injection step, separation, and imbalance filling in low pressure injection molding of ceramic components. *Journal of the European Ceramic Society*, *41*(14), 6915-6924. https://doi.org/10.1016/j.jeurceramsoc.2021.07.050

Zhang, M. M., & Lin, B. (2007). Simulation of ceramic injection molding for zirconia optical ferrule. In *Key Engineering Materials* (Vol. 336, pp. 997-1000). Trans Tech Publications Ltd. https://doi.org/10.4028/www.scientific.net/KEM.336-338.997

Zheng, Z. S., & Qu, X. H. (2006). Numerical simulation of powder injection moulding filling process for intricate parts. *Powder metallurgy*, *49*(2), 167-172. https://doi.org/10.1179/174329006X95329

Zink, B., & Kovacs, J. G. (2022). Pressure-dependent heat transfer coefficient measurement for thermoplastic melts. *Polymer Engineering & Science*.